Millimeter Wave Circularly Polarized Antennas Based on Printed Ridge Gap Waveguide Technology

Elham Baghernia

A Thesis

in

The Department

of

Electrical and Computer Engineering

Presented in Partial Fulfillment of the Requirements

for the Degree of

Doctor of Philosophy (Electrical and Computer Engineering) at

Concordia University

Montréal, Québec, Canada

January 2022

CONCORDIA UNIVERSITY

School of Graduate Studies

This is to certify that the thesis prepared

By: **Elham Baghernia**

Entitled: **Millimeter Wave Circularly Polarized Antennas Based on Printed Ridge Gap Waveguide Technology**

and submitted in partial fulfillment of the requirements for the degree of

Doctor of Philosophy (Electrical and Computer Engineering)

complies with the regulations of this University and meets the accepted standards with respect to originality and quality.

Signed by the Final Examining Committee:

______________________ Chair
Dr. Kudret Demirli

______________________ External Examiner
Dr. Yahia Antar

______________________ External to Program
Dr. Dmitry Korotkin

______________________ Examiner
Dr. Ahmed A. Kishk

______________________ Examiner
Dr. Robert Paknys

______________________ Thesis Supervisor
Dr. Abdel R. Sebak

Approved by ______________________
Dr. Wei-Ping Zhu, Graduate Program Director

January 31, 2022

____
Dr. Mourad Debbabi, Dean
Gina Cody School of Engineering and Computer Science

Abstract

Millimeter Wave Circularly Polarized Antennas Based on Printed Ridge Gap Waveguide Technology

Elham Baghernia, Ph.D.

Concordia University, 2022

The growing demand for higher data rates in wireless communication systems has built a significant momentum toward the fifth-generation (5G) of mobile communications as there are more uncongested frequency bands compared to the sub 6 GHz band. Circularly polarized (CP) antennas are highly required for the 5G millimeter-wave (mm-wave) systems due to their attractive features like reducing the polarization mismatch between transmitting and receiving antenna and suppressing multipath interference. The printed ridge gap waveguide (PRGW) technology exhibits desirable features at high frequencies due to its air-filled guiding medium. Therefore, the implementation of antenna arrays with these state-of-the-art guiding structures can enhance the efficiency of communication systems, which is highly required at mm-wave frequencies.

This research can be divided into two main parts: First, development of wideband mm-wave CP antenna array based on PRGW. Two designs for CP antenna arrays with distinct features of wideband bandwidth of more than 22.5%, simple structure, compact size, and high radiation efficiency better than 85% are presented. Cavity-backed slot spiral and spiral antenna are chosen as radiating elements to achieve RHCP beam. The mentioned antennas benefit from their inherently broadband features. However, their traditional feeding procedures are quite challenging and require complicated balun circuits and external matching networks. To alleviate this issue, simple feeding techniques for both spiral and slot spiral antennas have been proposed in this research.

In the second main part of the research, a PRGW wideband dual CP antenna array is developed to increase the system capacity further. The dual sense of circular operation is achieved by using a shared radiating aperture of a 2×2 45° ME dipole array and a two-port feeding network. The

proposed dual-port feeding network provides equal power division and the phase difference of -90° and +90° between adjacent output ports to generate RHCP and LHCP beams, respectively. The feeding network components (rat-race couplers, directional couplers, and crossover) are designed based on PRGW technology with broadband performance. The proposed design solves the problem of limited operating bandwidth and low radiation efficiency of low-profile dual CP arrays in the mm-wave band.

All proposed antenna arrays are fabricated and measured to verify the simulated results. Good agreement between simulation and measured results is obtained. In all designs, the wideband performance, compactness, high radiation efficiency, and integration capability are considered significant to make them suitable for mm-wave applications.

Acknowledgments

I would like to express my deepest gratitude to my supervisor, Prof. Abdel R. Sebak, for his valuable insights and inspirational guidance throughout my Ph.D. study. Without his constant support, this research would not have been possible.

I would also like to acknowledge the committee members, Prof. Ahmed A. Kishk, Prof. Robert Paknys, Prof. Yahia Antar, and Prof. Dmitry Korotkin, for their valuable comments and suggestions to improve the quality of my thesis.

My sincere appreciation to all my family members and friends for their motivation and support, and my special thanks to my loving husband, Sadegh, for his unconditional love and continuous encouragement.

To my love, Sadegh

To my beloved parents, Mohsen and Zahra

For their endless support and encouragement

Contents

List of Figures **x**

List of Tables **xv**

List of Abbreviations **xv**

List of Symbols **xvii**

1 Introduction **1**

1.1 Problem Statement and Motivation 2

1.2 Objective 4

1.3 Main Contributions 4

1.4 Organization of the Thesis 6

2 Theoretical Background and Literature Review **8**

2.1 Introduction 8

2.2 Circular Polarization 8

2.3 Spiral Antenna 12

2.3.1 The Principle of Operation 13

2.4 Sequential Rotation Feeding Technique 14

2.4.1 Sequential Rotation with Linearly Polarized Elements 16

2.4.2 Implementation of Sequential Feeding with Different Technologies 20

2.5 Challenges in Conventional Guiding Structure 20

2.5.1 Soft and Hard Surfaces 21
2.5.2 Gap Waveguide Technology 22
2.6 Research Methodology 25
2.7 Summary 26

3 Slot Spiral Cavity-Backed Antenna Array **27**
3.1 Introduction 27
3.2 Antenna Design 28
3.2.1 Equiangular Spiral Antenna 28
3.2.2 Cavity Excitation 30
3.2.3 Printed Ridge Gap Waveguide 32
3.2.4 Single Element Performance 33
3.2.5 Printed Ridge Gap Waveguide to Microstrip Line Transition 35
3.3 Circularly Polarized Antenna Array 37
3.3.1 2×2 Sequential Feeding Network 37
3.3.2 Effect of Cavity on Array Performance 40
3.4 Fabrication and Measurement 41
3.4.1 Simulation and Measurement Results 42
3.4.2 Comparison and Discussion 45
3.5 Summary 46

4 Broadband Compact Circularly Polarized Spiral Antenna Array **47**
4.1 Introduction 47
4.2 Realization of the Proposed CP Spiral Antenna 48
4.2.1 Single Radiating Element Design 48
4.2.2 Single Element Operating Principles 50
4.2.3 Printed Ridge Gap Waveguide 53
4.2.4 Performance 55
4.3 Circularly Polarized Antenna Array 56
4.3.1 2×2 array 56

4.3.2 Feeding Network . . . 56
4.4 Measured and Simulated Array Performance . . . 59
4.4.1 Fabrication and Measurement . . . 59
4.4.2 Experimental Results . . . 62
4.4.3 Comparison and Discussion . . . 65
4.5 Summary . . . 66

5 Millimeter-Wave Dual Circularly Polarized Antenna Array 68
5.1 Introduction . . . 68
5.2 Dual Circularly Polarized Feeding Structure . . . 69
5.2.1 Printed Ridge Gap Rat-Race Coupler . . . 71
5.2.2 Printed Ridge Gap 90° Directional Coupler . . . 73
5.2.3 Printed Ridge Gap Crossover . . . 75
5.2.4 PRGW Feeding Network . . . 77
5.3 45° ME Dipole Antenna Design . . . 79
5.3.1 Comparison Between 2×2 Sequentially Rotated 45° ME Dipole and ME Dipole Array . . . 82
5.4 Circularly Polarized Antenna Array . . . 85
5.4.1 2×2 Array . . . 85
5.4.2 Fabrication and Measurement . . . 86
5.4.3 Comparison and Discussion . . . 92
5.5 Summary . . . 93

6 Conclusions and Future Works 94
6.1 Summary . . . 94
6.2 Future Works . . . 96

Appendix A Electric Field of N-Element Sequentially Rotated Antenna Array 98

Bibliography 101

List of Figures

Figure 1.1 The electromagnetic spectrum [6]. 2
Figure 2.1 Polarization examples (a) Linear Polarization, (b) Circular Polarization, (c) Elliptical Polarization. 9
Figure 2.2 Contour plot of AR (dB). 11
Figure 2.3 (a) Equiangular spiral curve, (b) Two-arm Archimedean spiral antenna [24]. 13
Figure 2.4 Mode patterns for a spiral antenna [18]. 13
Figure 2.5 Active region (m=1) shown in two-arm Archimedean spiral antenna [24]. . . 14
Figure 2.6 Principle of sequentially rotated feeding [47]. 15
Figure 2.7 Phase distribution for RHCP and LHCP. 16
Figure 2.8 Two LP elements radiation in the yz plane. 17
Figure 2.9 Calculated CP patterns of the two-element array with element spacing of 0.87λ [55]. 19
Figure 2.10 2×2 sequentially rotated subarray, (a) arrangement to suppress the cross-polarization at $\phi = 0°$ and $\phi = 90°$ planes, (b) arrangement to suppress the cross polarization at $\phi = 0°$, $\phi = 90°$, and $\phi = \pm 45°$ planes. 19
Figure 2.11 SIW SR feeding network [67]. 21
Figure 2.12 Realization of soft and hard surfaces in corrugated metal slab. 22
Figure 2.13 Configuration of RGW. 23
Figure 2.14 Different types of gap waveguide structures, (a) Ridge gap waveguide, (b) Groove gap waveguide, (c) Microstrip gap waveguide, (d) Inverted gap waveguide, (e) Suspended gap waveguide. 24

Figure 2.15 Electric field lines of the quasi-TEM mode. 24
Figure 2.16 Flow chart of the research methodology. 25
Figure 3.1 Geometry of the proposed antenna element, (a) Perspective view, (b) Top view. 29
Figure 3.2 Electric field distribution in the SIC at 32 GHz. 30
Figure 3.3 Surface current distributions on the proposed antenna at different phases at 35.75 GHz. 31
Figure 3.4 (a) Circle mushroom unit cell (L=1.5mm, $\mathbf{r_p}$=0.55mm, $\mathbf{h_1}$=0.76mm, $\mathbf{h_2} = \mathbf{h_3}$=0.254mm,) (b) PRGW section. 32
Figure 3.5 Dispersion diagram of the mushroom unit cell. 33
Figure 3.6 Dispersion diagram of the PRGW section. 33
Figure 3.7 Simulated reflection coefficient of the proposed single antenna. 34
Figure 3.8 Simulated AR and Gain of the proposed single antenna. 34
Figure 3.9 Simulated 2-D radiation pattern of the proposed single element in xoz and yoz planes at 35.75 GHz. 35
Figure 3.10 PRGW to 50Ω Microstrip line transition, (a) 3D geometry, (b) Top view ($W_1 = 0.7mm, W_2 = 1mm, l_1 = 3.9mm$). 36
Figure 3.11 Simulated S-parameters of PRGW to 50Ω Microstrip line transition. 37
Figure 3.12 3D view of the 2×2 antenna array with the end launch connector. 37
Figure 3.13 Configuration of the proposed 2×2 antenna array. 38
Figure 3.14 Sequential feeding network implemented by PRGW. 38
Figure 3.15 Simulated Results of the designed sequential feeding network, (a) S-parameters, (b) phase error between output ports. 39
Figure 3.16 Simulated AR of the designed antenna array for the two cases of with and without the cavity. 40
Figure 3.17 (a) Fabricated proposed antenna arrays before assembly, (b) Fabricated proposed antenna array after assembly. 41
Figure 3.18 Simulated and measured reflection coefficient of the proposed antenna array. 42
Figure 3.19 Simulated and measured gain and AR of the proposed antenna array. 42
Figure 3.20 Radiation pattern measurement setup. 43

Figure 3.21 Simulated and measured 2-D radiation pattern of the proposed antenna array at (a) 35 GHz, (b) 37 GHz, and (c) 39 GHz. 44
Figure 4.1 Geometry of the proposed antenna element, (a) Perspective view, (b) Top view. 49
Figure 4.2 Cross section view of the proposed element with sketch of electric field, electric and magnetic currents. 51
Figure 4.3 Magnitude and phase of E_θ and E_ϕ in the y-z plane at 34 GHz, (a) With patch dipole, (b) Without patch dipole. 51
Figure 4.4 E-field distributions on the plane just above the top layer in a period of time at 34 GHz, (a) t = 0, (b) t = T/4, (c) t = T/2, (d) t = 3T/4. 52
Figure 4.5 Dispersion diagram of the designed unitcell (with $\mathbf{L}$=1.6mm, $\mathbf{r_p}$=0.65mm, $\mathbf{r_v}$=0.4 mm, $\mathbf{h_1}$=0.76mm, $\mathbf{h_2}$=$\mathbf{h_3}$=0.254 mm). 53
Figure 4.6 (a) PRGW section, (b) Dispersion diagram of PRGW section. 54
Figure 4.7 Simulated reflection coefficient of the proposed single antenna. 55
Figure 4.8 Simulated AR and RHCP Gain of the proposed single antenna. 55
Figure 4.9 Simulated normalized radiation pattern of proposed single antenna at 34 GHz in xoz and yoz planes. 56
Figure 4.10 Proposed antenna array structure. 57
Figure 4.11 Sequential feeding network implemented by PRGW. 57
Figure 4.12 Simulated S-parameters of the designed sequential feeding network. 58
Figure 4.13 Simulated phase error between the subsequent ports of the designed sequential feeding network. 59
Figure 4.14 Photographs of fabricated proposed antenna arrays, (a) Top view, (b) Bottom view. 60
Figure 4.15 Measurement setups,(a) N5227A PNA network analyzer, (b) anechoic chamber. 61
Figure 4.16 Simulated and measured reflection coefficient of the proposed antenna array. 62
Figure 4.17 Simulated and measured RHCP gain and AR of the proposed antenna array. 63
Figure 4.18 Simulated 2-D radiation patterns of the proposed antenna array at (a) 31 GHz, (b) 34 GHz, and (c) 37 GHz. 64

Figure 4.19 Simulated radiation efficiency of the proposed single element and antenna array. . . . 65
Figure 5.1 The schematic of the proposed dual polarized feeding network. 70
Figure 5.2 (a) Mushroom unit cell geometry ($h_1 = 0.762mm, h_2 = h_3 = 0.254mm, L = 1.7mm, W_p = 0.7mm, r_p = 0.2mm$), (b) Dispersion diagram of the PRGW. . . . 71
Figure 5.3 Geometry of the proposed wideband PRGW rat-race coupler. 72
Figure 5.4 Simulated results of the proposed wideband PRGW rat-race coupler, a) amplitude, (b) phase response. 73
Figure 5.5 Geometry of the proposed wideband PRGW 3-dB directional coupler. . . . 74
Figure 5.6 Simulated results of the proposed wideband PRGW 3-dB directional coupler, a) amplitude, (b) phase response. 75
Figure 5.7 (a) Geometry of the proposed wideband PRGW crossover, (b) Simulated S-parameters. 76
Figure 5.8 (a) Geometry of the proposed wideband PRGW crossover, (b) Simulated S-parameters. 77
Figure 5.9 Geometry of the proposed feeding network for dual sense of CP antenna. . . 78
Figure 5.10 Simulated S-parameters of the proposed feeding network for excitation from port 1. 78
Figure 5.11 Simulated S-parameters of the proposed feeding network for excitation from port 2. 79
Figure 5.12 Phase difference between the output ports for the excitation of port 1 and port 2. 79
Figure 5.13 Superposition of radiation patterns of the electric and the magnetic dipoles [124]. 80
Figure 5.14 Configuration of the proposed 45° ME dipole antenna. 80
Figure 5.15 Simulated reflection coefficient and realized gain of the proposed antenna . . 81
Figure 5.16 Simulated radiation patterns of the proposed antenna at 30 GHz. 82
Figure 5.17 (a) SR 45° ME dipole antenna, (b) SR ME dipole antenna. 83

Figure 5.18 Simulated normalized cross polarization at $\phi = 0°$ or $90°$, and $\phi = \pm 45°$ (a) RHCP. (b) LHCP. 84
Figure 5.19 Expanded view of dual-polarized ME dipole antenna array. 85
Figure 5.20 3D view of the 2×2 dual-polarized ME dipole antenna array with the end launch connector. 86
Figure 5.21 The fabricated dual CP polarized antenna, (a) top (b) bottom view. 87
Figure 5.22 S-Parameters of the antenna array for excitation of each input port. 88
Figure 5.23 Measured and simulated isolation between port 1 and port 2. 88
Figure 5.24 AR of the antenna array for excitation of each input port. 89
Figure 5.25 Realized gain of the antenna array for excitation of each input port. 89
Figure 5.26 Simulated 2-D radiation patterns of the proposed dual polarized antenna array when port 1 is excited, (a) 27 GHz,(b) 29 GHz, and (c) 31 GHz. 90
Figure 5.27 Simulated 2-D RP patterns of the proposed dual polarized antenna array when port 2 is excited (a) 27 GHz,(b) 29 GHz and (c) 31 GHz. 91
Figure 5.28 Simulated radiation efficiency for both CP Polarization. 92
Figure A.1 Vector geometry of Rodrigues' rotation formula 99

List of Tables

Table 3.1 Dimension of the proposed single element 30

Table 3.2 Comparison between the proposed antenna array and other reported 2×2 antenna array at mm-wave band 45

Table 4.1 Dimension of the proposed single element (mm) 50

Table 4.2 Dimension of the proposed sequential feeding Network (mm) 58

Table 4.3 Comparison Between the proposed mm Wave CP antenna array and some related works in the references 66

Table 5.1 Dimension of the proposed wideband PRGW rat-race coupler (mm) 72

Table 5.2 Dimension of the proposed wideband PRGW directional coupler (mm) . . . 74

Table 5.3 Dimension of the proposed wideband PRGW directional coupler (mm) . . . 76

Table 5.4 Dimension of the proposed $45°$ ME dipole antenna (mm) 81

Table 5.5 Comparison with other dual CP works 93

List of Abbreviations

1G:	First-Generation
4G:	Fourth-Generation
5G:	Fifth-Generation
AMC:	Artificial Magnetic Conductor
AR:	Axial Ratio
CP:	Circularly Polarized
EBG:	Electromagnetic Band Gap
FI:	Frequency Independent
Gbps:	Gigabytes per Second
LHCP:	Left Hand Circularly Polarized
LP:	Linearly Polarized
LTCC:	Low-temperature Co-fired Ceramic
ME:	Magneto-Electric
MMW:	Millimeter Wave
MSL:	Microstrip Line
PCB:	Printed Circuit Board
PEC:	Perfect Electric Conductor
PRGW:	Printed Ridge Gap Waveguide
PMC:	Perfect Magnetic Conductor
PNA:	Programmable Network Analyzer
RGW:	Ridge Gap Waveguide

RHCP:	Right Hand Circularly Polarized
SR:	Sequential Rotation
SIC:	Substrate Integrated Cavity
SIW:	Substrate Integrated Waveguide

List of Symbols

ϵ_r:	Permittivity of medium
ϵ_0:	Permittivity of vacuum
$\vec{E}$:	Electric field
β:	Propagation constant
η_{ap}:	Aperture efficiency
η_{rad}:	Radiation efficiency
λ:	Wavelength
λ_0:	Wavelength in free space
f:	Frequency
dB:	Decibels
$tan\delta$:	Loss tangent
Ω:	Ohms

Chapter 1

Introduction

The evolution of wireless communication systems was traced back to 1980 with the development of the first-generation (1G) network in which people were communicating with simple voice systems [1]. Nowadays, people are enjoying the tens of megabits per second (Mbps) data rates provided by the fourth-generation (4G) of wireless technology. However, there is an insatiable thirst for channel capacity and user data rates. The 5G communication systems are expected to provide tens of gigabit per second (Gbps) data rates for all users to keep pace with the increasingly high traffic demand of the future [2].

One innovative approach to realize 5G system requirements is the use of underutilized and unregulated spectrum at millimeter-wave (mm-wave) frequencies. The mm-wave technology dates backed to several decades ago when it was mainly deployed for military applications[3]. Recent advances in the technology of low-cost integrated chips pave the way for the usage of high-speed communication systems at mm-wave frequencies. The range of 30-300 GHz in the electromagnetic spectrum is occupied by the mm-wave frequency band, which corresponds to 1 mm to 10 mm wavelength [4]. Due to the small wavelength at mm-wave frequencies, the antennas have a physical compact size, which significantly increases the integration of antennas with RF systems. In addition, mm-wave frequencies can allocate larger bandwidth to wireless communication systems compared to the congested spectrum in the sub-6GHz [5, 6].

To satisfy the high data rate demands, the channel capacity of wireless communication systems must be increased. According to the Shannon-Hartley theorem, the larger bandwidth, the more

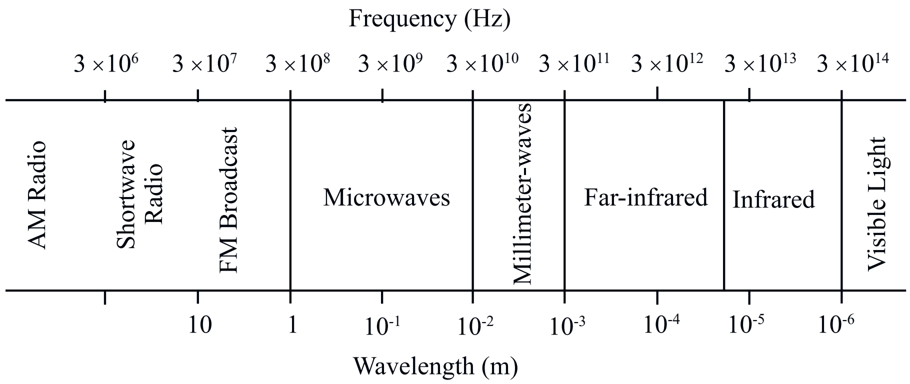

Figure 1.1: The electromagnetic spectrum [6].

capacity, and higher data rate channels have [7]:

$$C = BW \log_2(1 + SNR) \tag{1.1}$$

Where C is the channel capacity (bits per second), BW is the channel bandwidth in Hz, SNR is the signal-to-noise ratio. As it is evident from 1.1 the channel capacity linearly increases with increasing the channel bandwidth, and it grows logarithmically with improving the SNR.

In order to keep up with the demand for the high data rate, antennas as a vital component of every communication systems are demanded to be broadband. Various types of wideband mm-wave antennas have been proposed so far [8–15]. Among such antennas, CP (circularly polarized) antennas are preferred to LP (linearly polarized) antennas due to their distinct advantages, such as reducing polarization mismatch loss due to misalignment between transmitter and receiver antennas and suppressing multi-path interference as a result of reflecting the signal from the ground and surrounding objects [16]. Therefore, wideband CP antennas are highly required for 5G mm-wave communication systems.

1.1 Problem Statement and Motivation

Spiral antennas are low profile antennas that are able to generate circularly polarized (CP) radiation in a large frequency bandwidth due to their inherent frequency-independent (FI) characteristics

[17]. Owing to these desirable features, they have attracted significant attention over the past several decades in microwave frequencies. The usage of balun circuits is inevitable if the spiral antenna is excited in a balanced mode. In order to benefit from the inherently wideband feature of spiral antennas, balun must have the same frequency response as them [18]. Traditionally, balun circuits are bulky and complicated and make the spiral antenna unfavorable for mm-wave communication systems where compactness and lightweight is a crucial requirement. Therefore, a compact feeding mechanism for spiral antennas is an absolute necessity. To our knowledge, there are a few publications about spiral antenna at mm-wave bands, which might be due to their dependency on the complex balun circuits. In this research, we aim to address this issue by employing planar and simple feeding techniques.

In order to increase the link budget between the transmitter and receiver antennas, CP antennas with higher gain are desired. The sequential rotation (SR) feeding technique is a well-known approach for designing CP arrays. The traditional technologies for the implementation of SR feeding networks at low frequencies are not appropriate for mm-wave frequencies. Microstrip lines benefit from high integration level and conformability. Nevertheless, they suffer from spurious radiation and dielectric loss in mm-wave frequencies. Substrate integrated waveguide (SIW) structures have the advantages of planar compatibility and low parasitic radiation due to their self-consistent electrical shielding feature. However, they still have the weakness of high dielectric loss in mm-wave frequencies. In addition, the SIW-based SR feeding networks have commonly adopted the multilayer coupling method, which in turn introduces additional losses and increases the fabrication complexity.

To tackle the problem of high insertion loss and parasitic radiation from feeding networks, Ridge gap waveguide (RGW) guiding structures have been introduced. The printed version of ridge gap waveguide called printed ridge waveguide (PRGW) is a good alternative to Microstrip lines and SIWs in mm-wave frequencies due to its PCB-based structures [19]. The performance of PRGW is similar to the Microstrip line, but due to its excellent shielding feature, it does not suffer from radiation leakage. The antennas arrays implemented by PRGW technology have higher radiation efficiency. Moreover, their compatibility with PCB (Printed circuit board) fabrication process makes them low cost and lightweight. Due to the mentioned benefits, PRGW has been selected as a guiding structure in this research.

1.2 Objective

The concentration of this thesis is to study, design, and develop wideband single/dual circularly polarized antennas at mm-wave frequency band using PRGW technology. The structure's wideband performance, simplicity, fabrication cost, high integration, and loss are considered critical factors in all CP antenna designs. The objectives of this thesis are summarized as follows:

- A cavity-backed slot spiral antenna is designed. The slot spiral arms are fed differentially using the backed-cavity. Then the antenna elements are integrated with the SR feeding network for the AR and gain enhancement. The SR feeding network is implemented using the low-loss PRGW lines. In addition, a wideband transition from a 50-ohm microstrip line to the PRGW line is developed for the sake of measurement.

- A broadband mm-wave SR CP antenna array using compact Archimedean spiral antennas with a differential feeding technique is developed to achieve wider bandwidth compared to the previous work.

- The design methodology of the SR antenna array using LP radiating elements is reviewed. The 45° slant-polarized ME dipole antenna is designed. The PRGW dual CP feeding network components, including rat-race coupler, 3-dB directional coupler, and crossover are designed first and then combined to form the dual-port feeding network with the capability of producing the output signals with equal magnitude and $\pm 90^{\circ}$ difference.

1.3 Main Contributions

The main contribution of this research are listed as follows;

- Design of the wideband, low profile CP slot spiral antenna array using PRGW SR feeding [20].

The traditional feeding mechanism of slot spiral antennas with complicated balun structures adds considerable size to the whole system and therefore makes them inappropriate for mm-wave frequencies. We proposed a simple method to excite the slot spiral antenna. Exciting slot spiral arms with a coupling slot on the backed cavity make the low antenna profile and compatible with PCB fabrication technology. The proposed design archives -10 dB impedance bandwidth of 23.7%, the 3-dB AR of 22.5%, and radiation efficiency of better than 88%.

- Design of the wideband CP antenna array using spiral antennas and PRGW SR feeding [21].

  Spiral antennas are attractive candidates for broadband applications due to their traveling wave structures. However, to benefit from their wideband CP performance, they need to be electrically large enough. Having an electrically large antenna element in an array configuration at millimeter-wave frequencies (considering the grating lobe limit of one wavelength) is almost impossible. On the other hand, compactness is a crucial requirement for the mm-wave antennas as they need to be fitted into a small area in a package or on a chip. Some techniques introduced in the literature to reduce the size of the spiral antenna such as utilizing unequal arm lengths. However, due to perturbing the symmetry of the spiral arms, the antenna radiates a tilted beam from the broadside direction. We proposed a two-arm spiral antenna with a smaller size compared to conventional spiral antennas with several turns without ruining the symmetry of the antenna. The designed antenna array has a wide impedance bandwidth of over 48.5%, the 3-dB AR bandwidth of 34.2%, the 3-dB gain bandwidth of 32.4%, and excellent radiation efficiency of 85% over the entire operating frequency band.

- Design of the wideband dual CP antenna array by employing LP elements in two-port PRGW SR feeding network [Manuscript is submitted to IEEE Trans. Antennas Propag. , 2022.]

  Several millimeter-wave dual circularly polarized antennas are proposed in the literature based on microstrip line and substrate integrated waveguide technologies. However, they suffer from high dielectric loss at high frequencies, resulting in the low radiation efficiency of the antennas. We proposed a wideband dual circularly polarized antenna based on a PRGW SR feeding to obtain high radiation efficiency. Compared to the SIW-based dual-polarized feeding networks, the proposed feeding network is simplified by removing the additional phase shifters and dummy ports. In addition, the high cross-polarization discrimination (XPD) of a dual-polarized array by utilizing the 45° slant polarized radiating elements. The proposed dual CP antenna array provides the -10 dB impedance bandwidth of 22.2%, 3-dB AR bandwidth of 21.6%, and radiation efficiency of better than 90% from excitation of input ports.

1.4 Organization of the Thesis

This thesis is organized into six chapters as follows;

Chapter 1 contains a brief introduction and motivations of the research. In addition, the main contributions of this thesis are presented.

Chapter 2 provides a literature review on circular polarization and sequential feeding technique. Furthermore, as PRGW technology is used for the implementation of feeding networks in this thesis, the essential background of PRGW and different types of gap waveguide technology are presented.

Chapter 3 investigates a low-profile wideband cavity-backed slot spiral antenna fed by SR based on PRGW. The role of the cavity in suppressing the mutual coupling and improving the CP performance of the 2×2 AR array is discussed. The bandwidth of the proposed cavity-backed slot antenna array is increased with the help of the SR feeding technique. The measured results are presented.

Chapter 4 gives the design of a wideband CP antenna array using a compact two-arm Archimedean spiral antenna fed by the SR feeding network. The design procedure and working mechanism of the spiral antenna are given in detail. Then, the performance of the designed SR feeding network is thoroughly investigated. Finally, The measured results of the prototype are demonstrated and compared with other mm-wave CP antenna arrays in the literature, including the CP antenna designed in Chapter 3 of this thesis.

Chapter 5 presents a wideband dual CP antenna array implemented by PRGW technology. The working principle and the design method of the dual CP feed network are described first. Then the wideband LP ME dipole antenna is presented. The 2×2 sequential arrangement of ME dipole antennas is combined with the feeding network. Lastly, the performance of the designed dual CP antenna array is experimentally verified, and comparisons with other reported mm-wave CP antennas are given.

Chapter 6 summarizes the entire research work by highlighting the contributions of the proposed mm-wave CP antennas and suggests some possible future directions of this research topic.

Chapter 2

Theoretical Background and Literature Review

2.1 Introduction

This chapter presents a literature review in two major parts. First, the concept of circular polarization is discussed, and then a theoretical review of two types of CP traveling-wave antennas (i.e., spiral and slot spiral antenna) and the sequential rotation feeding technique is investigated. Spiral and slot spiral antenna are chosen as radiating elements in Chapters 3 and 4, and the sequential feeding network is deployed with both CP and LP antennas in chapters 3, 4, and 5. In the second part, the background of the gap waveguide guiding structures is provided. Feeding networks presented in this thesis are implemented using printed ridge gap waveguide (PRGW) technology.

2.2 Circular Polarization

Polarization is defined by the direction of the electric field vector in the transverse plane as a function of time [22]. There are three main types of polarizations (i) linear polarization, (ii) circular polarization, (iii) elliptical polarization, as shown in Fig. 2.1. For the circular polarization, the tip of the electric field vector rotates an angle of 2π in the x-y plane as time varies over a period of T [23] (Fig. 2.1 b).

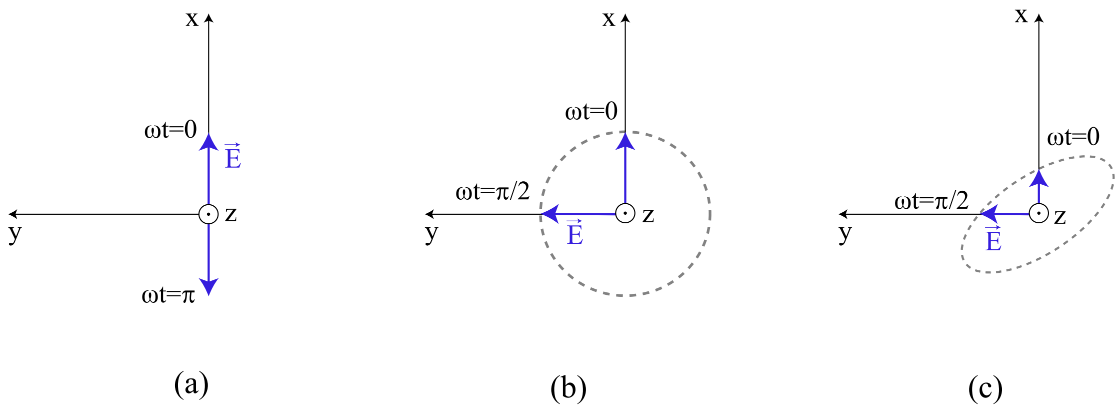

Figure 2.1: Polarization examples (a) Linear Polarization, (b) Circular Polarization, (c) Elliptical Polarization.

CP wave is called RHCP ((Right Hand Circularly Polarized); if the electric field rotates clockwise, and it is called LHCP (Left Hand Circularly Polarized), if the electric field rotates counterclockwise. E_L and E_R are RHCP and LHCP components of the electric field and can be written as [23]:

$$E_L = \frac{E_x - jE_y}{\sqrt{2}} \tag{2.1a}$$

$$E_R = \frac{E_x + jE_y}{\sqrt{2}} \tag{2.1b}$$

Where E_x and E_y are transverse components of a z-travelling wave in the far field:

$$\vec{E} = (E_x\hat{x} + E_y\hat{y})e^{-jkz} \tag{2.2a}$$

$$E_x = |E_x|\, e^{j\phi_x} \qquad E_y = |E_y|\, e^{j\phi_y} \tag{2.2b}$$

If $|E_x| = |E_y|$ and $\phi_y - \phi_x = -\frac{\pi}{2}$, $E_L = 0$ and RHCP wave is excited. If $|E_x| = |E_y|$ and $\phi_y - \phi_x = \frac{\pi}{2}$, $E_R = 0$ and LHCP wave is excited.

The quality of CP wave is measured by axial ratio (AR) which is defined by the following equation [24].

$$(AR)_{dB} = 20log\left[\frac{|E_R| + |E_L|}{\Big|\,|E_R| - |E_L|\,\Big|}\right] \tag{2.3}$$

From the above equation, it is known that if E_R or $E_L = 0$, then AR=0 dB and the wave is pure CP. The polarization of practical CP antennas is generally elliptical, and $AR \leq 3dB$ is acceptable in most applications.

$AR \neq 0$ caused by unequal amplitudes of two electric field components (amplitude error), and their phase difference deviation from 90° (phase error). Amplitude error (A_e) and phase error (θ_e) are calculated by:

$$A_e = \frac{|E_y|}{|E_x|}, \qquad A_e(dB) = 20\ log(A_e) \tag{2.4a}$$

$$\phi_y - \phi_x = \pm\frac{\pi}{2} \pm \theta_e \tag{2.4b}$$

Fig. 2.2 shows the effect phase error (θ_e) and amplitude error ($Ae(dB)$) on AR. As it can be seen from this figure, when $\theta_e = 0$ then $AR(dB) =\mid A_e(dB) \mid$. Furthermore, AR deteriorates by approximately 0.16 dB for each degree of phase error. Therefore, in order to have the $AR \leq 3dB$, we need:

$$|(A_e)dB| < 3dB, \qquad \text{when} \qquad \theta_e = 0 \tag{2.5a}$$

$$\theta_e \leq 18.9^\circ, \qquad \text{when} \qquad A_e(dB) = 0 \tag{2.5b}$$

The approximate formula to calculate AR when we have both A_e, and θ_e is given in [25]:

$$(AR)_{dB} = \sqrt{A_e(dB)^2 + 0.0225\theta_e^2} \tag{2.6}$$

Generally, there are two types of circularly polarized antennas: (1) circular polarized antennas due to their structure such as helix and spiral (2) Circularly polarized antennas due to the excitation

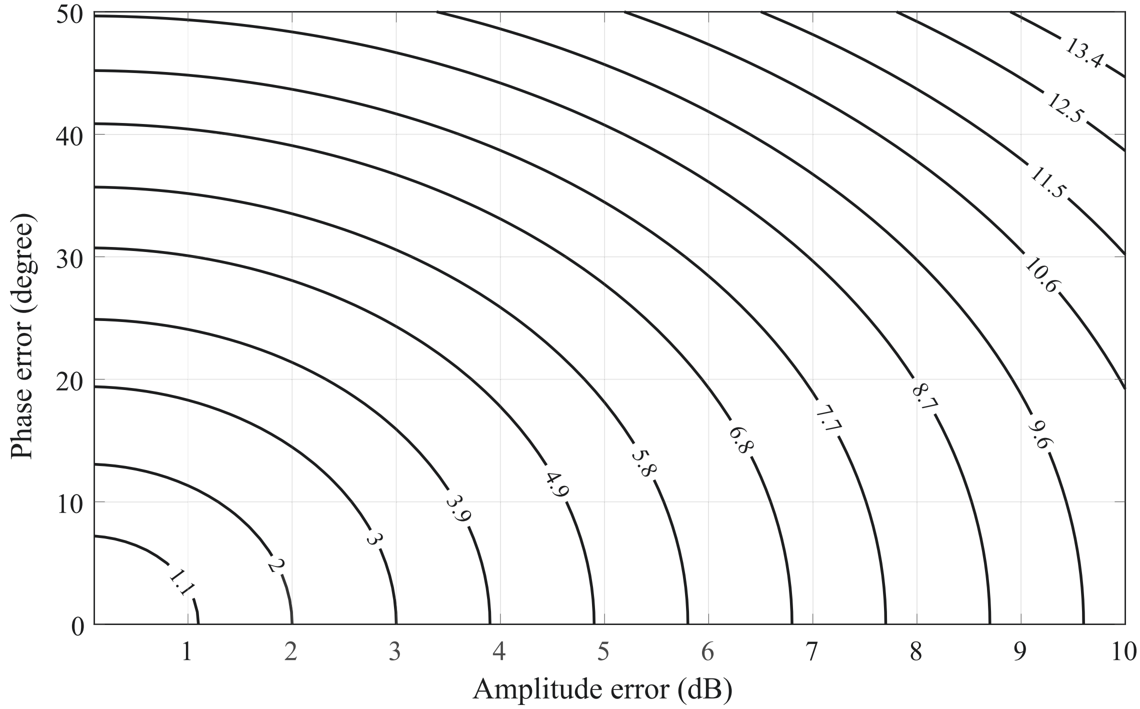

Figure 2.2: Contour plot of AR (dB).

of two orthogonal electric field components with the same magnitudes and 90° phase difference [24].

Various CP antennas at mm-wave frequencies have been reported in the literature, such as patch [26, 27], cavity-backed slot [28, 29] dielectric resonator [30, 31] and aperture antennas [32]. However, the majority of them suffer from either narrow CP bandwidth or complicated and large size of feeding structures. Over the years, helical and spiral antennas have become increasingly popular due to their wide AR bandwidth [33]- [34]. They can generate CP waves due to their unique shape. Helical antennas own 3D geometry, which makes them inappropriate for mm-wave fabrication. However, their fabrication can be realized by using the costly LTCC (low temperature cofired ceramic) fabrication process to implement the helix antenna in a multilayer structure [35]. Therefore, spiral antennas are preferred to helical antennas as they possess planar geometry and conformal characteristics.

2.3 Spiral Antenna

The spiral antennas were first introduced by Rumsey in 1955 [36]. They have been classified into a group of "frequency-independent (FI) antennas" in which the antenna performance is consistent over a wide frequency range. According to Rumsey's work, this feature would happen for those antennas that their geometries are defined only by an angle that makes them invariant to the scaling transformation. Practically, the FI antenna can achieve over 10:1 broad bandwidth [18, 36]. The sense of polarization of the spiral antenna is determined by the direction of the spiral windings. The planar type of spiral antenna can be fabricated using PCB technology. The most common types of planar spiral antennas are (1) Equiangular spiral antenna (2) Archimedean spiral antenna (Fig. 2.3).

The Equiangular spiral antenna was first developed by Dyson in 1958 [37]. The two arms for the equiangular spiral curves are described by two equations in polar coordinate as [38]:

$$r = r_0 e^{a\theta} \qquad \theta_{st} \le \theta \le \theta_{end}, \tag{2.7a}$$

$$r = r_0 e^{a(\theta-\pi)} \qquad \theta_{st} + \pi \le \theta \le \theta_{end} + \pi, \tag{2.7b}$$

Where r_0 is the initial radial distance from the origin, a is the spiral constant, and θ is the winding angle. Since the angle between the radial vector and tangent is constant for each point on the spiral curve ($\psi = \tan^{-1}(\frac{1}{a})$), this curve is called equiangular.

A two-arm Archimedean spiral was first proposed by Kaiser in 1960 [17]. The geometry of the two-arm Archimedean spiral is shown in Figure 2.3. The spiral curves in polar coordinate are defined by [38]:

$$r = r_0 + a\theta \qquad \theta_{st} \le \theta \le \theta_{end}, \tag{2.8a}$$

$$r = r_0 + a(\theta - \pi) \qquad \theta_{st} + \pi \le \theta \le \theta_{end} + \pi, \tag{2.8b}$$

Where r_0 is the initial radial distance from the origin, a is the spiral constant, and θ represents the winding angle.

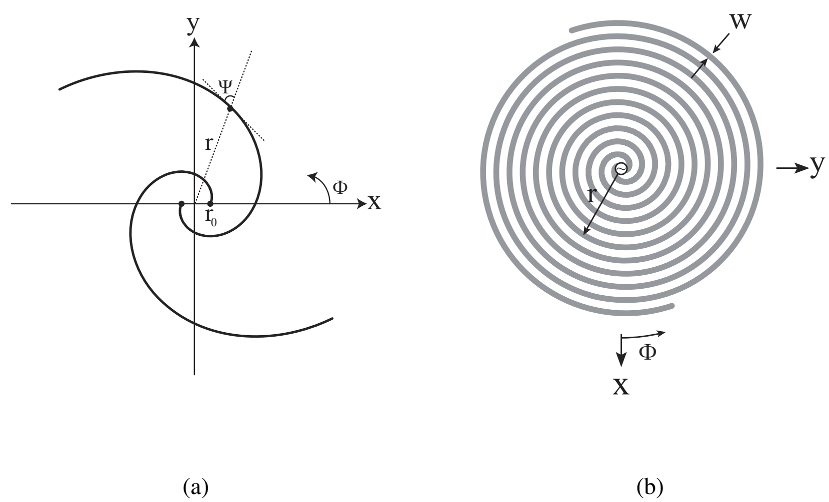

Figure 2.3: (a) Equiangular spiral curve, (b) Two-arm Archimedean spiral antenna [24].

2.3.1 The Principle of Operation

Generally, for an N-arm spiral antenna, $N-1$ independent mode can be excited if the arms are excited with equal magnitude and phase difference of $\frac{2\pi m}{N}$, where m is the desired mode of operation. Fig.2.4 shows the resulting radiation pattern of each mode. As it can be observed from this figure, except for the first mode, all modal patterns have null in the boresight direction. It is

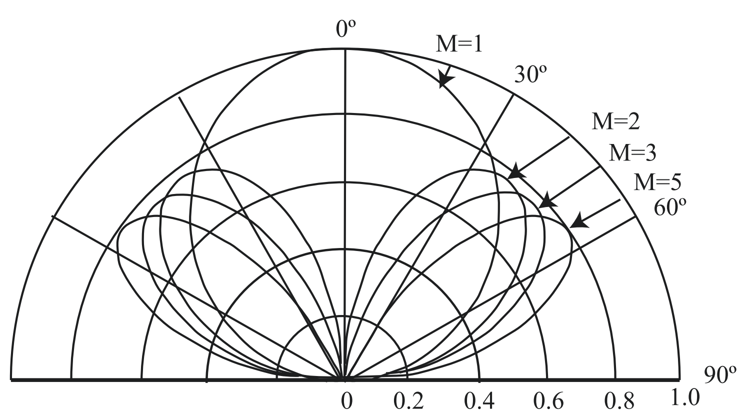

Figure 2.4: Mode patterns for a spiral antenna [18].

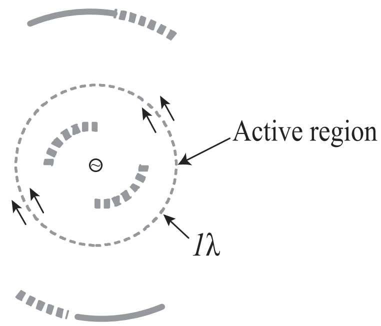

Figure 2.5: Active region (m=1) shown in two-arm Archimedean spiral antenna [24].

worth mentioning that, for each balanced mode, the radiation will occur in a ring of circumference $m\lambda$ which is known as "active region" (Fig. 2.5). When the currents of each mode, which are initially out of phase by $\frac{2\pi m}{N}$, reach an active region will become in phase, and that leads to the radiation of a CP wave [39]. The operating frequency of the spiral antenna is determined by the inner and outer radius of the spiral curve. The frequency response of the antenna also depends on the spiral constant (a in equation 2.7and 2.8).

In order to excite a two-arm spiral antenna with the balanced mode, a balun circuit is required. A balun is a balanced feeding structure that makes the output currents equal in magnitude and opposite in phase [40]. The conventional types of balun add notable complexity and volume to the antenna structure [41, 42].

2.4 Sequential Rotation Feeding Technique

The Sequential-rotation (SR) feed technique was first described by Teshirogi et al. [43]. This method has been widely used to broaden the AR bandwidth of array antenna in which each antenna element undergo both progressive phase shift and physical rotation [44–46]. Fig. 2.6 shows the configuration of the N-element sequentially rotated antenna array. The m_{th} radiating element in the sequential array configuration has angular rotation and phase shift of ϕ_m, which is obtained by [47]:

$$\phi_m = \frac{P(m-1)\pi}{M} \quad 1 \leq m \leq M \tag{2.9}$$

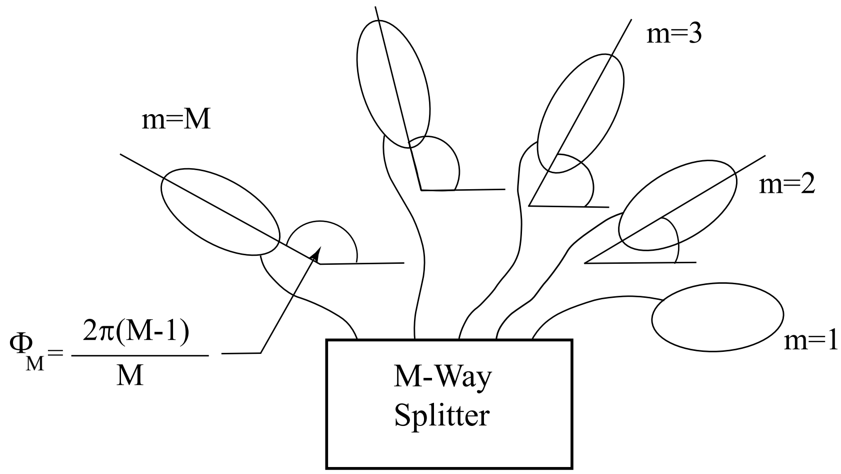

Figure 2.6: Principle of sequentially rotated feeding [47].

Where M is the total number of radiating elements and P is an integer and determines the angular variation of each element and $1 \leq P \leq M-1$. Various sequential-rotation configurations can be made by assuming different values for M and P as summarized in [48]. Due to the simplicity and compactness of the feeding network for providing $90°$ and $180°$ phase offsets using hybrids, as well as the rotational symmetry of radiation pattern, the 2×2 sequentially rotated antenna array (where M=4 and P=2 in equation 2.9) has attracted more attention [49]. Two senses of CP wave (RHCP are LHCP) are generated depending on the direction of phase increments in the sequential configuration. Fig. 2.7 shows the required phase shift for each radiator in the 2×2 sequentially rotated configuration.

The sequential rotated antenna array radiates CP wave in an on-axis direction ($\theta = 0°$) regardless of the polarization of the antenna elements as it is shown in Appendix A; therefore, it can be used with both LP and CP radiating elements [50, 51]. Due to unavoidable amplitude and phase errors of the sequential feeding networks, CP radiating element in sequential arrangement exhibits higher CP purity, broader AR, and gain bandwidth compared to LP elements in sequential feedings. However, the usage of LP elements in sequential feeding is beneficial for switching the sense of circular polarization [52] or generating dual CP dual-beam [53] from shared aperture arrays.

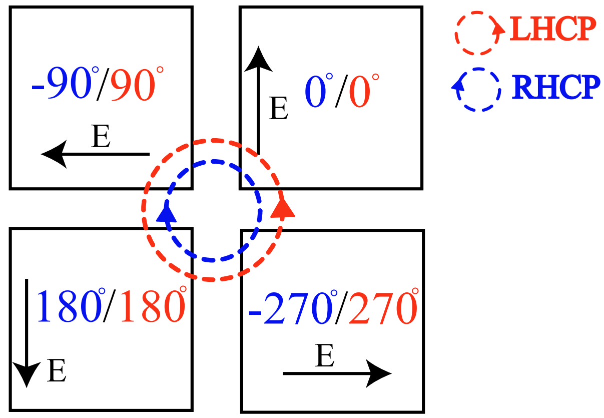

Figure 2.7: Phase distribution for RHCP and LHCP.

2.4.1 Sequential Rotation with Linearly Polarized Elements

To explain the operating principle of SR with LP elements, the array factor of SR 1×2 LP array antenna, in which antenna elements are placed at the distance of d on the y axis, is derived. The electric field radiated from an LP element at far field can be decomposed into two CP components:

$$\vec{E} = (E_R\hat{e}_R + E_L\hat{e}_L)\frac{e^{-jkR}}{R} \tag{2.10}$$

Where $\hat{e}_R$ and $\hat{e}_L$ are normalized unit vectors for RHCP and LHCP waves and are defined as:

$$\hat{e}_R = \frac{\hat{x} - j\hat{y}}{\sqrt{2}} \tag{2.11a}$$

$$\hat{e}_L = \frac{\hat{x} + j\hat{y}}{\sqrt{2}} \tag{2.11b}$$

Therefore, the radiated electric field from two LP elements in Fig. 2.8 can be written as:

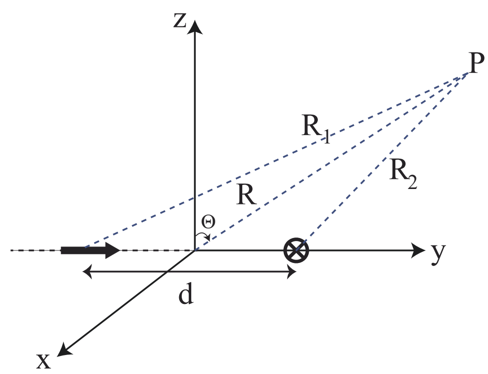

Figure 2.8: Two LP elements radiation in the yz plane.

$$\vec{E_1} = (E_R\hat{e}_R + E_L\hat{e}_L)\frac{e^{-jkR_1}}{R_1} \tag{2.12a}$$

$$\vec{E_2} = e^{j\alpha}(E_Re^{j\beta}\hat{e}_R + E_Le^{-j\beta}\hat{e}_L)\frac{e^{-jkR_2}}{R_2} \tag{2.12b}$$

Where R_1 and R_2 are the distance from LP elements to the observing point P in the far field, α and β are the applied excitation and geometrical phases, respectively, to the second element. The effect of geometrical rotation on electric field components can be obtained by Rodriges's formula [54] as explained in equation A.4

Using superposition theory and far-field approximation the total electric field can be written as:

$$\vec{E_T} = (E_R\hat{e}_R + E_L\hat{e}_L)\frac{e^{-jk(R+\frac{d}{2}sin\theta)}}{R} + (E_Re^{j(\alpha+\beta)}\hat{e}_R + E_Le^{j(\alpha-\beta)}\hat{e}_L)\frac{e^{-jk(R-\frac{d}{2}sin\theta)}}{R} \tag{2.13}$$

$$\begin{aligned}\vec{E_T} = \frac{e^{-jkR}}{R}(E_R\hat{e}_R(e^{-jk(\frac{d}{2}sin\theta)} + e^{j(\alpha+\beta)}e^{jk(\frac{d}{2}sin\theta)} \\ +E_L\hat{e}_L(e^{-jk(\frac{d}{2}sin\theta)} + e^{j(\alpha-\beta)}e^{jk(\frac{d}{2}sin\theta)})\end{aligned} \tag{2.14}$$

For the generation of RHCP wave, $\alpha = -90°$ and $\beta = 90°$, thus the total electric field can be expressed as:

$$\vec{E_T} = (E_R AF_R \hat{e}_R + E_L AF_L \hat{e}_L)\frac{e^{-jkR}}{R} \tag{2.15}$$

Where AF_R and AF_L are the array factor for RHCP and LHCP waves in the yz plane, respectively and are defined as:

$$AF_R = 2cos(\frac{kd}{2}sin\theta) \tag{2.16a}$$

$$AF_L = 2jsin(\frac{kd}{2}sin\theta) \tag{2.16b}$$

The normalized array factors are:

$$AF_R = cos(\frac{kd}{2}sin\theta) \tag{2.17a}$$

$$AF_L = sin(\frac{kd}{2}sin\theta) \tag{2.17b}$$

From equation 2.17a and 2.17b, it can be seen that at the broadside direction (in the y-z plane), the AF_R is maximum and AF_L is minimum, but as angle θ is increasing, AF for the cross-polarization (i.e AF_L) is increasing to reach its maximum value at the off-broadside angle.

Fig. 2.9 illustrates the CP radiation pattern of 1×2 sequential rotated antenna array in the plane where two LP elements are located. It should be noted that the cross-polarization level at the plane perpendicular to the plane containing LP elements is acceptable. Therefore, by expanding the linear array to the planar array (Fig. 2.10 a), the cross-polarization level improves significantly in xoz- and yoz-planes. However, the 2×2 sequential array in Fig. 2.10 a has high cross-polarization sidelobe levels at the diagonal plane. To fairly reduce the cross-polarization side lobe levels, sequential arrangement shown in Fig. 2.10 b is used. [55, 56].

It is worth mentioning that, these lobes are dependent on the element spacing. Therefore, the gain loss of sequentially rotated LP elements can be controlled by the element spacing. The maximum element spacing of $0.7\lambda_0$ ($1\lambda_0$ spacing in the diagonal plane) is considered to avoid high

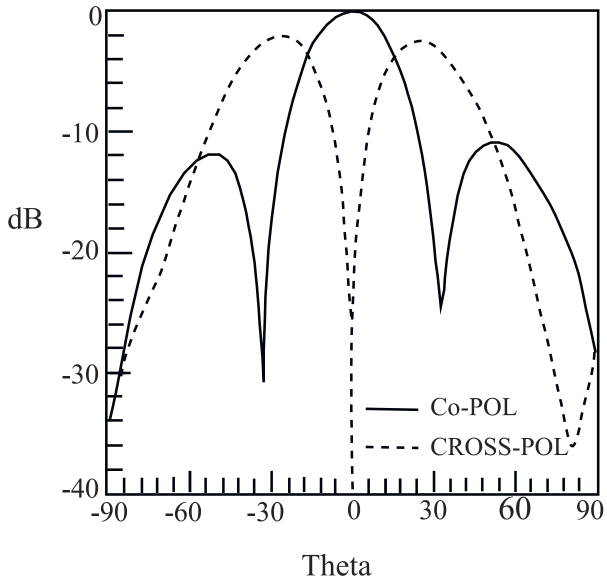

Figure 2.9: Calculated CP patterns of the two-element array with element spacing of 0.87λ [55].

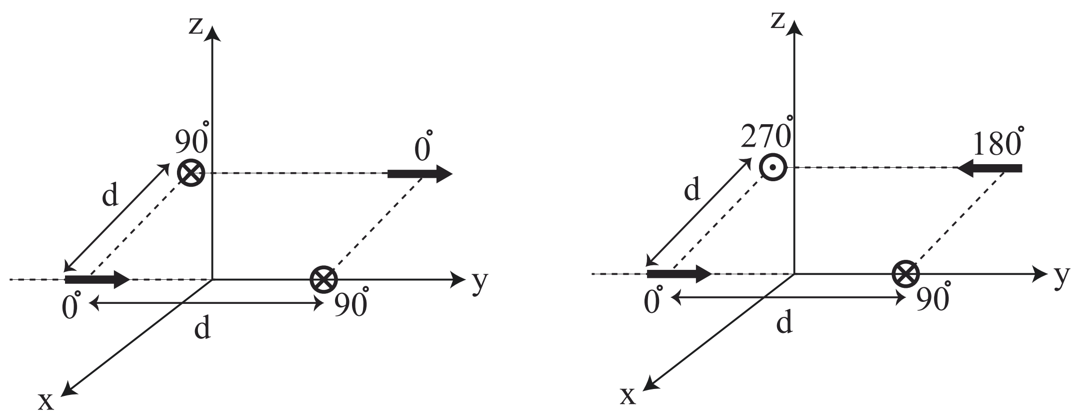

(a) (b)

Figure 2.10: 2×2 sequentially rotated subarray, (a) arrangement to suppress the cross-polarization at $\phi = 0°$ and $\phi = 90°$ planes, (b) arrangement to suppress the cross polarization at $\phi = 0°$, $\phi = 90°$, and $\phi = \pm 45°$ planes.

cross-polarized lobes in the diagonal planes. [57–59].

2.4.2 Implementation of Sequential Feeding with Different Technologies

The sequential rotation feeding scheme has been implemented with different feeding technologies for mm-wave applications, including microstrip line (MSL)[60, 61], LTCC [62, 63], and SIW [64, 65]. MSL was most popular at low frequencies due to such advantages as compactness, design flexibility, and low cost of fabrication. However, they usually suffer from radiation losses, which is more severe at high frequencies [66]. In addition, the parasitic radiation from microstrip feed networks has an adverse effect on the total radiation pattern of the antenna array. Radiation leakage and undesirable spurious radiation of the feed network is minimized in SIW since it is a self-package structure. But, they have some issues. Apart from a high dielectric loss at mm-wave frequencies, which makes the SIW less efficient compared to air traveling structures, it is not suitable for the realization SR feed network due to the large size of 3dB quadrature hybrid couplers and phase shifters. Recently, a multilayer aperture coupled approach is utilized to alleviate this problem [67]. However, the multilayer design adds more losses and difficulties in fabrication, particularly for large arrays (Fig. 2.11). PRGW technology is a promising alternative for microstrip lines at high frequencies [68, 69]. It's a compromise between the microstrip line and SIW as it is a package structure and suppresses the radiation loss and also has design flexibility, which is highly desirable for the implementation of the SR feeding network.

2.5 Challenges in Conventional Guiding Structure

The conventional guiding structure at microwave such as how waveguides, substrate integrated waveguides (SIW) and microstrip and strip lines have some inventible problems at mm-wave frequencies. The hollow waveguides (rectangular and circular) are the most common guiding structure at microwave frequencies. However, due to the poor electrical contacts between waveguide walls and resulting field leakage, hollow waveguides are problematic despite being a low loss. The main issue with microstrip and SIW is that they have the problem of severe dielectric loss at mm-wave frequencies. Moreover, microstrip lines suffer from high radiation loss, which significantly decreases the radiation efficiency of the antenna, particularly at mm-wave frequencies [66]. Furthermore, the spurious radiation from the microstrip feeding network has a detrimental effect on the antenna's

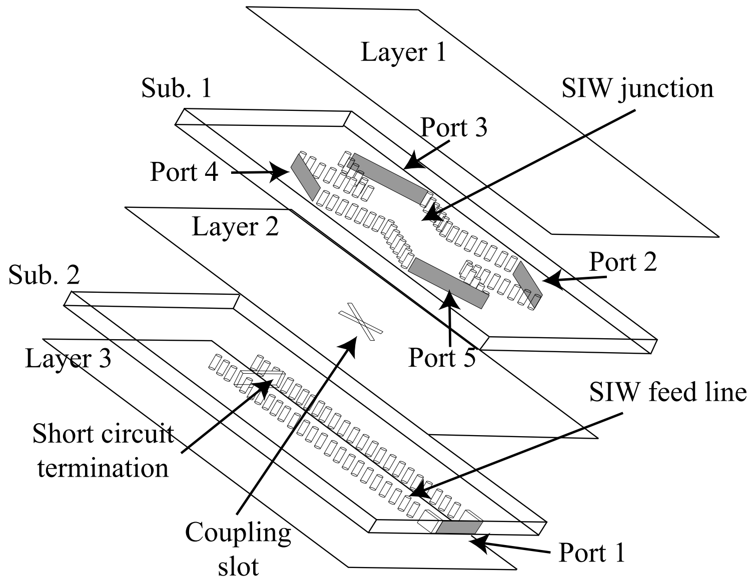

Figure 2.11: SIW SR feeding network [67].

radiation pattern. SIW could be an appropriate alternative to the microstrip lines at mm-wave frequencies if they did not have the problem of severe dielectric loss [70]. Besides, the bandwidth of the feeding networks, which are implemented by SIW technology, is limited by the cutoff frequency of the second propagating mode. Recently, based on the definition of soft and hard surfaces, the gap waveguides have been introduced, which have a better performance compared with the conventional guiding structure at mm-wave frequencies [68].

2.5.1 Soft and Hard Surfaces

The concept of soft and hard surfaces was first introduced in [71] and [72]. They are called soft and hard surfaces based on the analogy with soft and hard surfaces in acoustics [73]. They also referred to metamaterials as their proprieties cannot be found in nature and can only be made artificially. The hard surfaces are the artificial surfaces that allow the propagation, whereas soft surfaces are the surfaces that stop the propagation. The corrugated surface acts simultaneously as a hard surface in the direction of propagation and as a soft surface in the transverse direction, as shown in Fig. 2.12. It should be pointed out, the length of corrugated surfaces is a quarter

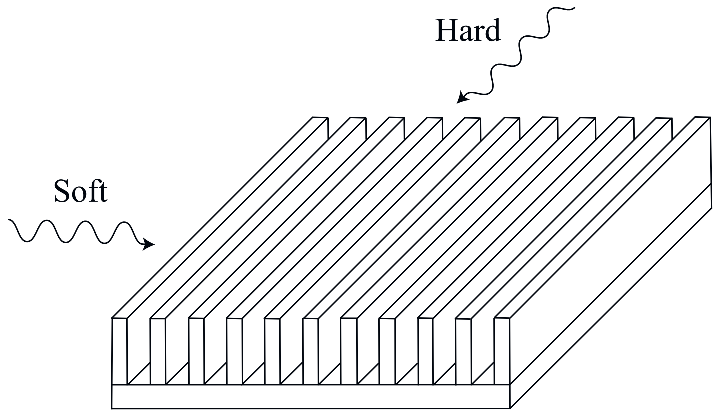

Figure 2.12: Realization of soft and hard surfaces in corrugated metal slab.

wavelength. Therefore the zero impedance of PEC surface is transformed to a high impedance (PMC) that prohibits the wave propagation along the direction of propagation for soft surfaces.

2.5.2 Gap Waveguide Technology

Fig. 2.13 shows the basic theory of gap waveguide structures. The principal operations of gap waveguides are based on confining electromagnetic fields to the desired path and suppression of undesired electromagnetic waves in the other regions. Suppression of unwanted waves can be realized by using two parallel plates, where one of them is PEC (perfect electric conductor) and the other one is PMC (perfect magnetic conductor). If the distance between the two parallel plates (h in Fig. 2.13) is less than 0.25λ, then all the modes are below their cutoff frequencies and only evanescent waves can exist. It is well known that the PMC environment can be artificially realized by 2D periodic metal pins, which act as quarter wavelength transformers and emulate the behavior of a high impedance surface [72, 74]. Due to the fact that the pin lattice can only provide a high impedance condition in a specific frequency range, the propagation of the electromagnetic wave in the mentioned condition is forbidden only in that specific frequency range which is called stopband.

The gap waveguide structures can be realized in three different versions based on their propagating path: ridge gap waveguide (RGW) [75, 76], groove gap waveguide (GGW) [77, 78] printed

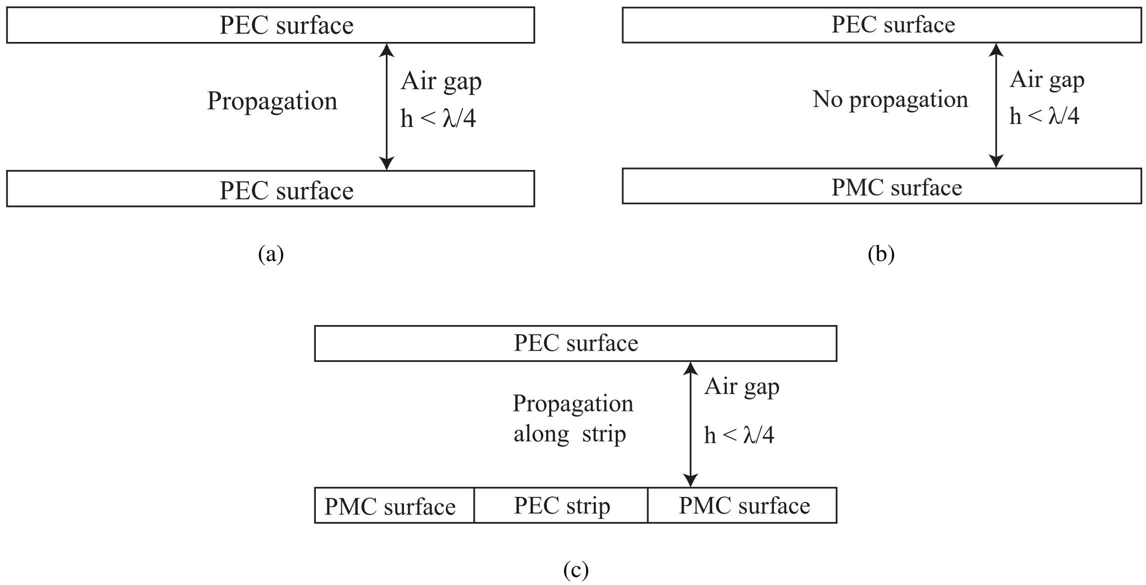

Figure 2.13: Configuration of RGW.

ridge gap waveguide (PRGW) [79, 80], as shown in Fig. 2.14. The groove and ridge gap waveguide can be made without any dielectric. RGW supports Quasi TEM propagating mode in the gap between two parallel plates, and the propagating mode of GGW in the groove is TE and TM. Both RGW and GGW do not require any electrical contacts between the two plates, so they can be a good alternative for rectangular waveguides at high frequencies. Similar to RGW, the quasi TEM mode is allowed to propagate in the gap between the microstrip line and the upper PEC plate of PRGW structures (Fig. 2.15). In this type, the high impedance surface is realized by mushroom-type EBG unit cells. PRGW can be a good alternative for planar transmission lines which are compatible to integrate with other planar circuits on the printed circuit boards (PCB). PRGW has the advantage of lower transmission loss compared to SIWs and microstrip lines as the electromagnetic wave is propagating in the air gap between the microstrip line and the upper PCB layer [81]. Furthermore, the feeding networks that are implemented by PRGW technology are effectively shielded from the radiating parts of the antenna which substantially suppresses the undesired radiations of the feeding network. Generally, there are two types of PRGW: (i) inverted printed gap waveguide [79] (ii) suspended printed gap waveguide [82]. For the first one, the microstrip line and AMC layer are in the same layer and the line is grounded by metalized vias, whereas for the second one, the microstrip

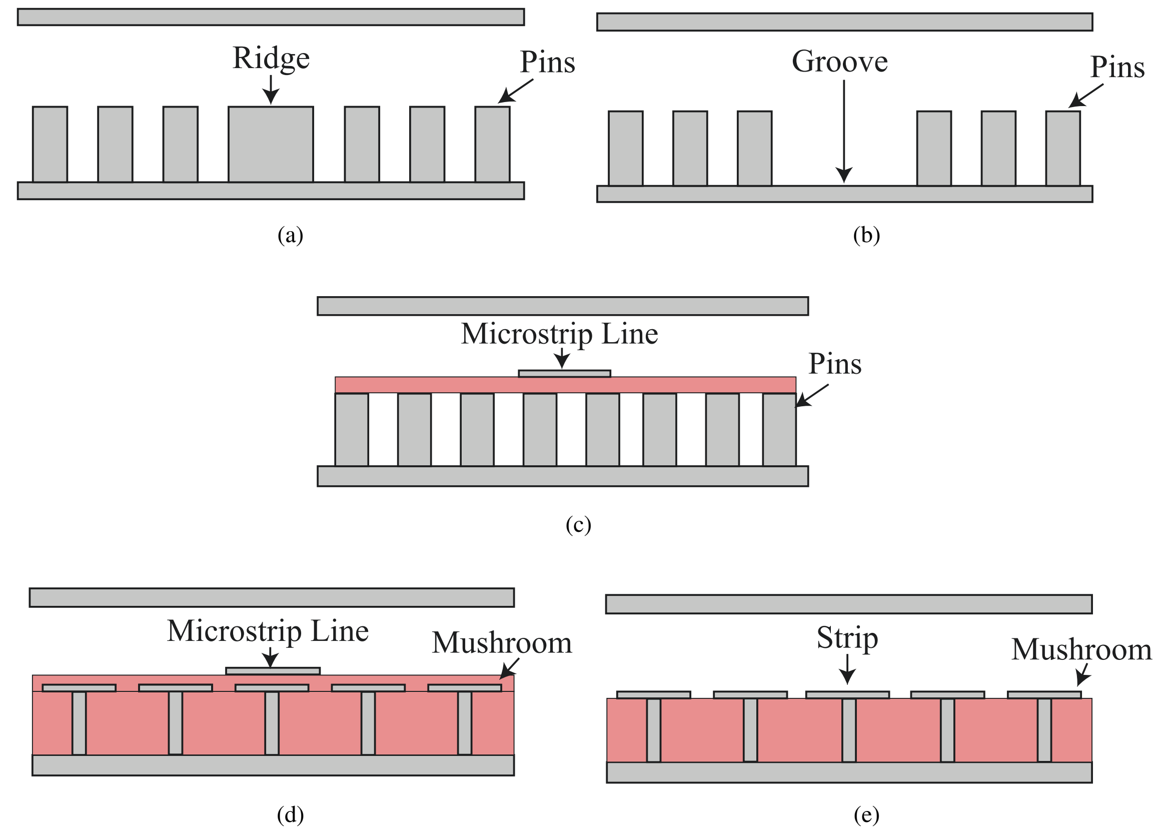

Figure 2.14: Different types of gap waveguide structures, (a) Ridge gap waveguide, (b) Groove gap waveguide, (c) Microstrip gap waveguide, (d) Inverted gap waveguide, (e) Suspended gap waveguide.

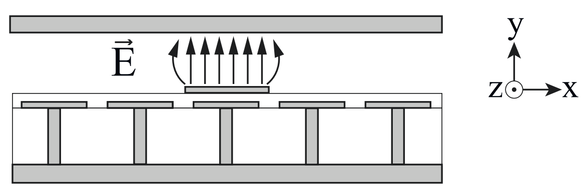

Figure 2.15: Electric field lines of the quasi-TEM mode.

line is on the upper layer of the AMC Layer. Having a microstrip line on a separate layer gives more freedom to adjust the position of the microstrip line, which is very important in large arrays. The suspended printed gap waveguide has been selected for implementation of the feeding network.

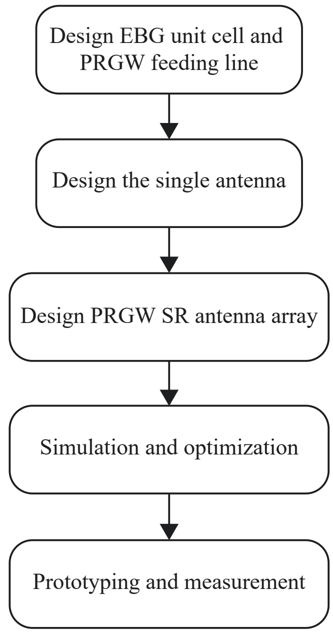

Figure 2.16: Flow chart of the research methodology.

2.6 Research Methodology

The research methodology that is used for designing mm-wave CP antennas based on PRGW is illustrated in Fig. 2.16. The initial step is to develop the EBG unit cell for the desired band stop considering the design requirement. It should be noted that the dispersion diagram of the EBG unit cell is computed using the CST Microwave Studio Eigenmode solver. The next step is to choose the broadband antenna and excite the antenna using the PRGW feeding line. Once the single antenna obtains good performance, it is incorporated into the SR arrangement. The SR antenna array realized by the PRGW feeding network is simulated and optimized using the 3-D EM full-wave software. To facilitate the design testing, a wideband transition from the microstrip line to the PRGW line is employed.

The final antenna array is fabricated based on a multilayer PCB process. The fabricated layers are stacked together using either plastic screws or glue at high temperatures with uniform pressure. An SMA 1492-02A-6 (2.4 mm) southwest Microwave end launch connector is connected to the 50-ohm microstrip line-to-PRGW transition.

The S-parameters of the fabricated antennas are measured using the N52271A programmable network analyzer (PNA). The SOLT (short-open-load-thru) calibration is performed with the Electronic calibration (ECal) module to set the measurement reference plane at the input of the microstrip line. The radiation pattern, gain, and AR of the CP antennas are measured in the anechoic chamber, where the antenna under test (AUT) is placed as a receiver, and the standard horn antenna is placed as a transmitter.

2.7 Summary

In this chapter, the background and design methodology of CP antennas with SR are introduced. Then different techniques for implementation of SR at mm-wave band are briefly reviewed. The state-of-the-art gap waveguide technology is presented, and then three versions of gap waveguides are explained.

Chapter 3

Slot Spiral Cavity-Backed Antenna Array

3.1 Introduction

Among various types of mm-wave CP antennas, helical and spiral antennas are desirable for ultra-bandwidth applications due to their travelling wave (TW) structure. However, the classical types of these antennas are not appropriate for the mm-wave array configurations due to their non-planar geometry and large size [33]-[34]. In [35], the LTCC technology is used to implement the multilayer structure of helical antenna; However, the LTCC fabrication process is costly and challenging. In order to maintain the inherently broadband feature of the spiral antenna, a wideband balun is absolutely vital for the antenna feeding, which in turn adds notable complexity to the overall system [83]. Some alternative feeding techniques have been employed in literature to make the spiral antennas independent of conventional and complicated balun structures. In [84]-[85], the spiral arms are differentially fed by two opposing vias at sides of the slot etched on the backed substrate integrated cavity (SIC). Even though the mentioned works benefits from a simple and planar alternative to the vertical balun structures, the usage of the waveguide feeding mechanism added relatively significant height and weight to the whole system.

In this chapter, a 2×2 cavity-backed slot spiral antenna array with a simple feeding mechanism for mm-wave applications is presented. The cavity-backed slot spiral is easily fed through a single slot etched on the other side of the cavity. Although the proposed antenna element has a narrow AR bandwidth, the deployment of this antenna element in a sequentially rotated array environment results in a high-performance CP antenna array, which is the main objective of this work.

3.2 Antenna Design

3.2.1 Equiangular Spiral Antenna

The single element antenna configuration is depicted in Fig. 3.1, which consists of four layers. The first layer includes the arms of the equiangular slot spiral antenna, which is etched on the top surface of the backed SIC. The cavity is fed by a PRGW feed line through a $3.4mm \times 0.4mm$ coupling slot etched on its bottom surface, as shown in Fig. 3.1a. The length of the slot is calculated using the following formula:

$$L_s = \frac{c}{2 f_{c_{TE120}} \sqrt{\epsilon_e}} \tag{3.1}$$

Where c is the speed of the light in vacuum, $f_{c_{TE120}}$ is the cutoff frequency of TE_{120} mode and ϵ_e is the equivalent permittivity of slot and is obtained by:

$$\epsilon_e = \frac{1 + \epsilon_r}{2} \tag{3.2}$$

The physical dimensions of the proposed single element are summarized in Table 3.1. Each of the equiangular spiral arms are defined by the two functions in polar coordinates:

$$r_1 = r_i e^{(a\theta)}, \qquad r_2 = K r_i e^{(a\theta)} \tag{3.3a}$$

$$r_3 = r_i e^{(a\theta+\pi)}, \qquad r_4 = K r_i e^{(a\theta+\pi)} \tag{3.3b}$$

where r_i is the initial value for r, a is the spiral constant, θ represents the winding angle, starts at θ_{st} and ends at θ_{end} and constant K is defined as $K = \frac{r_2}{r_1} = \frac{r_4}{r_3}$.

The spiral arms are truncated with two circles to alleviate the effect of reflected currents from the arm ends. The spiral antenna will exhibit the travelling-wave behavior if its circumference

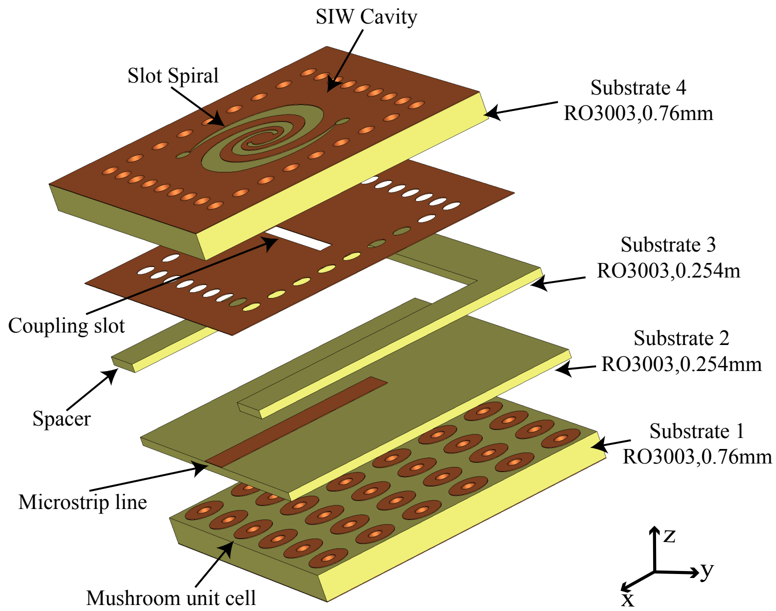

(a)

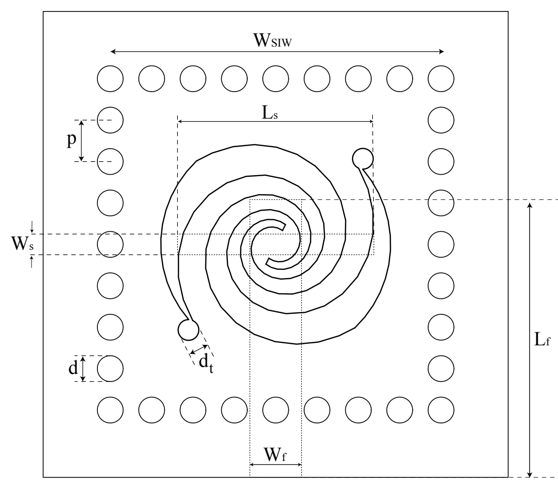

(b)

Figure 3.1: Geometry of the proposed antenna element, (a) Perspective view, (b) Top view.

C ($C = 2\pi r_{max}$, where r_{max} is attributed to the lowest design frequency) is greater than one wavelength at the lowest frequency [39]. Here C is chosen to be $2.7\lambda_g$ approximately. The designed antenna exhibits RHCP due to the direction of spiral arms windings. All layers are made with Rogers 3003 substrate with the dielectric constant of $\epsilon_r = 3$, loss tangent=0.0013, and copper cladding of 17 µm. For the two-arm spiral antenna, the balanced mode is excited if the arms have the same amplitude and 180° phase shift [86].

Table 3.1: Dimension of the proposed single element

Parameter	W_{SIW}	W_f	L_f	Ws	Ls	d	p
Value	6.4	1	5.4	0.4	3.4	0.5	0.8
unit	mm	mm	mm	mm	mm	mm	mm
Parameter	r_i	d_v	a	K*	θ_{st}	θ_{end}	
Value	0.8	0.4	0.22	1.44	0.23	8.9	
unit	mm	mm	mm/rad	-	rad	rad	

* There is no unit for K.

3.2.2 Cavity Excitation

The primary reason to utilize the SIC at the back of the equiangular slot spiral is to provide a unidirectional radiation pattern. The second reason is the differential excitation of the slot spiral arms to have a CP radiation. The radiating arms are fed through a transverse coupling slot, which is etched on the bottom wall of the SIC. In order to have differential electric currents on both halves of the SIC, TE_{120} is chosen to be excited and accordingly the width of SIC is obtained using the following equation [87]:

$$f_{c_{TE120}} = \sqrt{\frac{5}{4}}\frac{c}{\sqrt{\epsilon_r}}(W_{SIW} - \frac{d^2}{0.95p})^{-1} \tag{3.4}$$

Where c is the speed of the light in vacuum, ϵ_r is the dielectric constant, p is the center to center distance between two subsequent vias, d is the via diameter, and W_{SIW} is the width of the SIW cavity. The width of square SIC is chosen to have TE_{120} mode at frequencies higher than

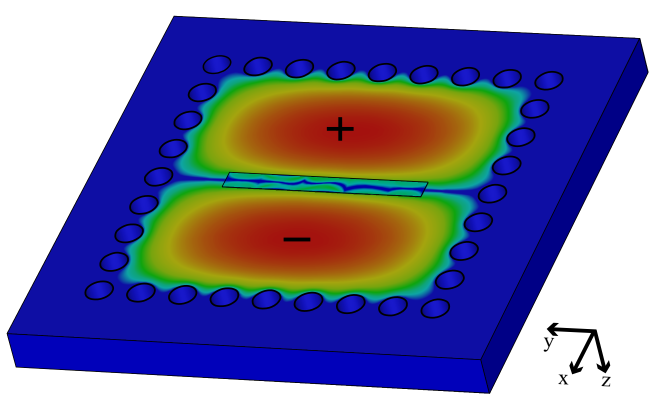

Figure 3.2: Electric field distribution in the SIC at 32 GHz.

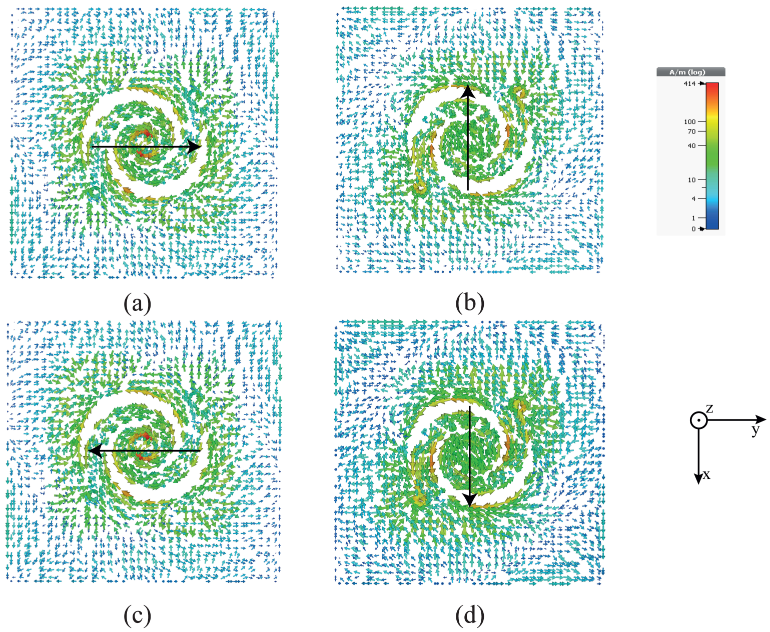

Figure 3.3: Surface current distributions on the proposed antenna at different phases at 35.75 GHz.

32 GHz. It is worth noting that TE_{120} and TE_{210} are degenerated modes on the square cavity and can be excited simultaneously with the same cut-off frequency. However, the transverse slot in the middle of the cavity does not couple to the TE_{210} mode. The electric field distribution in the SIC is demonstrated in Fig. 3.2.

To illustrate the radiation performance of the proposed slot spiral antenna, the simulated surface current distributions on the radiating aperture at different phases of 0° ,90° ,180° and 270° are plotted in Fig. 3.3. The black arrow represents the direction of the major surface current at different phases. As can be seen from this figure, for any two successive 90° phase intervals, the surface current vectors are orthogonal and their amplitudes are almost equal, which enables the CP radiation of the presented antenna.

3.2.3 Printed Ridge Gap Waveguide

The feeding line is implemented by PRGW technology. PRGW structure consists of two parallel plates with a microstrip line in between. The lower layer contains so-called mushrooms to represent the behavior of artificial magnetic conductor (AMC). Having two parallel PEC-AMC plates with a distance less than $\lambda/4$ provides a parallel-plate stopband. Therefore, the signal is travelling in the airgap between the microstrip and the upper PCB. Generally, there are two types of PRGW: (i) inverted printed gap waveguide [19] (ii) suspended printed gap waveguide [82]. For the first one, the microstrip line and AMC layer are in the same layer and the microstrip line is grounded by metalized vias, whereas for the second one, the microstrip line is on the upper layer of the AMC Layer. Having a microstrip line on a separate layer gives more freedom to adjust the position of the microstrip line, which is very important in the large arrays. The suspended printed gap waveguide has been selected for the implementation of the feeding network. The mushroom unitcell is designed based on the design guidelines of the PRGW reported in [82]. Fig. 3.4, Fig. 3.5 and Fig. 3.6 show the configuration of the circular mushroom unit cell, PRGW structure, and the corresponding dispersion diagrams, respectively.

The dispersion diagram is calculated by the Eigenmode solver of CST studio. The dimension of metal circle patches and metalized vias are chosen to obtain the bandstop of 26-51.4 GHz. The band stop covers the operational bandwidth of the proposed antenna with almost equal margins from both sides. As can be seen from Fig. 3.6, by introducing a microstrip line, the band stop diminish to 26-51.4 GHz and the propagating Quasi TEM mode appears in the band stop frequency range. It should be pointed out that due to the finite periodicity of PRGW structure in the transverse direction, several waveguide modes appear below the bandgap [75].

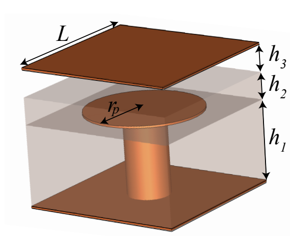

(a)

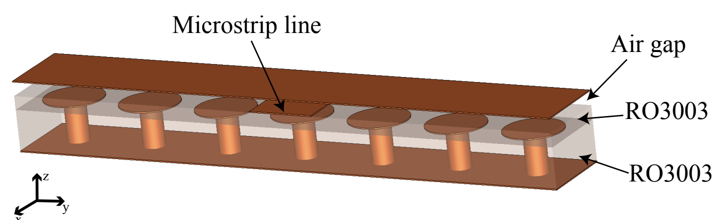

(b)

Figure 3.4: (a) Circle mushroom unit cell (L=1.5mm, $\mathbf{r_p}$=0.55mm, $\mathbf{h_1}$=0.76mm, $\mathbf{h_2} = \mathbf{h_3}$=0.254mm,) (b) PRGW section.

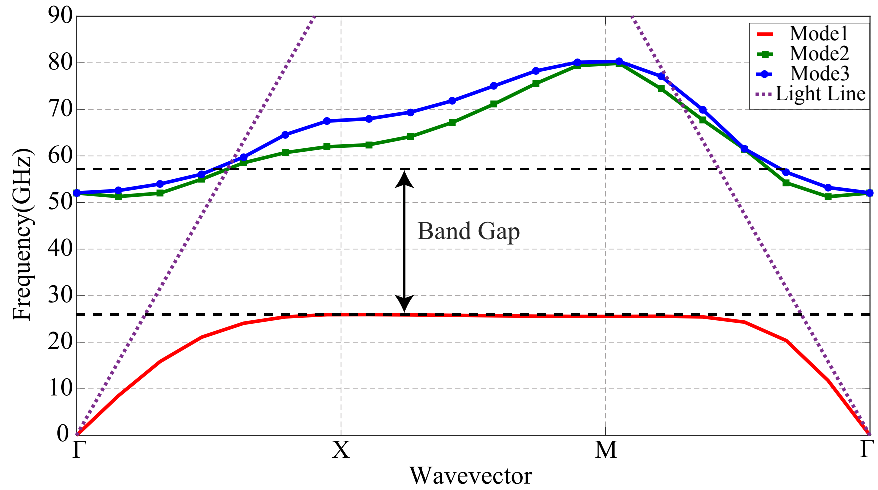

Figure 3.5: Dispersion diagram of the mushroom unit cell.

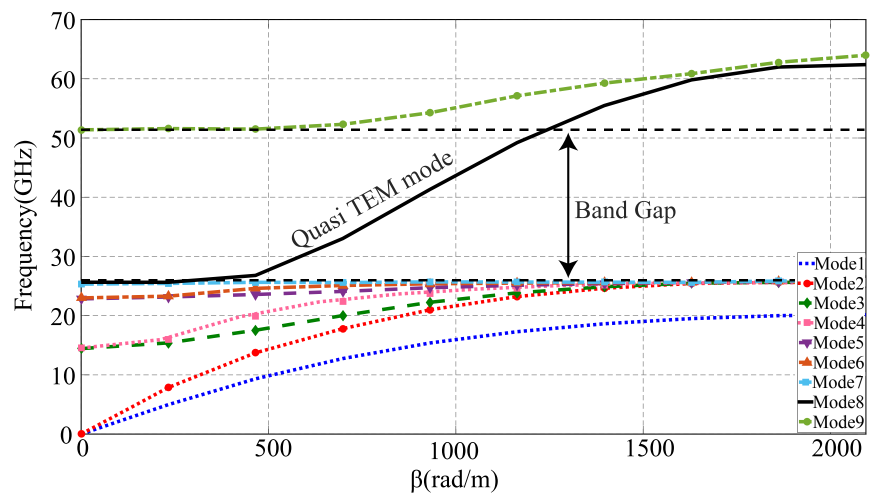

Figure 3.6: Dispersion diagram of the PRGW section.

3.2.4 Single Element Performance

The simulated results for |S11|, AR, and gain are depicted in Fig. 3.7 and Fig. 3.8, respectively. It is seen that; the proposed single element has -10 dB wide impedance bandwidth of 15.44% (34.45 GHz-40.21 GHz) and 3 dB AR bandwidth of 1.76% (35.42 GHz-36.05 GHz), which will be explained as follows. For the conventional slot spiral antenna that the excitation is applied to one end of the arms, the current on each arm is obtained by $I(l) = I_0 e^{(-jbl)}$ (ignoring the mutual coupling between the spiral arms and the reflected current from the arms ending) where I_0 is the initial current at the excitation point, and l represents the arm's length from the excitation point [86].

Here, instead of exciting slot spiral arms from one end, a backed SIC which supports TE_{120} mode is used for the excitation. TE_{120} mode splits the SIC into two halves in which the electric field distribution has the same amplitude and 180° phase difference (Fig. 3.2). Since the slot spiral arms are located in both halves of the SIC, the current phase on each arm is adversely affected by the backed-cavity surface currents. Therefore, the active regions of most frequencies are disturbed, and the CP performance deteriorates. It should be noted that since the sequential feeding plays a

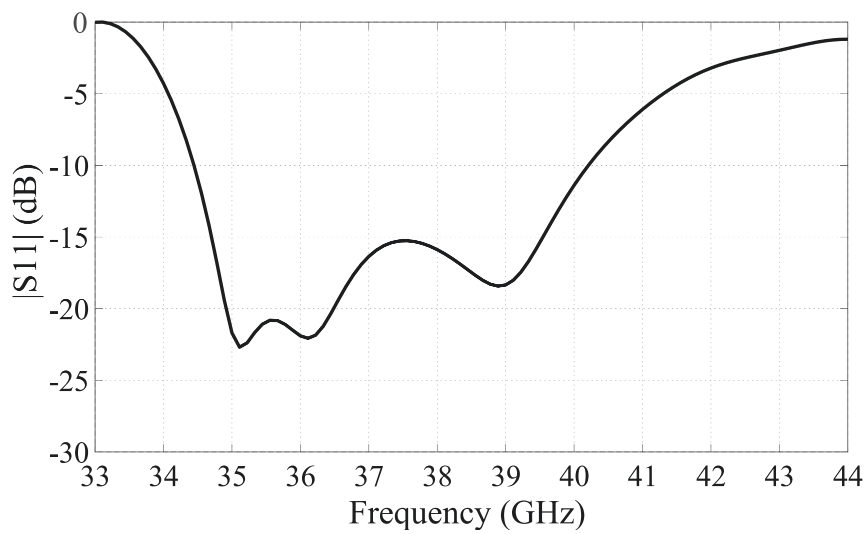

Figure 3.7: Simulated reflection coefficient of the proposed single antenna.

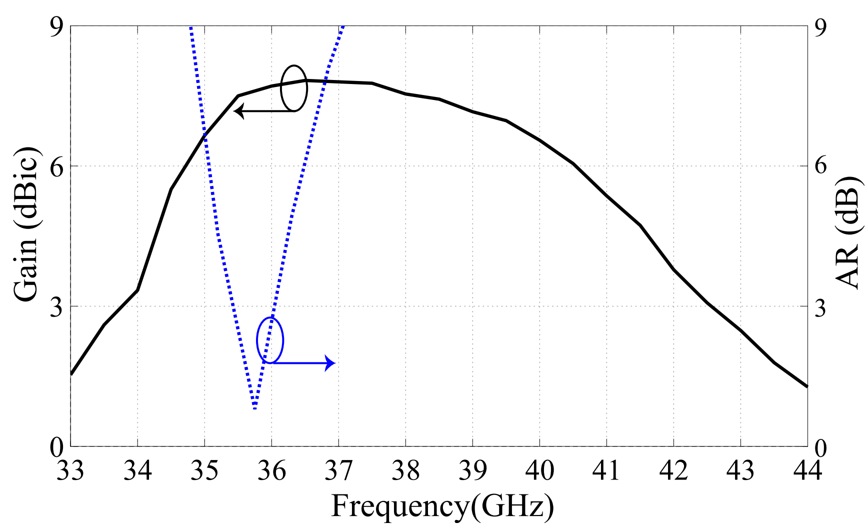

Figure 3.8: Simulated AR and Gain of the proposed single antenna.

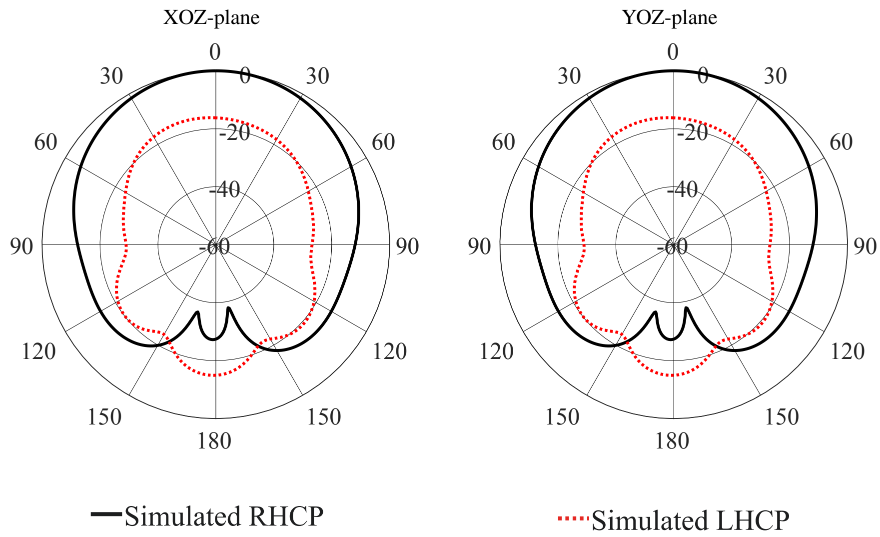

Figure 3.9: Simulated 2-D radiation pattern of the proposed single element in xoz and yoz planes at 35.75 GHz.

more critical role in achieving wide AR bandwidth than the antenna element, antennas with narrow AR bandwidth are commonly used in the sequentially rotated arrays.

The peak RHCP gain of the proposed single element is 7.9 dBic at the boresight direction. The simulated RHCP and LHCP radiation patterns in xoz- and yoz-planes at 35.75 GHz are demonstrated in Fig. 3.9. As can be seen from this figure, the pattern is almost symmetrical in both xoz and yoz planes.

3.2.5 Printed Ridge Gap Waveguide to Microstrip Line Transition

A transition from PRGW to a standard 50Ω microstrip line is used to enable the measurement of the proposed antenna through an end-launch connector [69, 88]. The designed transition is shown in Fig. 3.10. The thickness of the substrate for the microstrip line has to be equal to the airgap thickness, and it acts as a spacer as well. The simulated S-parameter of the designed transition is shown in Fig. 3.11. The designed transition has a good impedance matching level ($S_{11} \leq -14.4dB$) and low insertion loss ($S_{12} \geq -0.33\ dB$) within the whole operating frequency bandwidth.

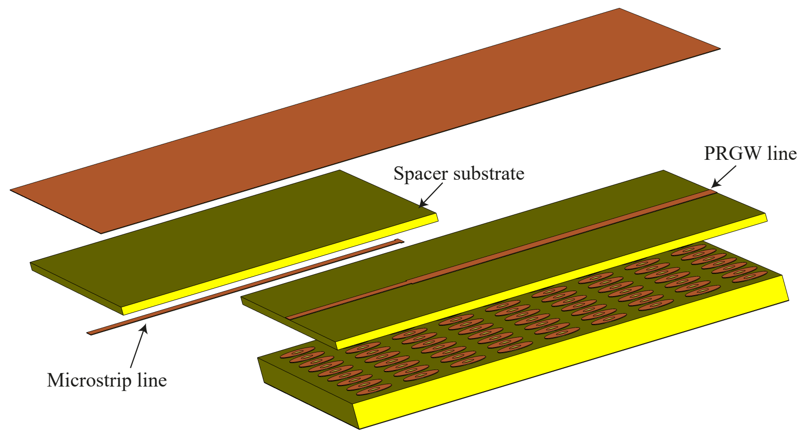

(a)

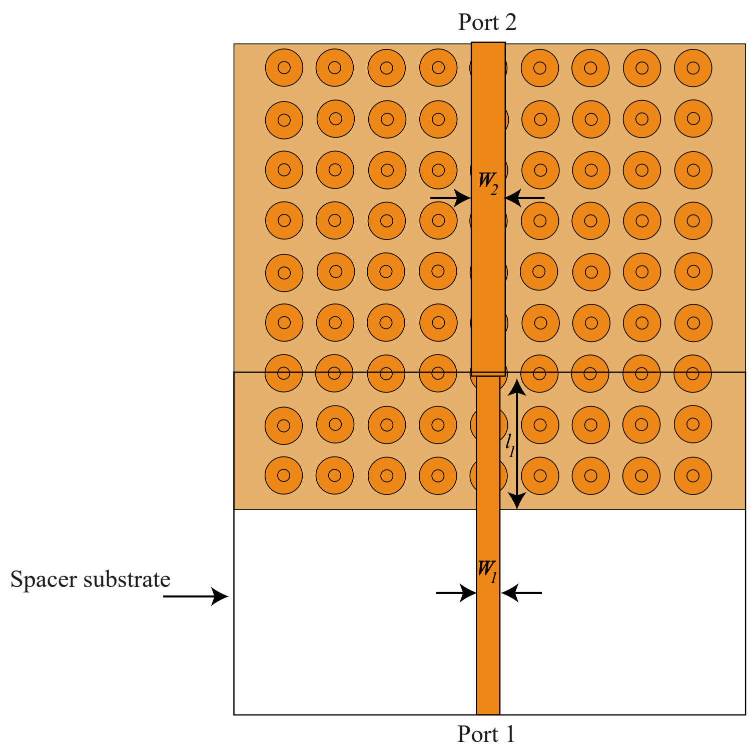

(b)

Figure 3.10: PRGW to 50Ω Microstrip line transition, (a) 3D geometry, (b) Top view ($W_1 = 0.7mm, W_2 = 1mm, l_1 = 3.9mm$).

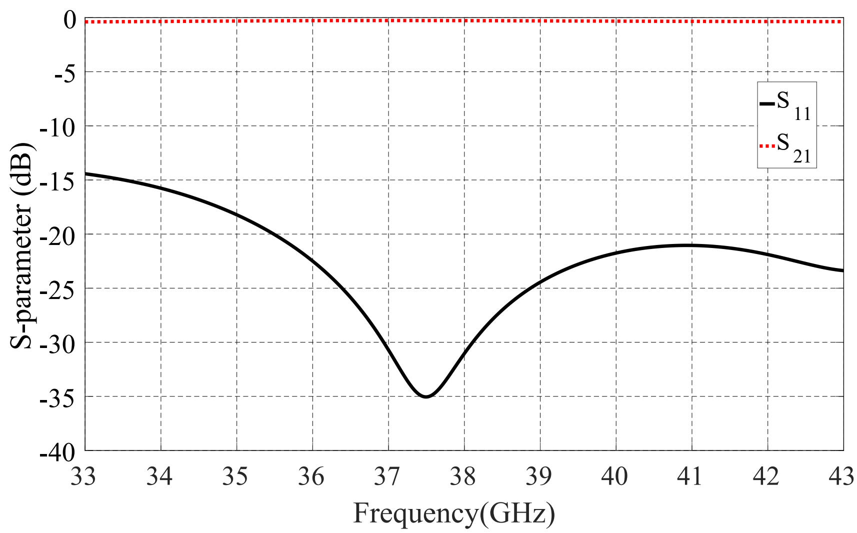

Figure 3.11: Simulated S-parameters of PRGW to 50Ω Microstrip line transition.

3.3 Circularly Polarized Antenna Array

3.3.1 2×2 Sequential Feeding Network

The configuration of the 2×2 antenna array is shown in Fig. 3.12 and Fig. 3.13. In order to get the desired radiation performance of the antenna array, the dimensions of the antenna element in the array configuration have been changed slightly. Element spacing in an array configuration is equal to the cavity width and it is around $0.81\lambda_0$, which is sufficient to avoid grating lobes. The physical aperture size, excluding the surrounding margin, is 12.8×12.8 mm^2(1.62×1.62 λ_0^2).

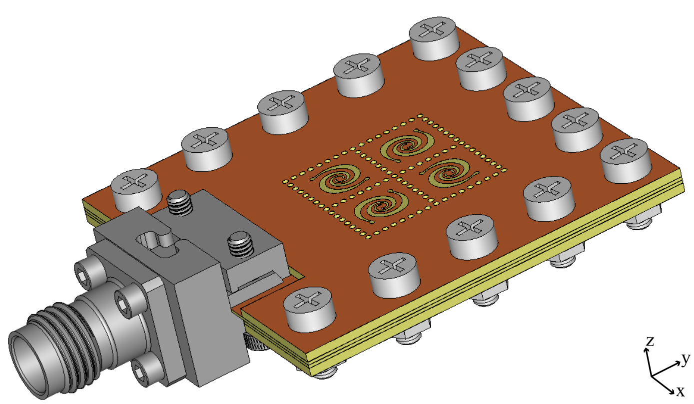

Figure 3.12: 3D view of the 2×2 antenna array with the end launch connector.

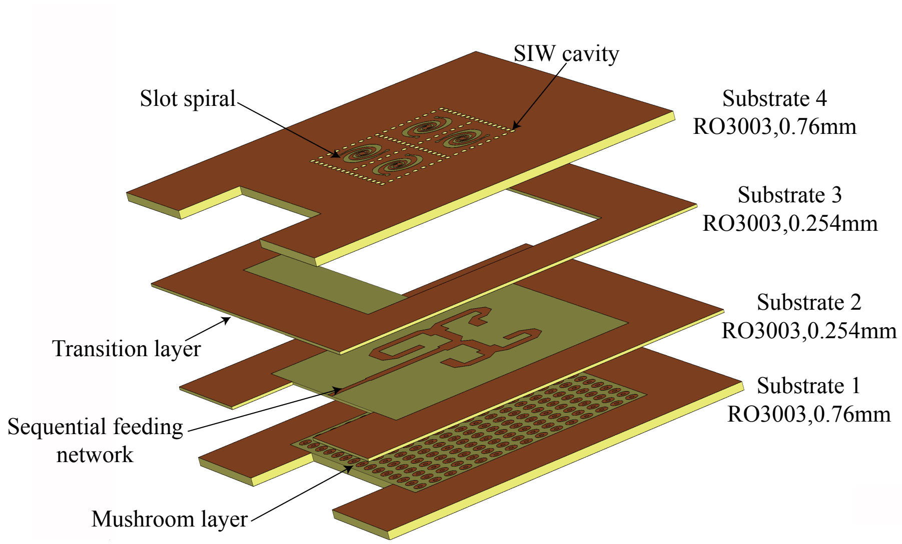

Figure 3.13: Configuration of the proposed 2×2 antenna array.

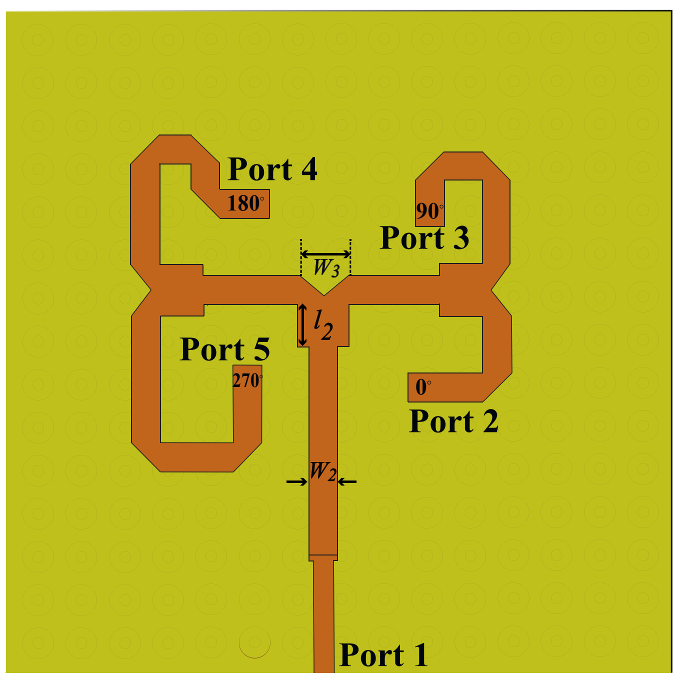

Figure 3.14: Sequential feeding network implemented by PRGW.

The geometry of 2×2 sequential feeding implemented by PRGW technology is shown in Fig. 3.14, where $\mathrm{W_1 = 0.7mm, W_2 = 1mm, W_3 = 1.8mm, l_1 = 3.8mm}$, and $\mathrm{l_2 = 1.5mm}$. The length difference between two successive output ports is a quarter guided wavelength ($\lambda_g/4$) to create 90° phase delay. Since the single element is RHCP, the 90° phase augment between output ports in the sequential feeding network is supposed to be in an anti-clockwise direction. The simulated S-parameters amplitudes and phase difference between output ports are shown in Fig.3.15. The feeding network has 33.75% impedance bandwidth of -20 dB with low insertion loss. The maximum phase deviation of sequential output ports is 26° over the entire bandwidth.

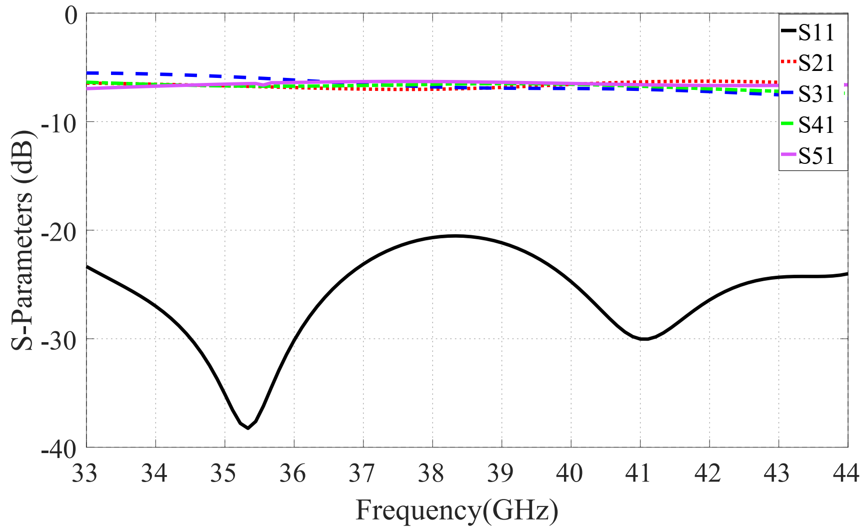

(a)

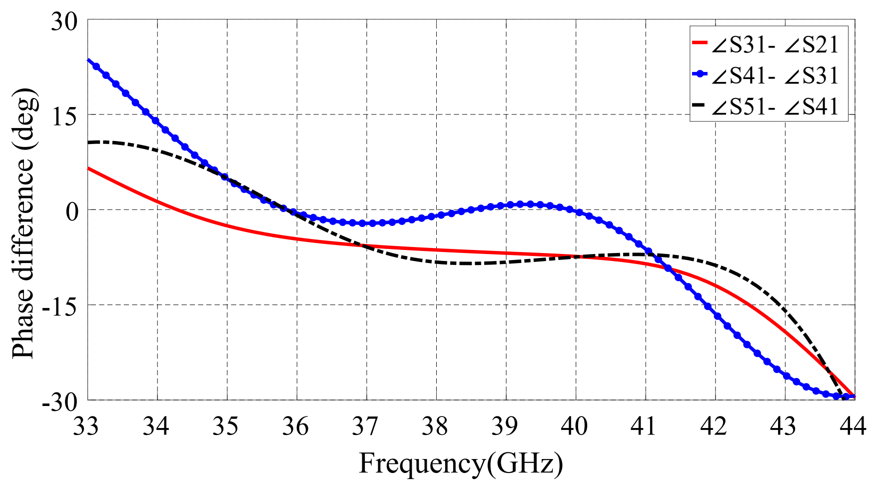

(b)

Figure 3.15: Simulated Results of the designed sequential feeding network, (a) S-parameters, (b) phase error between output ports.

Theoretical gain increase of the 2×2 sequentially rotated antenna array can be calculated using [89]:

$$G_{array} = G_{element} + 20log(1 + \frac{2A_e}{1 + A_e^2} cos\theta_e) \tag{3.5}$$

Where A_e is the amplitude error and θ_e represents the phase error. For the ideal sequential feed network, which provides the equal amplitude and quadrature phase shift for each antenna elements (i.e. A_e(dB)=0 and θ_e(degree)=0), the gain of 2×2 sequentially rotated antenna array increases by 6 dB compared to the gain of a single element.

3.3.2 Effect of Cavity on Array Performance

The backed cavity not only provides planar excitation for the spiral arms but also significantly suppresses the mutual coupling between antenna elements in an array environment. Therefore, it improves antenna performance in terms of cross-polarization, AR, and directivity. Fig.3.16 compares the effect of the cavity on AR of the $2\times$ 2 sequentially rotated antenna array. As depicted, the cavity has a noticeable impact on the CP performance of the antenna array.

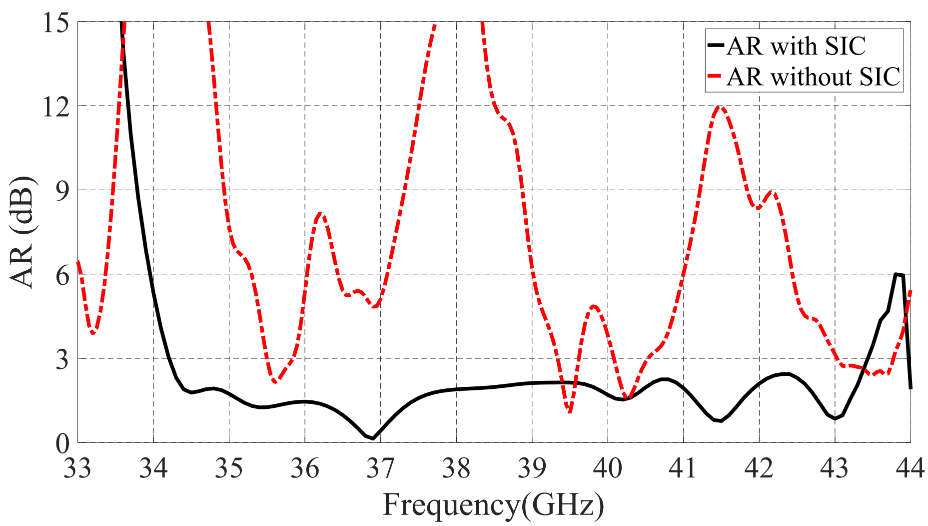

Figure 3.16: Simulated AR of the designed antenna array for the two cases of with and without the cavity.

3.4 Fabrication and Measurement

Four layers of mushroom unit cells, microstrip sequential feeding, spacer and cavity-backed slot spiral antenna array are fabricated independently and then were assembled using plastic screws. Fig. 3.17(a) and Fig. 3.17(b) show the fabricated antenna layers and the assembled antenna, respectively. The antenna array is fed through an end-launch 2.4 mm Southwest Microwave connector. The |S11| of the antenna was measured by a mm-wave band N5227A PNA network analyzer.

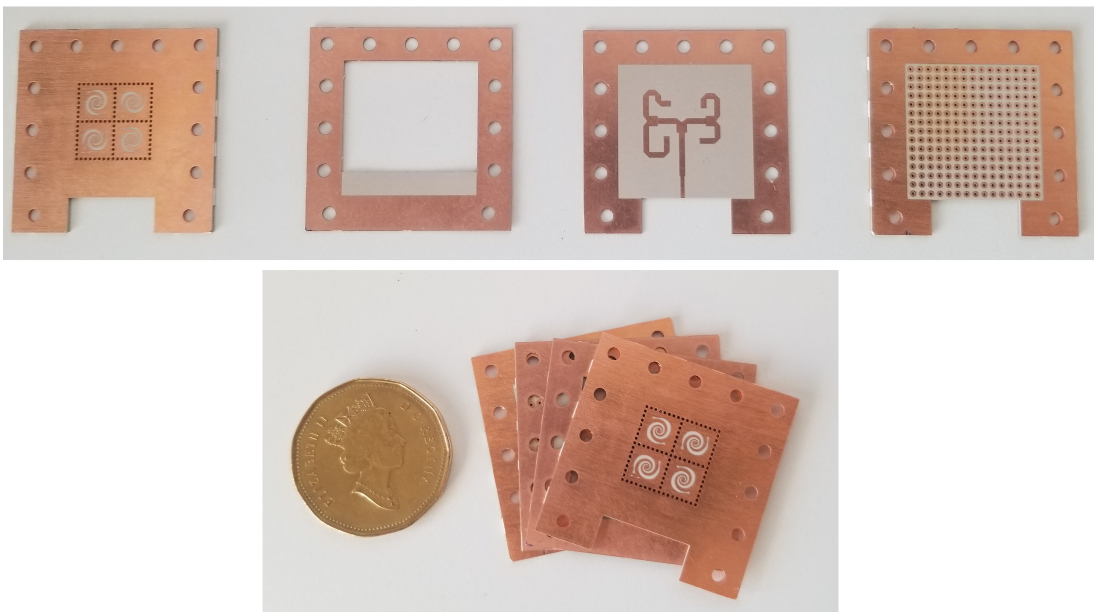

(a)

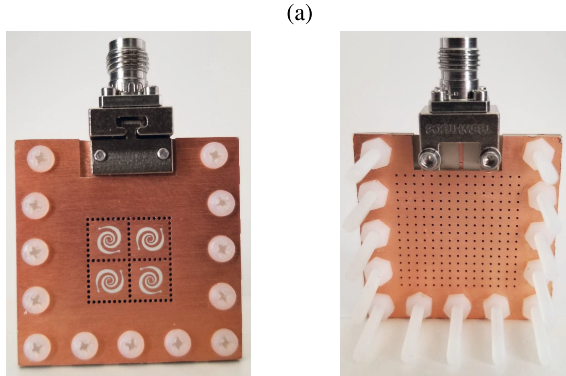

Top view

Rear view

(b)

Figure 3.17: (a) Fabricated proposed antenna arrays before assembly, (b) Fabricated proposed antenna array after assembly.

3.4.1 Simulation and Measurement Results

The simulated and measured reflection coefficient is given in Fig. 3.18. The simulated and measured |S11| (under -10 dB) bandwidth of the antenna is about 24.47% from 33.74 GHz to 43.15 GHz and 23.7% from 33.66 GHz to 42.71 GHz, respectively. The measured and simulated AR and RHCP gain of the antenna array at the boresight direction are plotted in Fig. 3.19. The simulated and measured 3 dB AR bandwidth is about 23.42% from 34.3 GHz to 43.4 GHz, and 22.5% from 34.5 GHz to 43.25 GHz, respectively. Besides, a measured peak gain of up to 12.3 dBic at 36 GHz is achieved. The simulated and measured fractional 3 dB gain bandwidth is 23.69% from 33.97 GHz to 43.1 GHz and 20.33% from 34.25 GHz to 42 GHz, respectively.

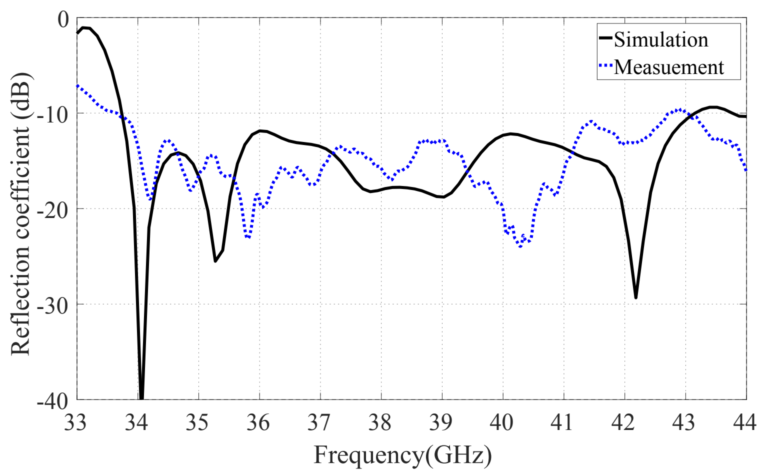

Figure 3.18: Simulated and measured reflection coefficient of the proposed antenna array.

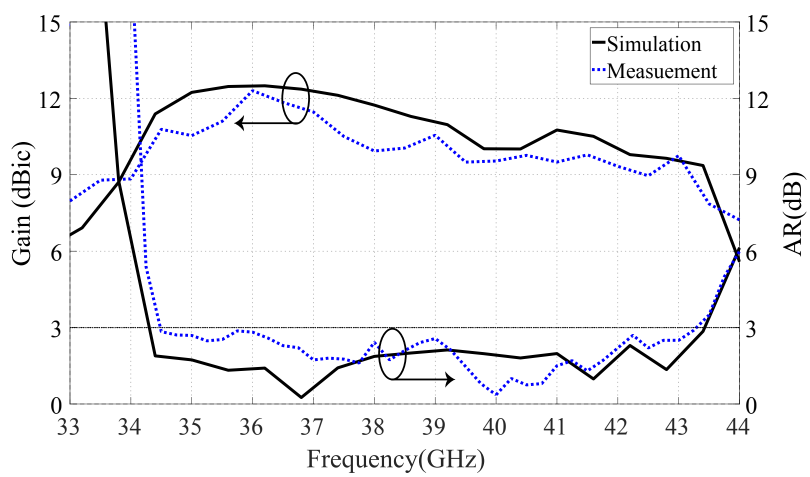

Figure 3.19: Simulated and measured gain and AR of the proposed antenna array.

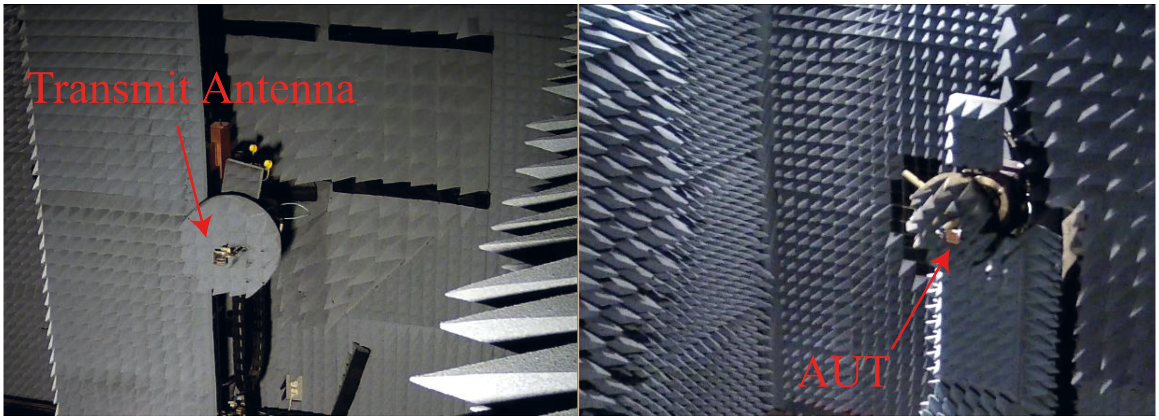

Figure 3.20: Radiation pattern measurement setup.

The radiation performance of the antenna array was measured by employing the far-field measurement setup in the anechoic chamber as exhibited in Fig. 3.20. The measured and simulated radiation 2-D patterns of the antenna array on both xoz and yoz planes at frequencies of 35 GHz, 37 GHz and 39 GHz are illustrated in Fig. 3.21. Relatively good agreement is obtained between the simulated and measured radiation patterns. The measurement results reveal that the maximum level of cross polarization (i.e., LHCP) is -15.5 dB at the boresight direction.

The designed array has the advantage of high radiation efficiency. The simulated radiation efficiency is better than 88% for the whole frequency band. This merit is mainly due to the lower transmission line loss and surface wave loss that PRGW possesses compared with the microstrip lines.

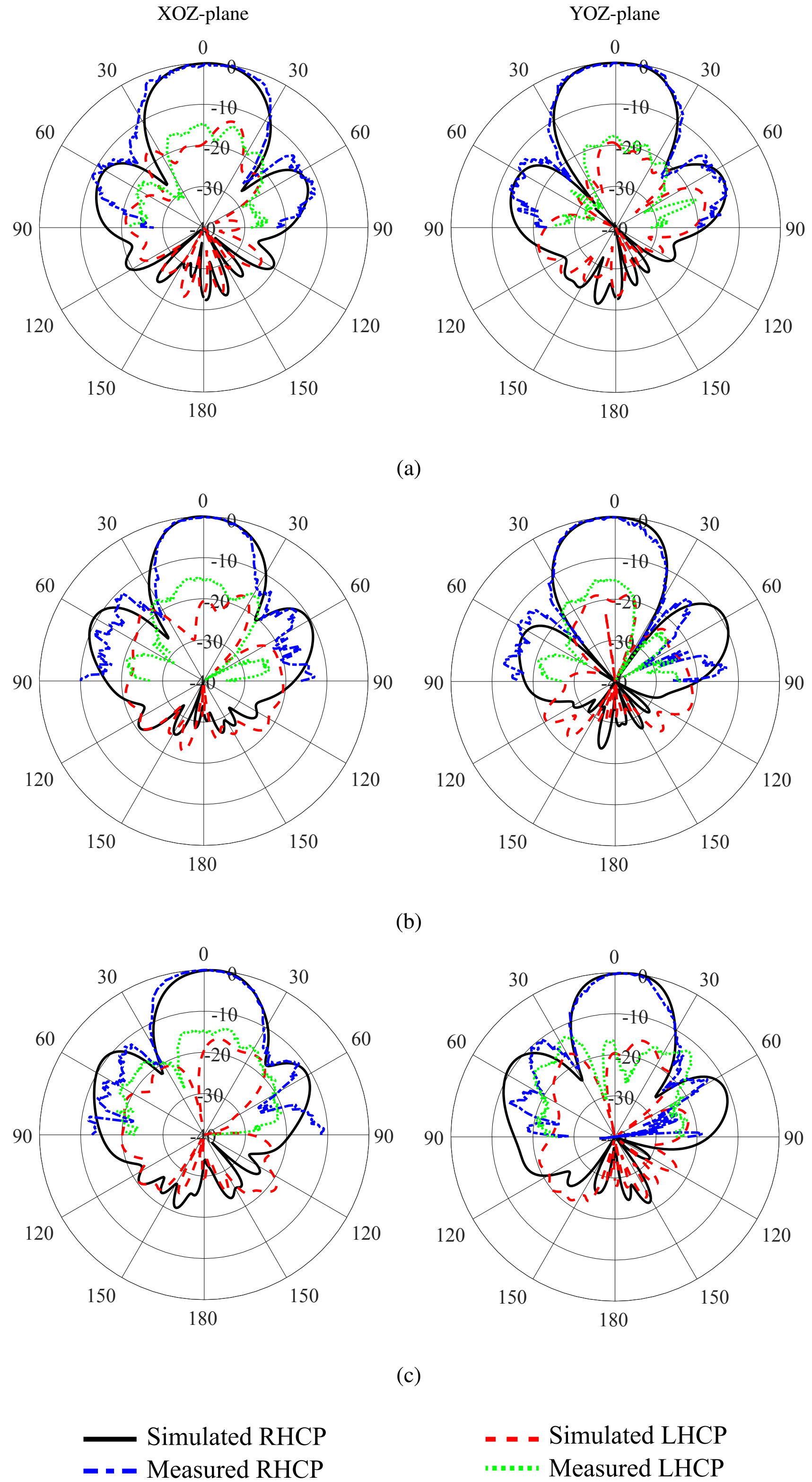

Figure 3.21: Simulated and measured 2-D radiation pattern of the proposed antenna array at (a) 35 GHz, (b) 37 GHz, and (c) 39 GHz.

3.4.2 Comparison and Discussion

Table 3.2 compares the performance of the proposed antenna array with some other CP mm-wave 2×2 in the literature. To provide a fair comparison with our work, all of the listed antenna arrays in Table 3.2 are fed using the 2×2 sequential rotation feeding technique. Since the radiation efficiency is not available in any of the papers listed in Table 3.2, the total efficiency (aperture efficiency × radiation efficiency) is calculated using the antenna's aperture size, maximum gain and its corresponding frequency [90]. The total efficiency of the proposed antenna is better compared to other papers except for the antenna in ref [91]. The antenna in [91] owns higher aperture efficiency due to the usage of a series-type feeding network, which is more compact compared to the parallel-type feeding network employed in other reported papers in Table 4.3. However, the antenna array in [91] suffers from relatively narrow 3 dB AR bandwidth. The radiation efficiency and the aperture size of the antenna array in [92] and our work are close. But the proposed work owns slightly higher gain and AR bandwidth and less number of layers, which can reduce the fabrication complexity.

Table 3.2: Comparison between the proposed antenna array and other reported 2×2 antenna array at mm-wave band

	Ref. [91]	Ref. [64]	Ref.[93]	Ref. [92]	Ref. [94]	This work
Size (λ_0^2)	1.55×1.55	3.6×3.6	3×3	2.86×2.94	4.5×4.5	2.9×2.9
Freq (GHz)	29	28	60	26	45.5	38
Element	Patch	Slot	Grid array	Patch	Slot	Slot spiral
Feeding Network	Sequential (microstrip)	Sequential (SIW)	Sequential (LTCC)	Sequential (SIGW)	sequential (SIW)	Sequential (PRGW)
Imp. BW%	15.45	23.3	16.7	25.6	14.72	23.7
AR BW%	5.44	7.7	12.5	19	14.72	22.5
Peak gain (dBi)	13.6	10.8	14.3	11.5	10.5	12.3
Efficiency% ($\epsilon_{ap} \times \epsilon_{rad}$)	74.5	16	31.8	57.3	17.5	57.3

3.5 Summary

A wideband cavity-backed slot spiral antenna at mm-wave band is developed in this paper. A backed SIC provides differential excitation and makes this antenna independent of the complicated balun structures. The single element is employed in the 2×2 sequential rotation feeding configuration. The presented antenna is compatible with PCB fabrication technology, which makes it very low cost. Experimental results agree well with the simulated results, where the measured -10 dB impedance bandwidth, 3 dB AR bandwidth and 3 dB gain bandwidth are 23.7%, 22.5% and 20.33%, respectively. The proposed antenna array achieves the measured peak RHCP gain of 12.3 dBic and high radiation efficiency due to the implementation of the feeding network with PRGW technology.

Chapter 4

Broadband Compact Circularly Polarized Spiral Antenna Array

4.1 Introduction

In chapter 2, a wideband CP slot spiral antenna array was described. In this chapter, to further improve the antenna characteristics, the spiral antenna is chosen as the radiating element.

Spiral antennas possess a planar structure and can be implemented using low-cost printed circuit board (PCB) technology. Therefore, spiral antennas are preferred to helical antennas in terms of the fabrication simplicity. However, there are two main problems in the realization of a spiral antenna at high frequencies, where compactness is a crucial requirement. The main problem with spiral antennas is that they need balun circuits to be excited in a balanced mode [86]. This problem becomes more severe in an antenna array configuration, in which balun circuits add more complexity to the whole structure. Another problem with the spiral antennas is that to fulfill the traveling wave requirements, the currents on spiral arms should have decaying current distribution [87]. This situation happens if the spiral is electrically large enough; otherwise, the reflected currents from the arms ends cause the total currents distribution to be standing waves, which in turn deteriorates the wideband characteristics of the AR and impedance matching [33]. Considering fabrication constraints and the size of spiral antenna with multiple turns, it is hard to keep element spacing in array configuration less than λ_0 (where λ_0 is the free space wavelength) at mm-wave frequencies and avoid the presence of grating lobes. Moreover, conventional approaches such as coating the arm ending with chip resistors [95] or terminating the spiral arms with zigzag sections [96] are not appropriate at mm-Wave frequency bands due to the severe loss at high frequencies and difficulties in fabrication, respectively. These problems hinder the usage of spiral antennas at high frequencies, despite their desirable wideband radiation performance.

Zhu et al. in [84] addressed these problems. To make the spiral antenna independent of balun circuits, spiral arms are differentially fed using two opposing vias located at the two sides of the coupling slot. Besides, to have the CP wave generation from the shorter spiral arms, their lengths are differed by $\lambda/4$ to create a $90°$ phase difference between the surface currents on both arms. However, perturbing the symmetry of the spiral antenna causes beam tilting in the radiation pattern. In this paper, we tried to tackle the problem of the large dimension of the spiral antenna without perturbing the spirals' symmetry.

In this chapter, we propose a wideband and compact CP spiral antenna array fed by the PRGW sequential-rotation feeding structure. The proposed spiral antenna is relatively small and has less than one turn. In order to broaden the AR bandwidth and improve the array CP purity, the proposed antenna element is utilized in the SR arrangement. The designed antenna array has been fabricated, and its performance is validated by measurement. The rest of this chapter is organized as follows; Section 4.2 discusses the design principles of the proposed antenna structure and the PRGW line. Section 4.3 presents the implementation of the antenna array, followed by the design of the PRGW sequential feeding network. The experimental prototyping results and comparison with other similar works are illustrated in Section 4.4. Finally, Section 4.5 presents the conclusion of this Chapter.

4.2 Realization of the Proposed CP Spiral Antenna

4.2.1 Single Radiating Element Design

Fig. 4.1 illustrates the configuration of the proposed structure. It consists of a two-arm symmetrical spiral antenna on top of substrate 1 and two planar patches printed on substrate 2, which form a half-wavelength dipole. Both substrates are Rogers RO6002 with $\epsilon_r = 2.92$, $tan\delta = 0.0012$ and thicknesses of 0.762 mm and 0.528 mm from top to bottom, respectively. Therefore, the spiral

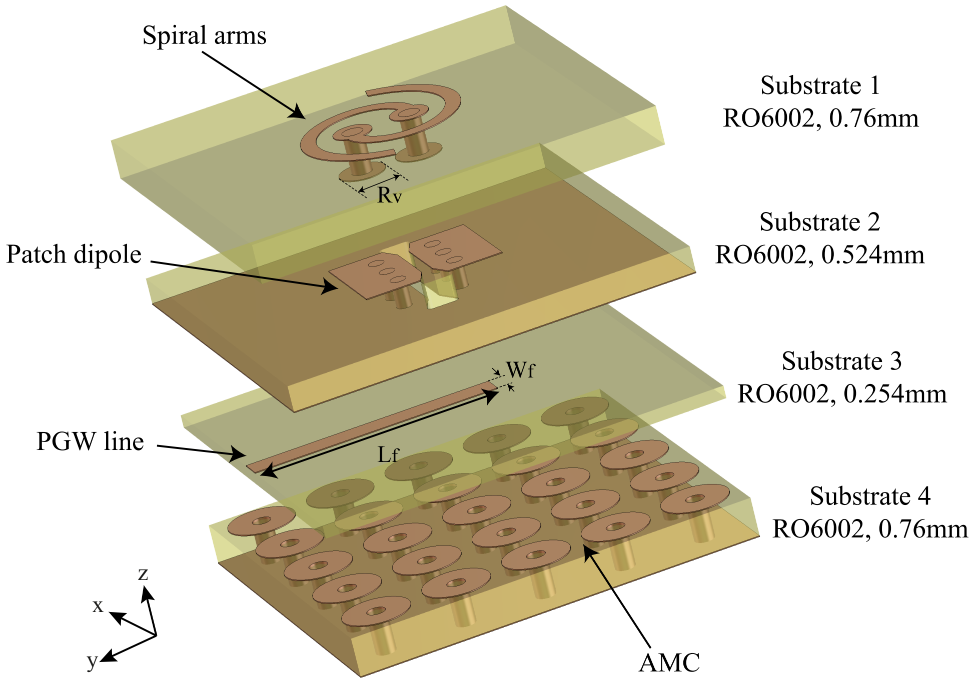

(a)

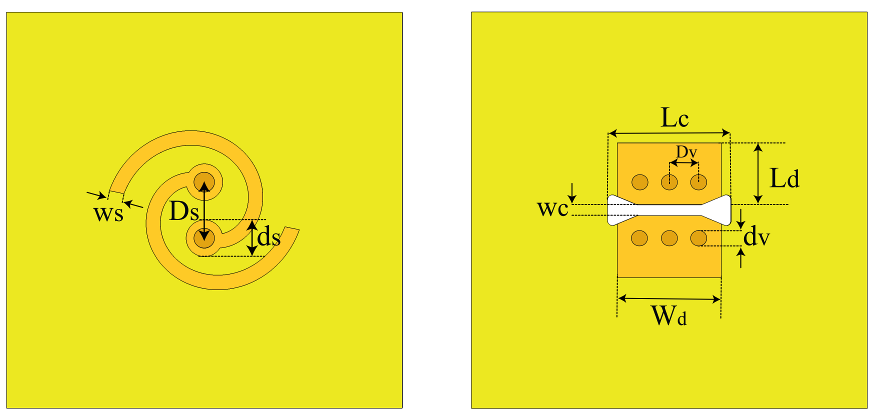

(b)

Figure 4.1: Geometry of the proposed antenna element, (a) Perspective view, (b) Top view.

antenna is located above a conducting ground plane with a height of approximately $\lambda_g/4$ (is the guided wavelength in substrate 2 and 3) to ensure the unidirectional radiation pattern. The spiral arms constructed by the Archimedean spiral function of $r = a\theta + b$ in the polar coordinate system, where a is spiral constant, θ represents the winding angle, and b is the initial radius. Here b can be obtained by $0.5(D_s - w_c)$, where w_c is the width of the coupling slot, and D_s is center to center

Table 4.1: Dimension of the proposed single element (mm)

Parameter	W_f	L_f	W_s	D_s	d_s	L_c	W_c
Value	0.5	4.9	0.3	1.13	0.74	2.5	0.22
Parameter	W_d	L_d	d_v	D_v	R_v	a^*	θ_{end}^{**}
Value	2.1	1.25	0.3	0.6	0.89	0.276	4.51

* The unit is rad/mm.

** The unit is rad.

via distance on the top layer and is determined by fabrication constraints. The second arm of the spiral antenna is composed by rotation of the first arm by π rad. The winding angle of the spiral is increasing from 0 to 4.51 rad, and the spiral number of turns is N=0.83.

The spiral arms are fed differentially by two opposing vias located at both sides of a transverse slot, which is etched on a lower substrate. The length of the coupling slot is $\frac{\lambda_g}{2}$ where λ_g is the guided wavelength at the center frequency of 34 GHz. It is noted that two circular patches surround two vias on the bottom of substrate 1 to ensure good electrical contact between two vias and the patch dipoles on substrate 2.

The PRGW feeding line is employed for the slot coupling. The shape of the slot is chosen to enhance the electromagnetic energy coupling between the slot and the PRGW line. Detailed geometrical dimensions of the proposed structure are summarized in Table 4.1. The presented antenna generates RHCP (Right-hand Circular Polarization) due to the direction of spiral windings and differential phase excitation.

4.2.2 Single Element Operating Principles

To excite a two-arm spiral antenna in the fundamental mode, spiral arms must be excited with the same amplitude and 180° phase difference [86]. In our design, two vias located at the lateral sides of the slots etched on the top layer serves as a balun for the spiral arms. Fig. 4.2 illustrates the sketch of the electric field and electric currents on the cross section of the proposed structure. As it is shown, the electric currents on two vias of the top substrate are out of phase, which provides a differential feed for the spiral arms. The proposed spiral antenna has a relatively small dimension with $\frac{D}{\lambda_0} = 0.41$. The polarization of an electrically small spiral antenna is highly elliptical due to the

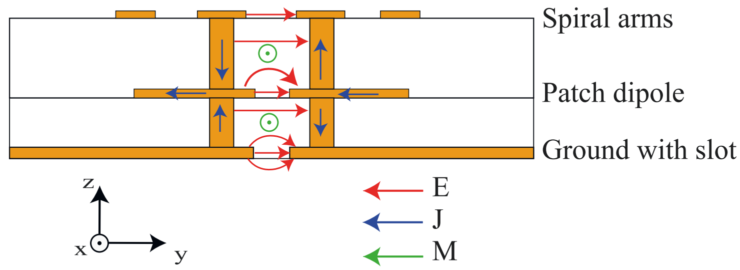

Figure 4.2: Cross section view of the proposed element with sketch of electric field, electric and magnetic currents.

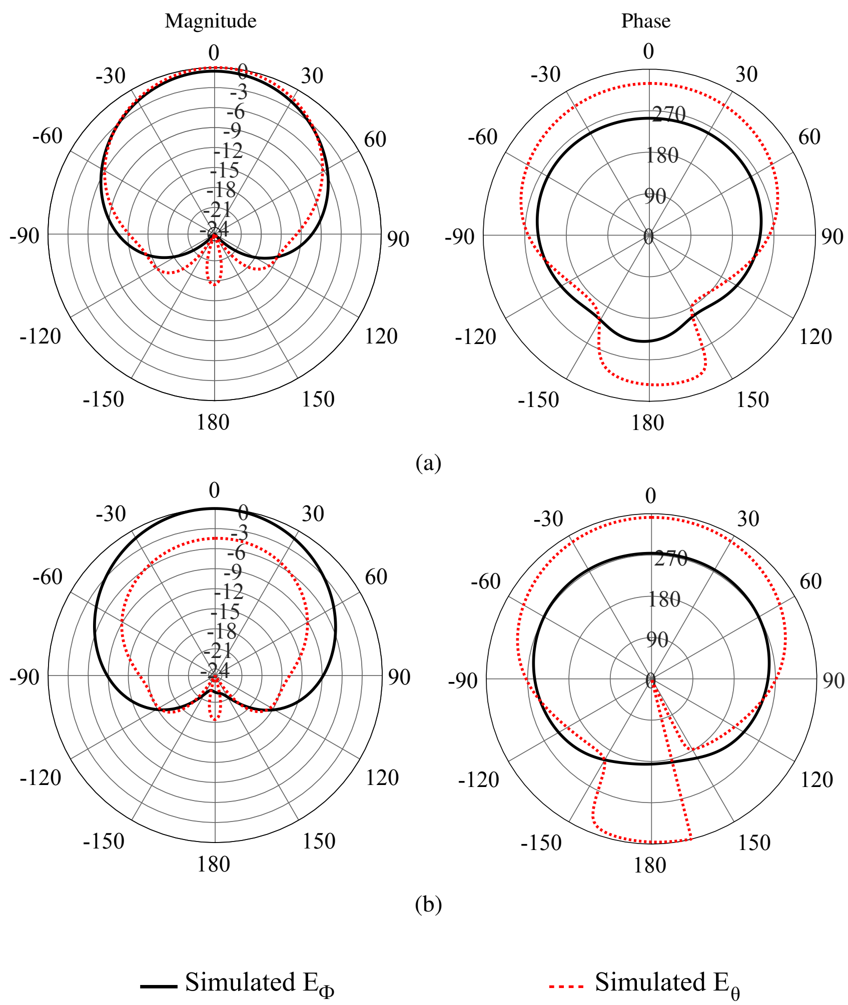

Figure 4.3: Magnitude and phase of E_θ and E_ϕ in the y-z plane at 34 GHz, (a) With patch dipole, (b) Without patch dipole.

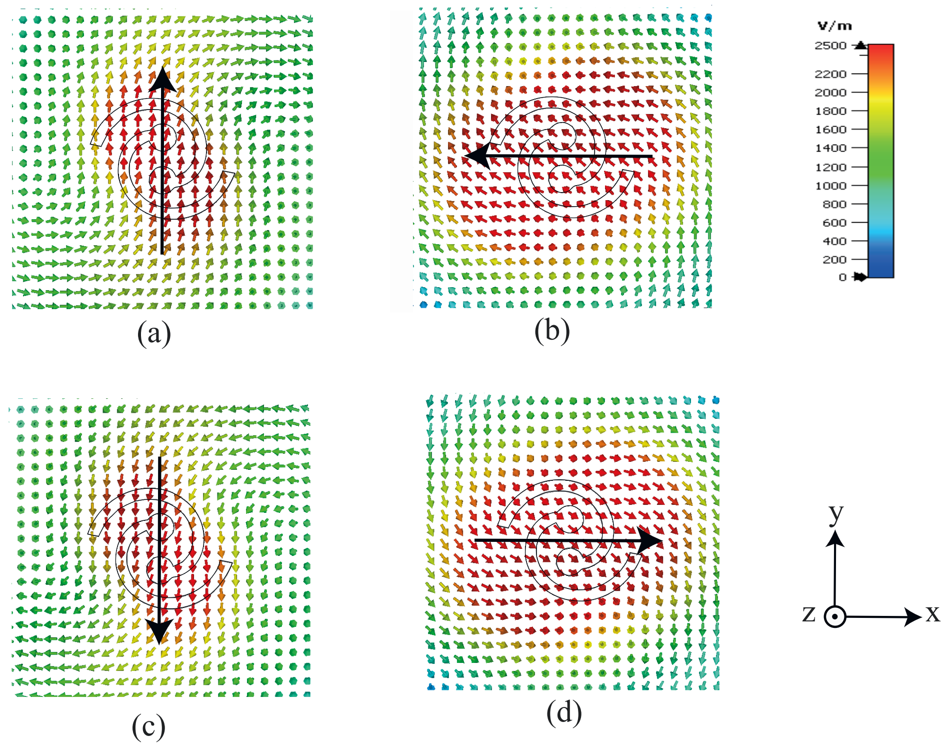

Figure 4.4: E-field distributions on the plane just above the top layer in a period of time at 34 GHz, (a) t = 0, (b) t = T/4, (c) t = T/2, (d) t = 3T/4.

unequal magnitude of orthogonal electric currents at time intervals of t=T/4 (T is one period of time) on the spiral arms. The y-oriented patch dipole is placed under the spiral to reinforce the electric current along the y-direction. To better reveal the effect of the patch dipole on the CP performance, the magnitude and phase of electric field components, E_θ and E_ϕ, in the y-z plane are plotted in Fig. 4.3. It should be noted that to provide a fair comparison, the distance of the spiral antenna from the ground plane is kept unchanged. As can be seen, for the case of without patch dipole $E_\phi > E_\theta$, which results in the elliptically polarized wave. However, adding the y-oriented patch dipole improves the E_θ components while the phase difference between E_θ and E_ϕ has remained almost constant at 90°. It is worth pointing out that the patch dipole is a non-radiating element. In the designed patch dipole, vias act like an inductor, and the gap between two patches acts like a capacitor. The resulting LC circuit improves the antenna performance in terms of AR.

To clarify the CP generation of the proposed structure, the simulated electric field distribution on a plane just above the top layer at t=0, T/4, T/2 and 3T/4 are plotted in Fig. 4.4. The black arrow represents the dominant direction of electric field components. Based on the orientation of the electric field, the co-polar vector is $E_{Co} = E_y - jE_x$, which confirms RHCP generation according to [[23], equation(2.21)].

4.2.3 Printed Ridge Gap Waveguide

The feedline is implemented using PRGW technology. The PRGW supports the propagation of the quasi-TEM wave in the air gap between the upper plate of the PRGW structure and the microstrip line, which is placed above the artificial magnetic conductor (AMC). The AMC surface is realized by 2D periodic EBG unit cells. However, the EBG structure can create the AMC boundary conditions over a limited frequency range, called stopband. Within the stopband, the electromagnetic wave follows the microstrip line, and propagation of any PEC–AMC parallel-plate modes is suppressed if the height of the air gap is less than a quarter of a free space wavelength [68]. The simulated dispersion diagram and the geometry of the unit cell are indicated in Fig. 4.5. The dispersion diagram, which shows the unit cell's stopband, is simulated through the Eigenmode solver of CST. The mushroom EBG unit cell is designed to cover the bandgap of 22.5-50 GHz based on the design guidelines of gap waveguides discussed in [69, 75]. RO6002 substrate with a loss tangent of 0.0009 and dielectric constant of 2.94 and thickness of 0.76 mm and 0.25 mm are used to print

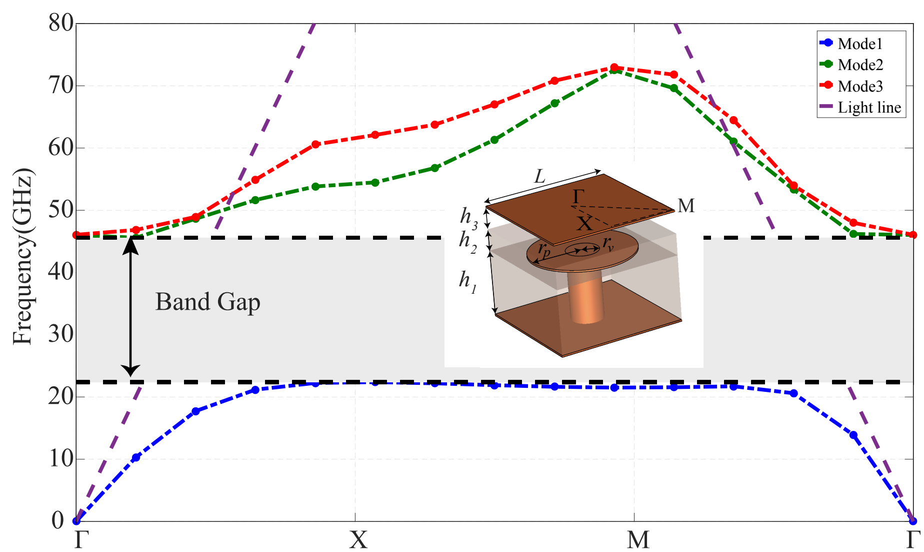

Figure 4.5: Dispersion diagram of the designed unitcell (with $\mathbf{L}$=1.6mm, $\mathbf{r_p}$=0.65mm, $\mathbf{r_v}$=0.4 mm, $\mathbf{h_1}$=0.76mm, $\mathbf{h_2}$=$\mathbf{h_3}$=0.254 mm).

mushroom unit cell and metallic microstrip line. Fig. 4.6 (a) depicted the PRGW section geometry, which consists of 3 rows of the unit cell on lateral sides of the printed microstrip line. By introducing a metallic microstrip between the PEC-AMC plates, a quasi-TEM mode can propagate within the bandgap frequency band, as shown in Fig. 4.6 (b). As can be seen from this figure, the bandgap of the PRGW structure is from 22.9-46.3 GHz. It is noted that the PRGW bandgap frequency range must cover the operational bandwidth of the designed antenna with margins.

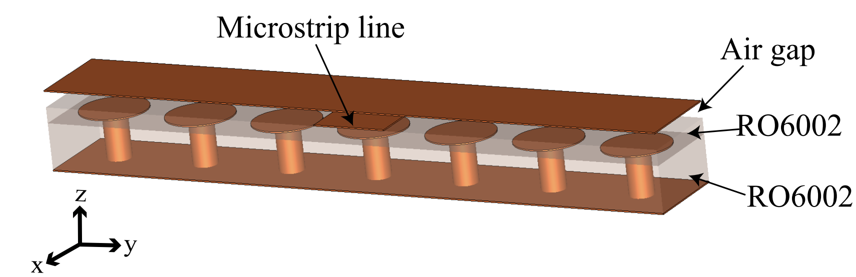

(a)

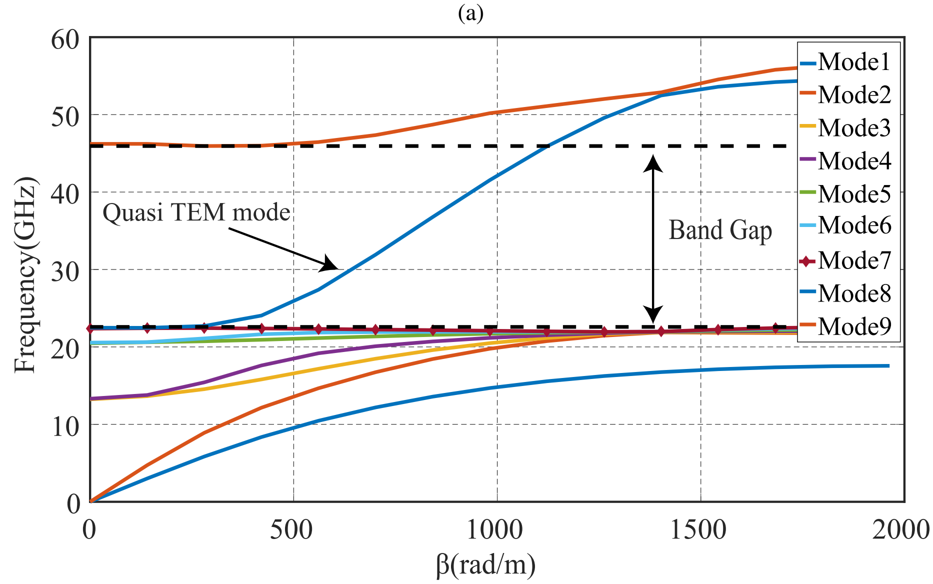

(b)

Figure 4.6: (a) PRGW section, (b) Dispersion diagram of PRGW section.

Generally, the PRGW line's width is larger than the microstrip line, which leads to a smaller conductive loss. Here, the width of PRGW is chosen to provide the impedance of 75Ω to have a better matching for the high input impedance of the spiral antenna.

4.2.4 Performance

The simulated reflection coefficient, AR, and gain of the proposed antenna are shown in Fig. 4.7 and Fig. 4.8, respectively. The presented single element has -15 dB impedance bandwidth of 37.2% ranging from 28.13 GHz to 41 GHz, 3-dB AR bandwidth of 23.2% ranging from 30.6 GHz to 38.62 GHz and maximum RHCP gain of 7.2 dBic in the broadside direction. Fig. 4.9 presents the simulated normalized radiation pattern of the proposed structure in xoz- and yoz-planes at 34 GHz. It can be observed from Fig. 4.9 that the proposed CP element exhibits low cross-polarization of -18.5 dB in the broadside direction.

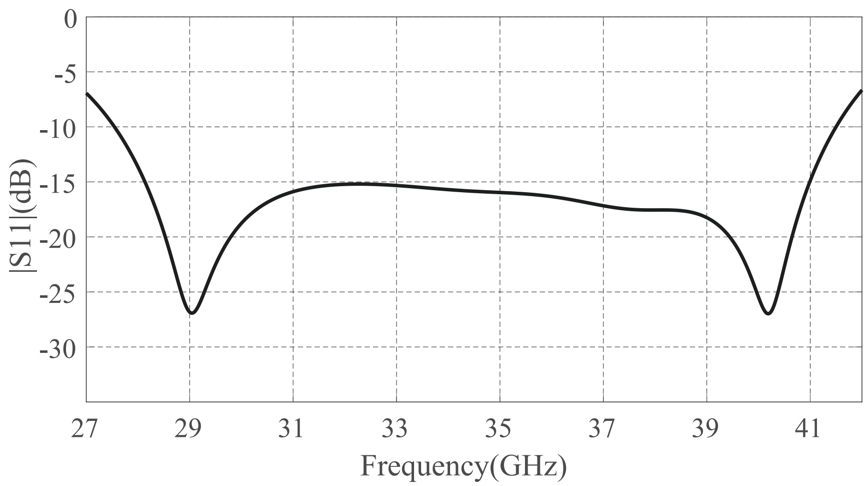

Figure 4.7: Simulated reflection coefficient of the proposed single antenna.

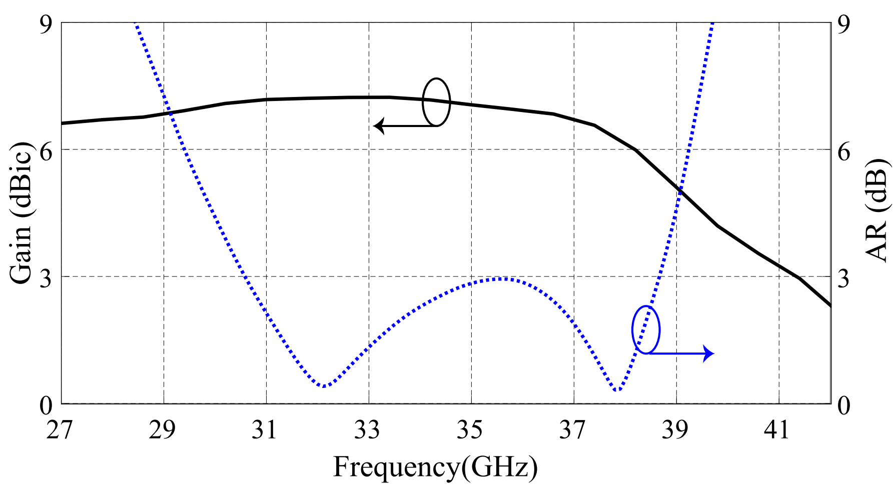

Figure 4.8: Simulated AR and RHCP Gain of the proposed single antenna.

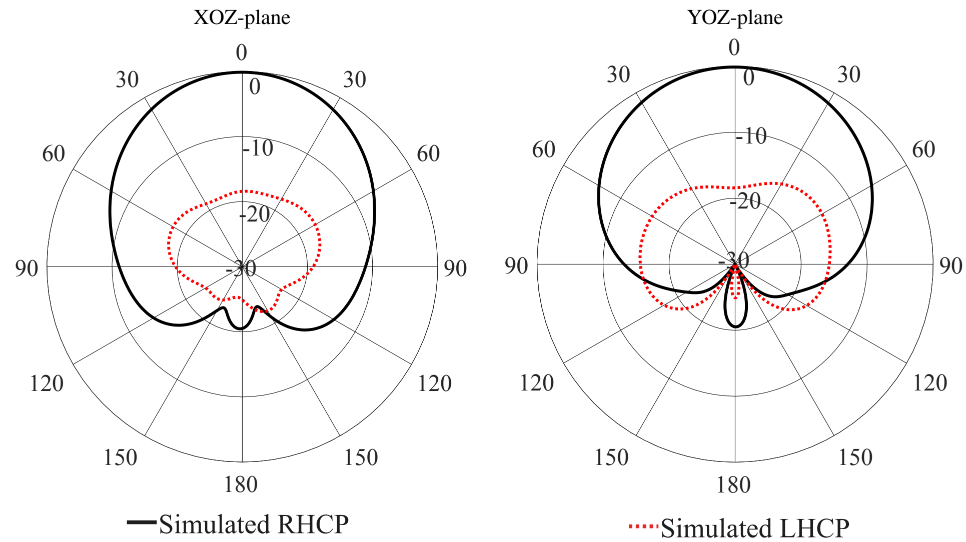

Figure 4.9: Simulated normalized radiation pattern of proposed single antenna at 34 GHz in xoz and yoz planes.

4.3 Circularly Polarized Antenna Array

4.3.1 2×2 array

The geometry of the 2×2 CP spiral antenna array is shown in Fig. 4.10. It consists of 3 main parts: (1) sequential feeding network on the bottom layer, (2) patch dipoles on the middle layer (3) spiral antenna on the top layer. The spacing between antenna elements is 0.85 λ_0 (λ_0 corresponds to the highest frequency in the operating band) to avoid the generation of grating lobes. The sequential feeding network is realized using PRGW and will be further explained in the next part. A transition from the PRGW line to the MS line is designed for the sake of measurement.

4.3.2 Feeding Network

The SR feed technique is a well-known method to broaden the AR bandwidth in which antenna elements undergo both progressive phase difference and physical rotation. This method can be applied to both LP and CP radiating elements [44, 60, 93]. However, CP radiating element fed by the SR feed technique exhibits higher CP purity and wider AR bandwidth. It is worth mentioning that the employment of a corporate feed network that applies an equal phase to each antenna element in an array configuration usually deteriorates the CP performance of the whole antenna. In [90],

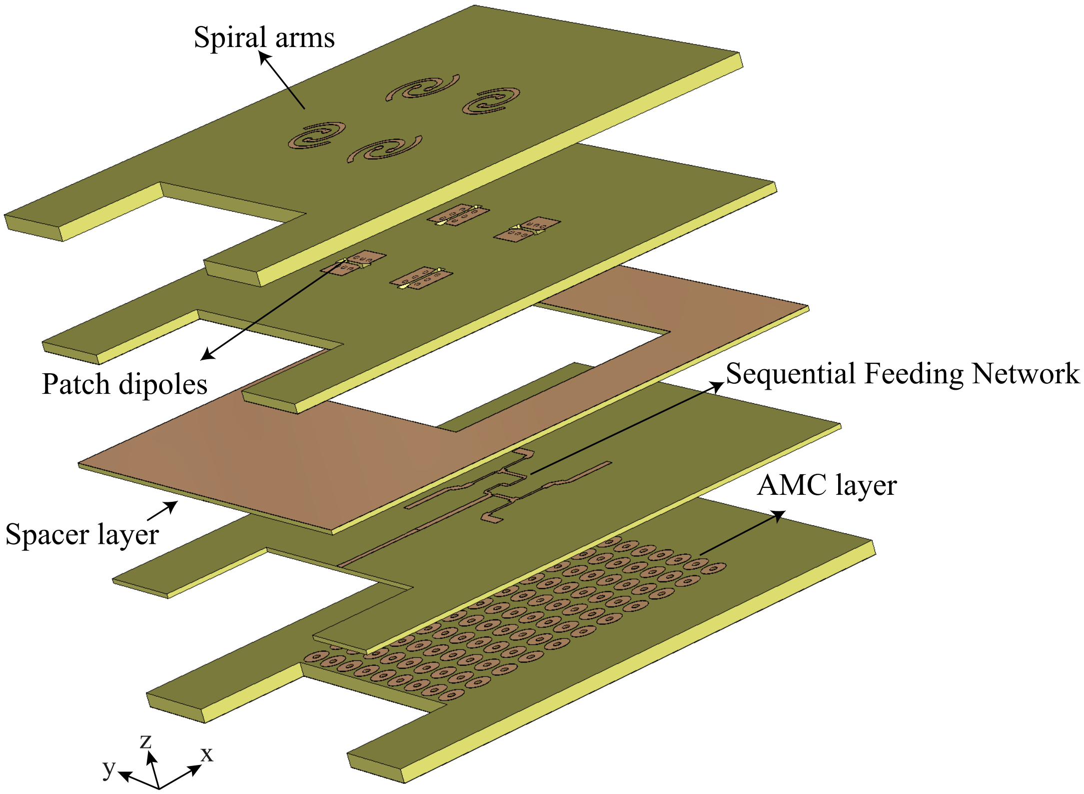

Figure 4.10: Proposed antenna array structure.

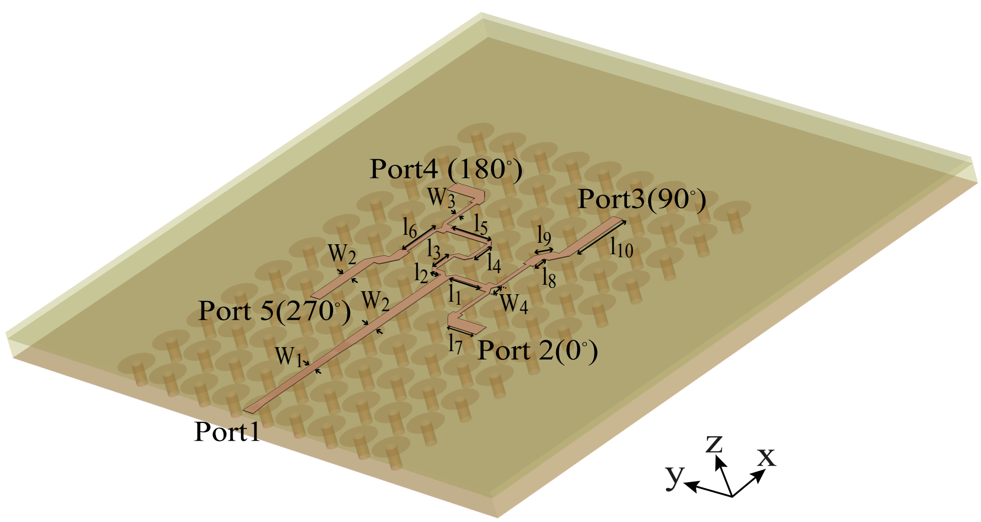

Figure 4.11: Sequential feeding network implemented by PRGW.

Table 4.2: Dimension of the proposed sequential feeding Network (mm)

Parameter	W_1	W_2	W_3	W_4	l_1	l_2	l_3
Value	0.3	0.48	0.2	0.48	1.56	0.46	0.85
Parameter	l_4	l_5	l_6	l_7	l_8	l_9	l_{10}
Value	0.85	0.89	2.04	1.4	0.52	0.7	2.55

the designed magneto electric antenna achieved the 3-dB AR bandwidth of 25.9%. But, for an 8×8 full-corporate substrate integrated waveguide (SIW) fed antenna array based on the proposed magneto electric (ME) dipole antenna element, the 3-dB AR bandwidth was reduced to 16.5%. The schematic of the designed sequential feeding network is plotted in Fig. 4.11, and its corresponding detailed dimensions are listed in Table 4.2. Since the single radiating element generates RHCP, the rotation and phase increment of the designed sequentially rotated feeding is in an anticlockwise direction. The required 90° phase difference is realized using a quarter length of PRGW lines.

It should be noted that the phase and amplitude error resulting from delay PRGW lines, limit the operating bandwidth of the designed antenna array. To alleviate this problem, a metamaterial-based sequential feeding network is introduced in [97]. However, the lumped elements adopted in the metamaterial line can cause strong parasitic effects at high frequencies.

The simulated results of power dividing and phase error of the sequential feed network are shown in Fig. 4.12 and Fig. 4.13, respectively. The phase error (phase deviation from 90°) of the

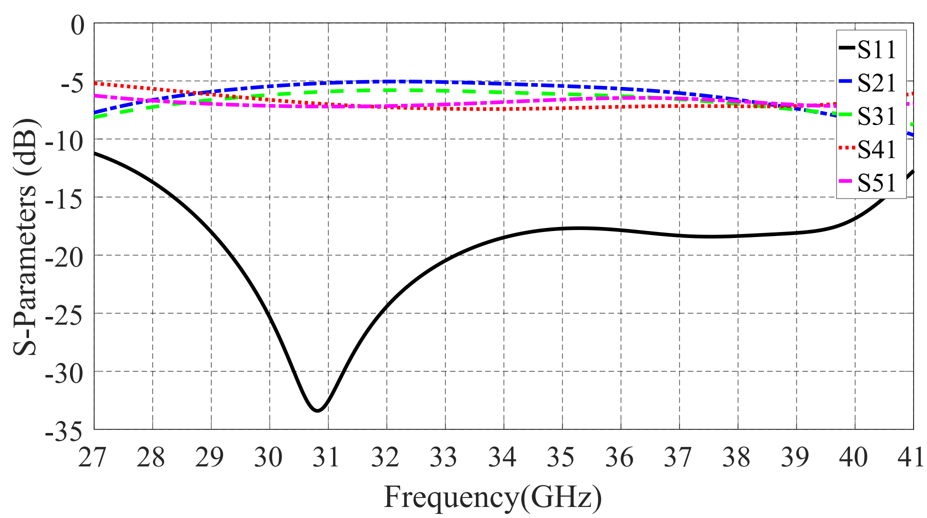

Figure 4.12: Simulated S-parameters of the designed sequential feeding network.

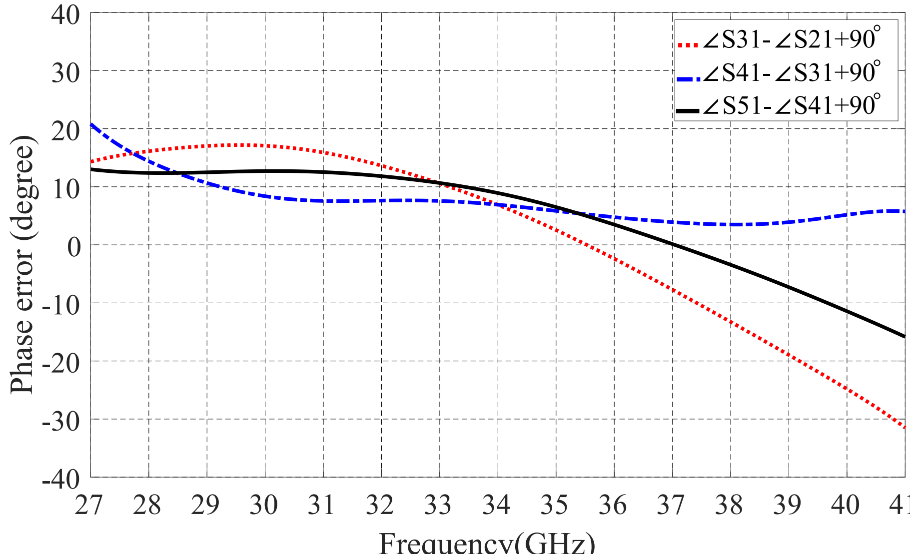

Figure 4.13: Simulated phase error between the subsequent ports of the designed sequential feeding network.

designed sequential feeding is less than 30° with the operating frequency band, and the maximum insertion loss is -7.4 dB.

4.4 Measured and Simulated Array Performance

4.4.1 Fabrication and Measurement

The proposed CP antenna array is fabricated and measured for performance verification. The photograph of the fabricated antenna prototype is plotted in Fig.4.14. First, each layer is fabricated using low-cost PCB manufacturing technology; then, all layers are stacked on top of each other using adhesive epoxy glue. It should be noted that the existence of the glue with material properties of $\epsilon_r = 3.5$, loss tangent=0.03, and thickness of $5\mu m$ is considered during the simulation process. A 2.4 mm Southwest end launch connector is connected to the input port of the antenna for the sake of measurement. The overall dimension of the prototype antenna is 27.8 mm × 23.8 mm × 2.5 mm or $3.15\lambda_0 \times 2.7\lambda_0 \times 0.28\lambda_0$, where λ_0 is the wavelength in free space.

The radiation performance of the designed antenna array is measured using the far-field measurement setup shown in Fig. 4.15. As can be seen, an LP standard horn antenna is employed as a

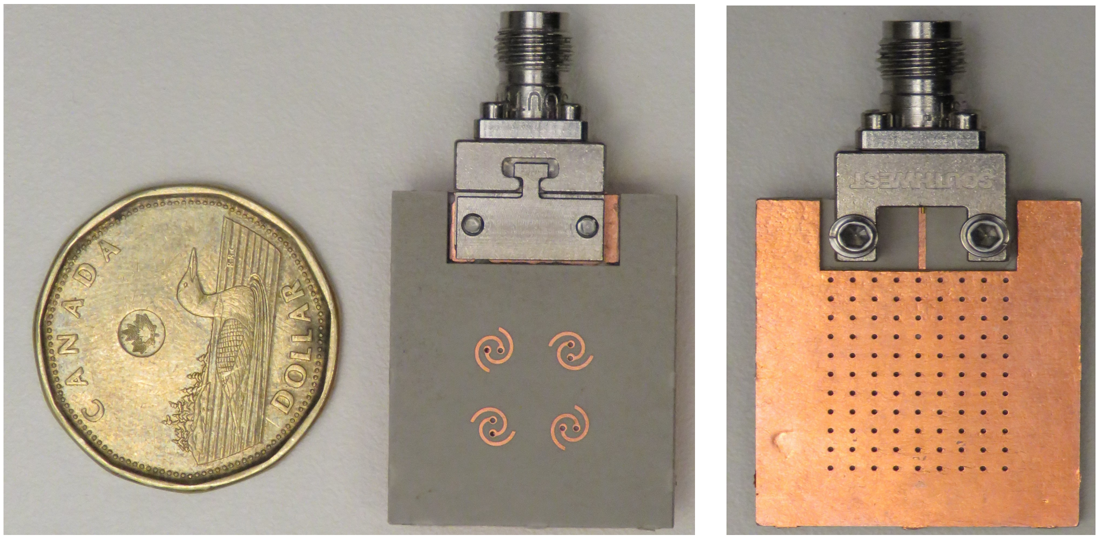

(a) (b)

Figure 4.14: Photographs of fabricated proposed antenna arrays, (a) Top view, (b) Bottom view.

transmitting antenna. The gain of the designed CP array is obtained in two steps: first measuring the LP gain using the conventional gain comparing method and then applying the gain correction factor to get the CP gain as follows [98]:

$$G_{AUT}(dBic) = G_l + 3 + G_c \tag{4.1}$$

Where G_l is the LP gain obtained from measurement and G_c is the gain correction factor calculated by:

$$G_c(dB) = 20log_{10}(0.5(1 + 10^{(\frac{-AR(dB)}{20})})) \tag{4.2}$$

For the pure CP antenna (with AR(dB)=0), $G_c = 0$ therefore, the 3 dB gain increase is required to convert the LP gain to the CP gain.

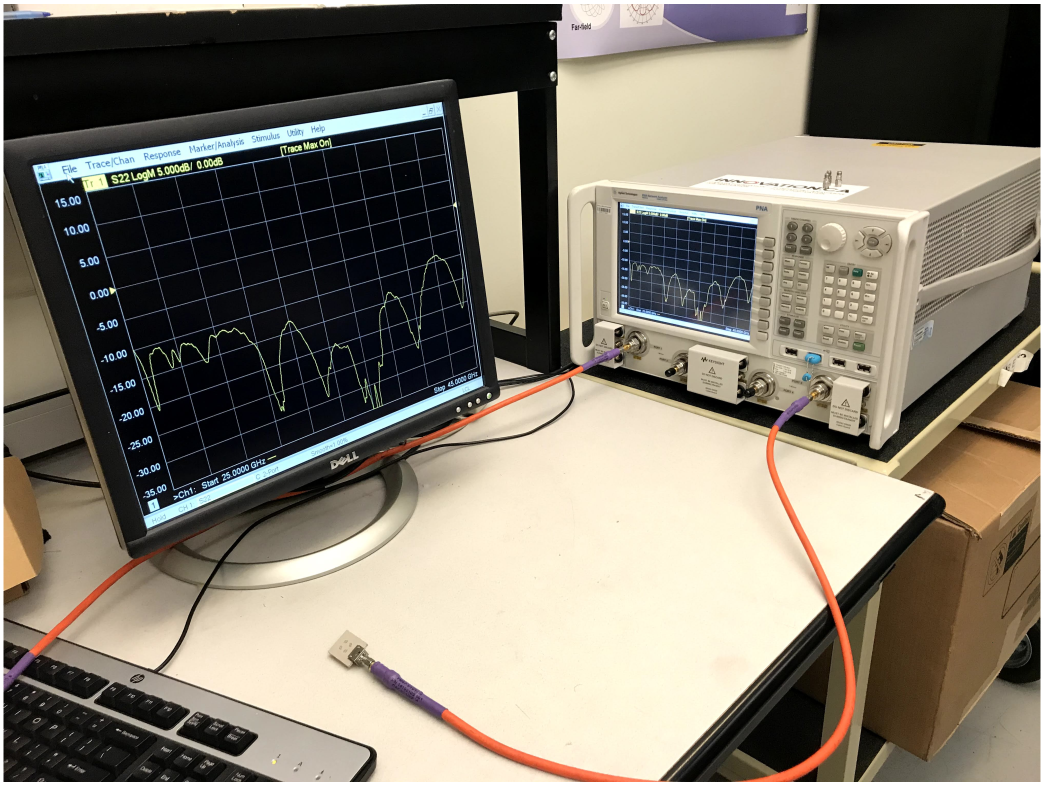

(a)

(b)

Figure 4.15: Measurement setups,(a) N5227A PNA network analyzer, (b) anechoic chamber.

4.4.2 Experimental Results

The reflection coefficient of the fabricated antenna array was measured by the mm-wave PNA network analyzer (N5227A). Fig. 4.16 compares the simulated and measured reflection coefficient of the proposed antenna array. Measured and simulated results indicate that the designed antenna has a wide impedance bandwidth. Measured and simulated matching impedance (i.e., $|S11| < -10dB$) cover the bandwidths of greater than 48.5% (25.03 GHz-41 GHz) and 48.6% (24.6 GHz- 40.4 GHz), respectively. The discrepancy between simulated and measured results for the impedance matching can be caused by the following factors: 1) smaller height of the air gap, which results in a wider matched bandwidth for the proposed antenna array; 2) the thickness of the glue, which changes the resonance frequency; 3) fabrication error in positioning vias on the top layer that leads to the resonance frequency shift, and 4) measurement errors. The simulated and measured AR and gain are plotted in Fig. 4.17.

The measured AR has the 3-dB bandwidth of 34.2% (28.6 GHz – 40.4 GHz) and simulated 3-dB bandwidth of 38.9 % (27.1 GHz – 40.2 GHz). The maximum measurement gain is 11.74 dBic at 34 GHz. The maximum measured gain is slightly lower than the simulated gain, which could be

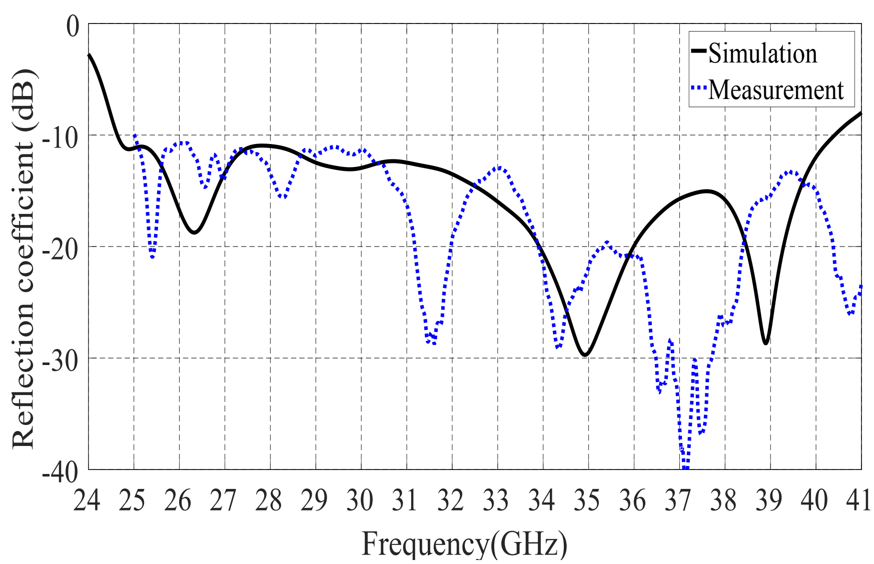

Figure 4.16: Simulated and measured reflection coefficient of the proposed antenna array.

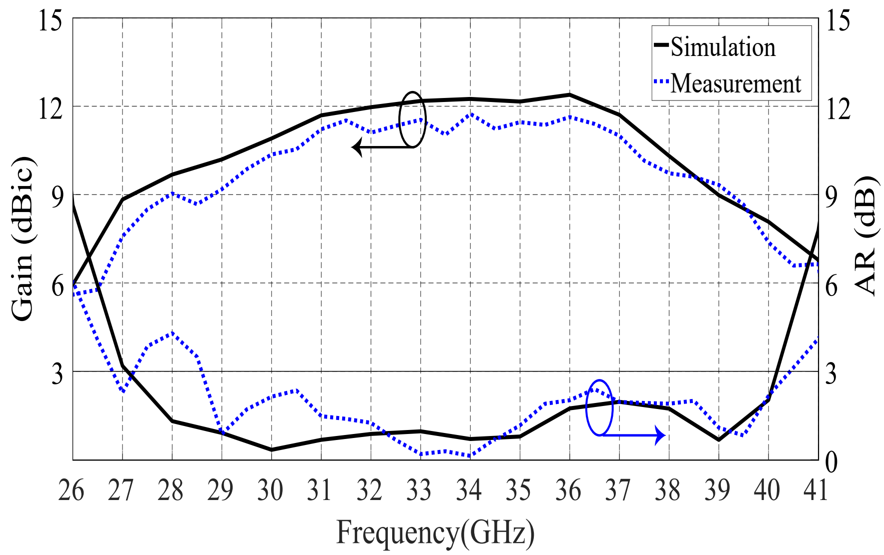

Figure 4.17: Simulated and measured RHCP gain and AR of the proposed antenna array.

due to the loss introduced by the connector and glue used to stack the fabricated layers.

The simulated and measured normalized radiation patterns in xoz- and yoz-planes for three different frequencies of 31 GHz, 34 GHz, and 37 GHz are shown in Fig. 4.18. As can be seen from this figure, the measurement results agree well with the simulated results. The maximum measured cross-polarization level (i.e., LHCP) at 34 GHz is around -21.3 dB at both XOZ and YOZ planes. Fig. 4.19 indicates the simulated radiation efficiency for both proposed single antenna element and 2×2 antenna array. As shown in this figure, the simulated radiation efficiency of the proposed antenna array exceeds 85% over the entire frequency bandwidth due to the implementation of the feeding network with a low-loss and self-package technology of PRGW. The proposed 2×2 antenna array is suitable to be used as a subarray for building larger antenna array structures. It is expected that broader AR bandwidth is obtained with a larger SR antenna array. Each round of SR suppresses the cross-polarization level further, and as a result, the AR bandwidth is enhanced [23]:

$$AR(dB) = 20log\left|\frac{1+|\frac{E_{xp}}{E_{co}}|}{1-|\frac{E_{xp}}{E_{co}}|}\right| \tag{4.3}$$

Where E_{xp} and E_{co} represent cross- and co-polar electric field components, respectively. The effect of each round of SR on co- and cross-polar components of the electric field is given in Appendix A.

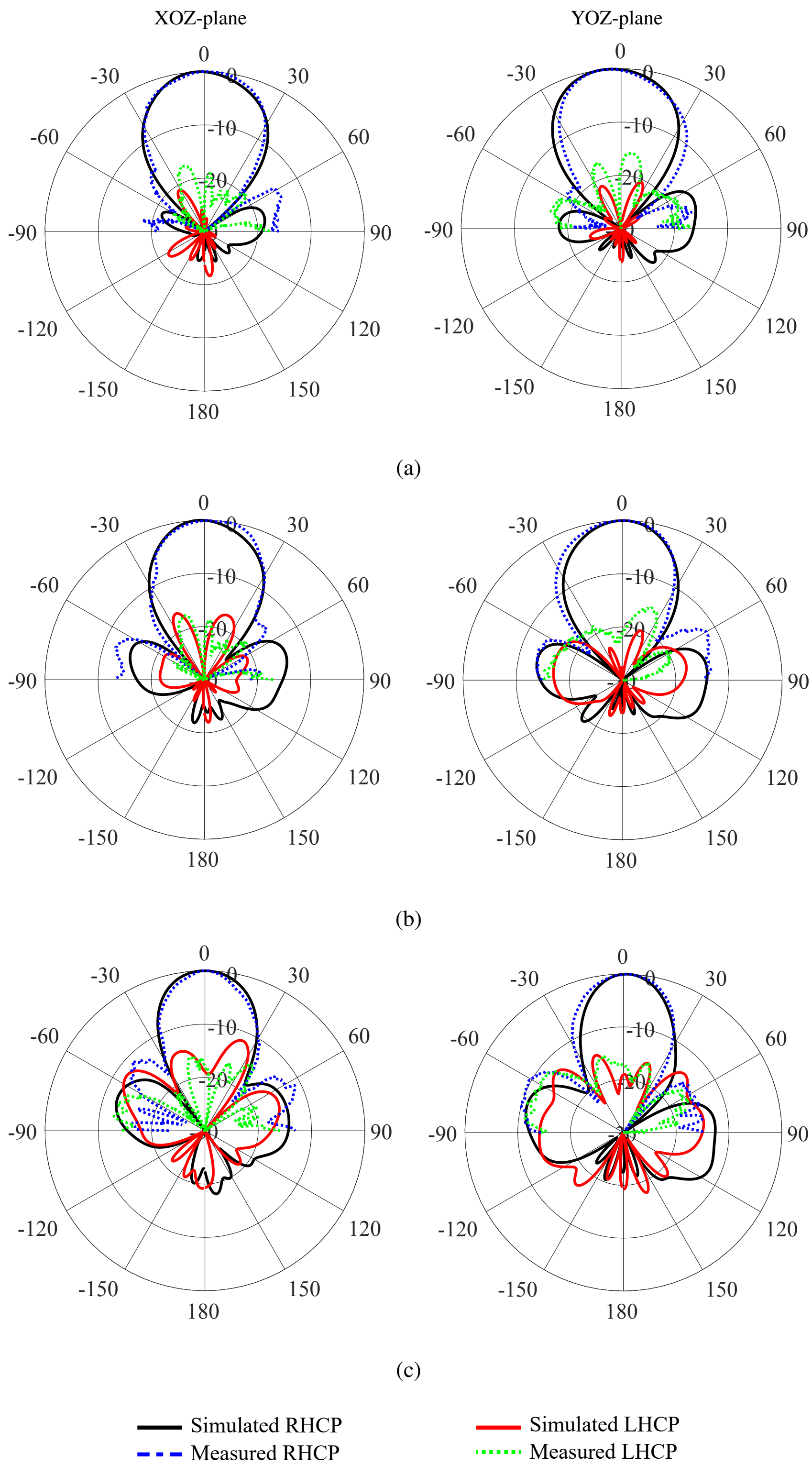

Figure 4.18: Simulated 2-D radiation patterns of the proposed antenna array at (a) 31 GHz, (b) 34 GHz, and (c) 37 GHz.

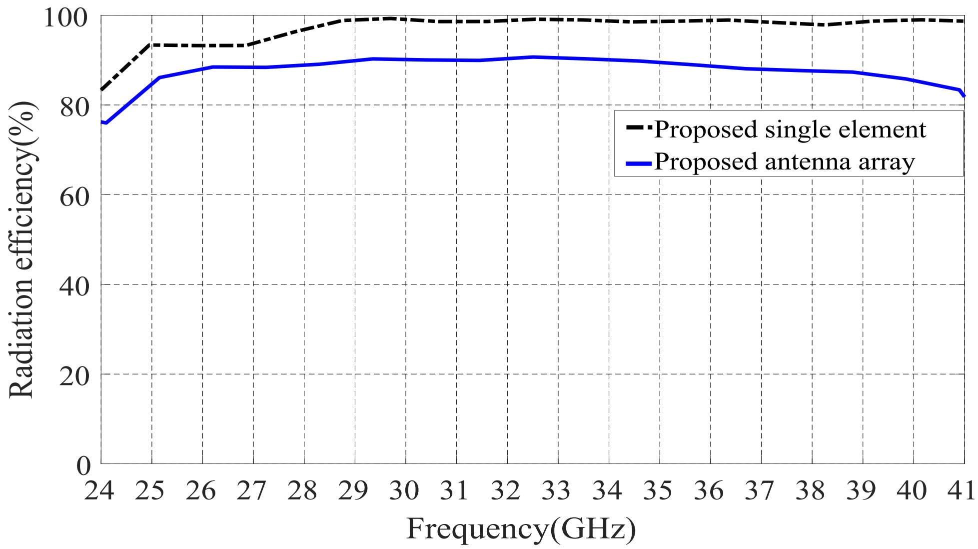

Figure 4.19: Simulated radiation efficiency of the proposed single element and antenna array.

4.4.3 Comparison and Discussion

Table 4.3 compares the measured results of the proposed mm-wave CP antenna array with some previously reported works in literature in terms of the size, impedance bandwidth, CP performance, gain, and total efficiency. The total sizes of the antenna arrays are considered for comparison. Except for the reported antenna array in [35], all the antennas listed in Table 4.3 are fabricated using low-cost PCB technology. The presented antenna array in [84] has a wide AR bandwidth. However, the impedance bandwidth is limited due to the usage of the asymmetrical spiral antenna as a radiating element. Despite having a broad impedance bandwidth of 23.3%, the proposed design in [64] suffers from a narrow AR bandwidth. Compared to antenna arrays fed by SIW and MS lines, PRGW-fed antennas exhibit higher radiation efficiency [20, 99]. Therefore, PRGW technology is a good alternative for the implementation of feeding networks at mm-wave frequencies. Since the differential feed network in [99] is realized using two layers of PRGW, including two thin air gaps, it has more difficult fabrication compared to our work. Overall, as can be seen from Table 4.3, the proposed CP antenna array archives better reflection coefficient, AR, and gain bandwidth with high radiation efficiency compared to the other CP antenna arrays listed in this table.

Table 4.3: Comparison Between the proposed mm Wave CP antenna array and some related works in the references

Ref.	Element	Freq.	Element Num.	Feeding Network	Size (λ_0^2)	Imp. BW%	AR BW%	Gain BW%	Peak Gain (dBic)	ϵ_{rad}%
[35]	Helical	60	4×4	Full corporate (Strip line)	2.4×2.0	22	20	15.1	15.2	54.9
[84]	Spiral	60	4×4	Sequential (SIW)	4.9×4.9	14.1	21.1	16.4	19.5	> 77
[64]	Slot	28	2×2	Sequential (SIW)	3.46×3.46	23.3	7.7	7	10.78	NG*
[92]	Patch	26	2×2	Sequential (SIGW)	3.9×3.5	25.6	19	25	11.53	NG*
[99]	Aperture	30	2×2	Differential (PRGW)	6.1×4.9	15.6	10	14	13.5	> 84
[20]	Slot spiral	38	2×2	Sequential (PRGW)	4.4×4.4	23.7	22.5	21	12.3	> 82
[100]	ME-dipole	27	4×4	Sequential (SIW)	7.0 ×5.0	27.7	27.8	25.3	20.2	78
This work	Spiral	34	2×2	Sequential (PRGW)	3.15×2.7	> 48.5	34.2	32.4	11.74	> 85

*The numerical data is not given in the referenced paper.

4.5 Summary

We presented a wideband compact CP spiral antenna array for mm-wave applications. The patch dipole beneath the spiral arms helps the spiral to shrink but at the expense of adding one layer. Also, the connecting vias to the patch dipole provide a 180° phase difference for the spiral antenna to be excited with its fundamental mode. To further increase the AR bandwidth, the proposed single element is employed in the SR feeding network. The sequential feeding is implemented using PRGW technology, which benefits from the design flexibility of MS lines and, at the same time, having low dispersion. The prototype of the planar CP antenna array has been designed, fabricated and measured. The measured results are in good agreement with the simulated results. Based on the measured results, the fabricated antenna array has a wide impedance bandwidth of more than 48.5%, 3-dB AR of 34.2% and 3-dB gain bandwidth of 32.4% with a maximum gain of 11.74 dBic over the operating frequency bandwidth. In addition, the proposed antenna array exhibits high radiation efficiency due to the implementation of the feeding network with PRGW technology.

Chapter 5

Millimeter-Wave Dual Circularly Polarized Antenna Array

5.1 Introduction

Dual polarized antennas have drawn considerable attention due to increasing channel capacity and enabling frequency reuse [101]. In particular, dual circularly polarized (CP) antennas are more desirable because they benefit from the features mentioned above and have the advantages of CP antennas, such as eliminating multipath fading and suppressing polarization mismatch between the transmitter and receiver antennas [102].

The proposed mm-wave dual CP antennas and arrays in the literature are based on either the substrate integrated waveguide (SIW) [103–106] or waveguide [107–109]. MM-wave antennas based on SIW structures have the advantage of easy integration, small size, and low-cost fabrication process. However, they exhibit low radiation efficiency due to the high dielectric loss at mm-wave frequencies. This problem would be more serious for antenna arrays with the large size of the feeding networks [103],[32]. Antennas realized by waveguides could be an effective solution due to their air-filled structure and low insertion loss but at the cost of difficulties in fabrication and low integration capability with planar circuits.

Printed ridge gap waveguide (PRGW) technology has been widely used in mm-wave antenna designs as it has lower insertion loss compared to SIW based structures and is fully compatible with printed circuit board (PCB) technology [68, 69, 110]. A few mm-wave dual linearly polarized (LP) polarized antennas based on PRGW technology have been reported, which exhibits high radiation efficiency [111–113]; However, to the best of our knowledge, no mm-wave dual CP antenna based on PRGW has been proposed so far.

In this chapter, we develop a wideband, low profile dual CP shared–aperture antenna array with the feeding network implemented in a single PRGW layer, contrary to previously reported PRGW dual LP antennas that required two different laminate layers for the feeding networks of each orthogonal polarization [112]-[113]. The LP magneto-electric (ME) dipole antenna is chosen as a radiating element because of its broad bandwidth and simple structure, then each antenna element rotated by $45°$ to alleviate the problem of high cross-polarization at off-broadside directions. Sequential rotation (SR) technique [89, 114] is used to generate CP radiation from LP antenna elements. The proposed PRGW SR feeding is simplified to avoid the usage of a phase shifter. The 2×2 ME dipole antenna array elements are sequentially rotated and fed with equal amplitude and $90°$ phase difference in clockwise or anti-clockwise direction depends on the excitation of each input port. The presented dual CP antenna array has the merits of wide operating bandwidth, lightweight, convenient integration, low manufacturing cost, reduced complexity of the feeding network, and high radiation efficiency.

The rest of this chapter is organized as follows; Section 5.2 first describes the working principle of the proposed PRGW feeding network, then presents the simulation results for the feeding network and its components. The design of the $45°$ ME antenna is given in Section 5.3. Section 5.4 presents the PRGW dual CP antenna array's simulated and experimental results and compares them with other similar works. Finally, section 5.5 concludes this chapter.

5.2 Dual Circularly Polarized Feeding Structure

The block diagram of the proposed feeding structure to realize both senses of circular polarization is shown in Fig. 5.1. It consists of two rat-race couplers, two-directional couplers, and one crossover, all printed on the same layer. P1 and P2 are the input ports, and P3-P6 are the output ports that would feed the 2×2 sequentially rotated antenna array. The proposed feeding structure

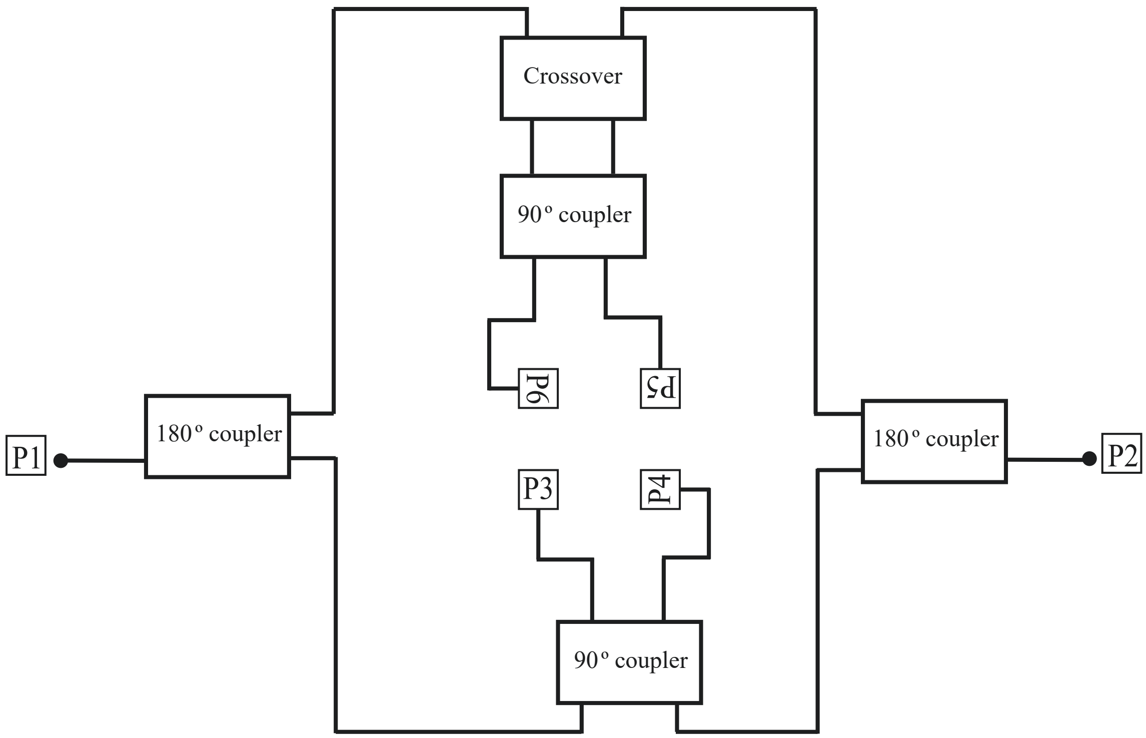

Figure 5.1: The schematic of the proposed dual polarized feeding network.

provides 90° phase increments in clockwise or anticlockwise direction between the adjacent output ports, depending on the excitation of each input port:

$$\angle S_{41} - \angle S_{31} = \angle S_{51} - \angle S_{41} = \angle S_{61} - \angle S_{51} = S_{31} - \angle S_{61} = -90^{\circ} \tag{5.1a}$$

$$\angle S_{42} - \angle S_{32} = \angle S_{52} - \angle S_{42} = \angle S_{62} - \angle S_{52} = S_{32} - \angle S_{62} = +90^{\circ} \tag{5.1b}$$

All components are realized using PRGW technology. The PRGW section includes three layers, an artificial magnetic conductor (AMC) layer, which consists of 2-D distributions of circular mushroom unit cells, a thin layer on top of the AMC layer, and an air gap realized by a thin substrate layer that acts as a spacer. The geometry and dimensions of the designed mushroom unit cell and the simulated dispersion diagram of the PRGW line is shown in Fig. 5.2. All PRGW components are printed on Rogers 6002 with ϵ_r =2.94 and loss $tan\delta = 0.0012$ and thickness of 0.254mm.

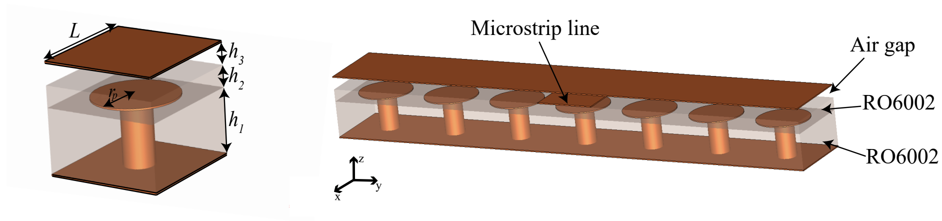

(a)

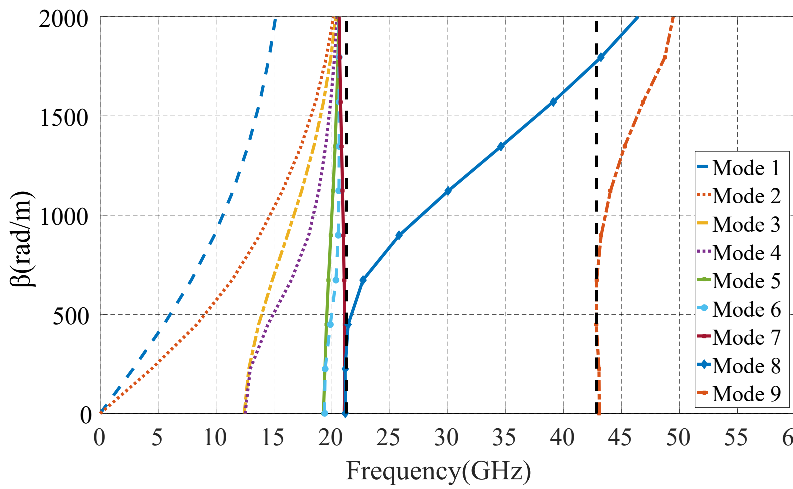

(b)

Figure 5.2: (a) Mushroom unit cell geometry ($h_1 = 0.762mm, h_2 = h_3 = 0.254mm, L = 1.7mm, W_p = 0.7mm, r_p = 0.2mm$), (b) Dispersion diagram of the PRGW.

5.2.1 Printed Ridge Gap Rat-Race Coupler

In order to divide the input signal into two signals with equal amplitude and 180° phase difference, a wideband two-section rat-race coupler based on the PRGW technology has been designed [115]. Fig. 5.3 shows the geometry of the proposed rat-race, which is composed of four horizontal symmetrical $\lambda_g/4$ lines and three vertical $\lambda_g/2$ lines (where λ_g is the guided wavelength at the center frequency). It has only one feeding port since there is no need for the in-phase output signals in our design. The optimized dimensions of the proposed rat-race coupler are summarized in Table 5.1. Fig. 5.4(a) and Fig. 5.4 (b) show the simulated results for the S-parameter amplitude and phase, respectively. As shown in these figures, the amplitude imbalance and phase imbalance of output ports are -3.2±0.5 dB and 180°±6°, respectively. The reflection coefficient is less than -15 dB within the frequency range of 25.48-35 GHz.

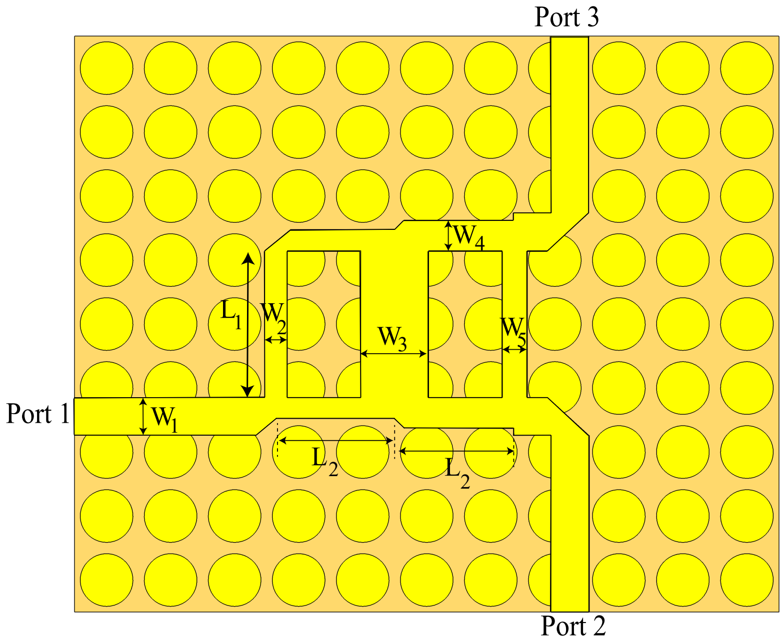

Figure 5.3: Geometry of the proposed wideband PRGW rat-race coupler.

Table 5.1: Dimension of the proposed wideband PRGW rat-race coupler (mm)

Parameter	W_1	W_2	W_3	W_4
Value	1	0.6	1.80	0.81
Parameter	W_5	L_1	L_2	
Value	0.67	3.8	3.1	

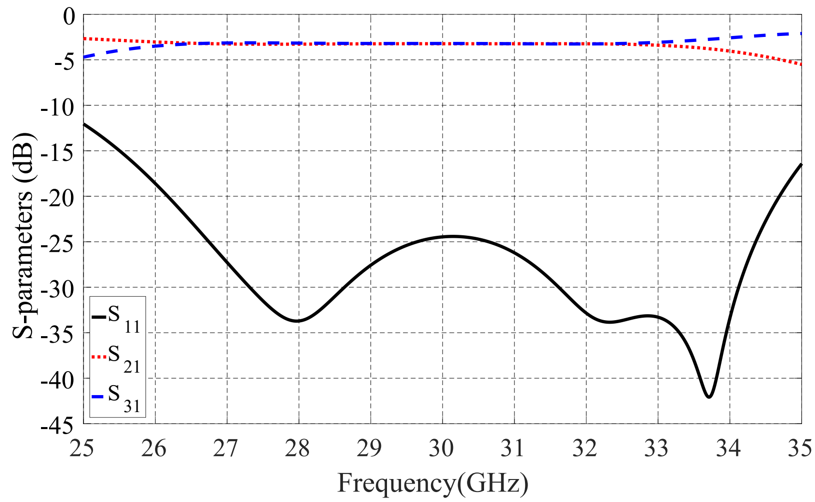

(a)

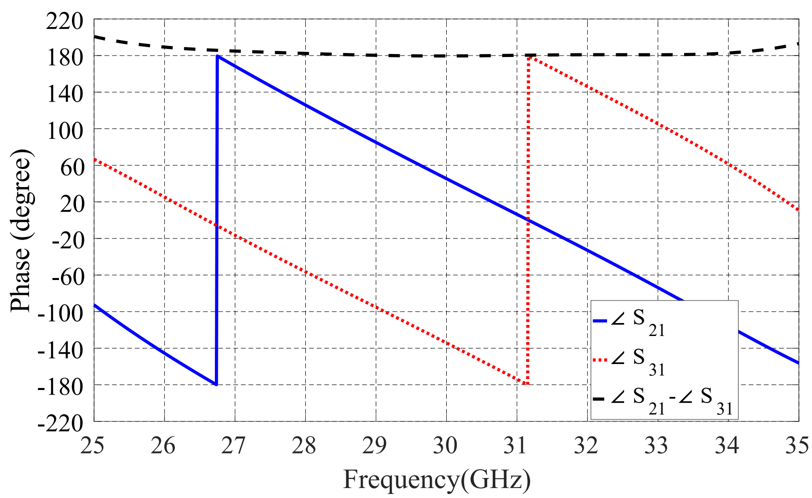

(b)

Figure 5.4: Simulated results of the proposed wideband PRGW rat-race coupler, a) amplitude, (b) phase response.

5.2.2 Printed Ridge Gap 90° Directional Coupler

The configuration and dimensions of the proposed wideband two-section 90° PRGW coupler are illustrated in Fig. 5.5 and Table 5.2, respectively. Contrary to the conventional design of two section coupler, it has four horizontal $\lambda_g/4$ lines(where λ_g is the guided wavelength at the center frequency) and two vertical $\lambda_g/2$ lines, making the designed coupler more compact while keeping the wideband performance [116, 117]. Fig. 5.6 (a) and Fig. 5.6 (b) show the simulated results of

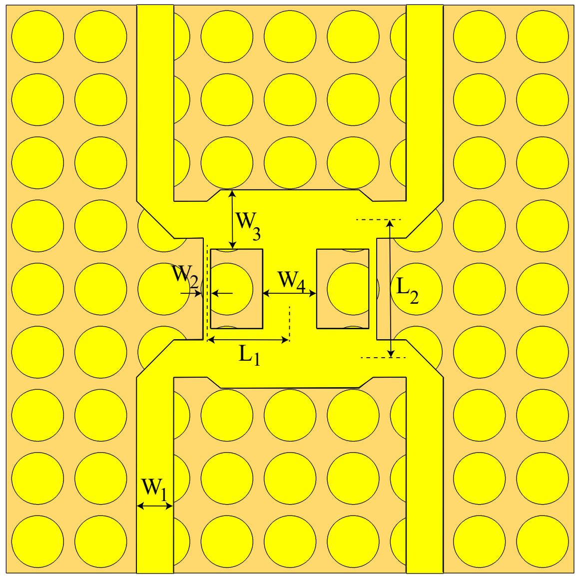

Figure 5.5: Geometry of the proposed wideband PRGW 3-dB directional coupler.

Table 5.2: Dimension of the proposed wideband PRGW directional coupler (mm)

Parameter	W_1	W_2	W_3	W_4	L_1	L_2
Value	1	0.25	1.80	0.81	3.8	2.85

S-parameters amplitude and output phase difference. The designed PRGW coupler has impedance and isolation bandwidth of almost 28.4% ($\mid S11 \mid < -15$ dB and $\mid S14 \mid < -15$ dB) from 26.3-35 GHz, the amplitude imbalance of -3.2 ±0.6 dB and phase imbalance of -90.5°±3°. The proposed PRGW coupler is compact with the size of $0.5\lambda_0 \times 0.45\lambda_0$.

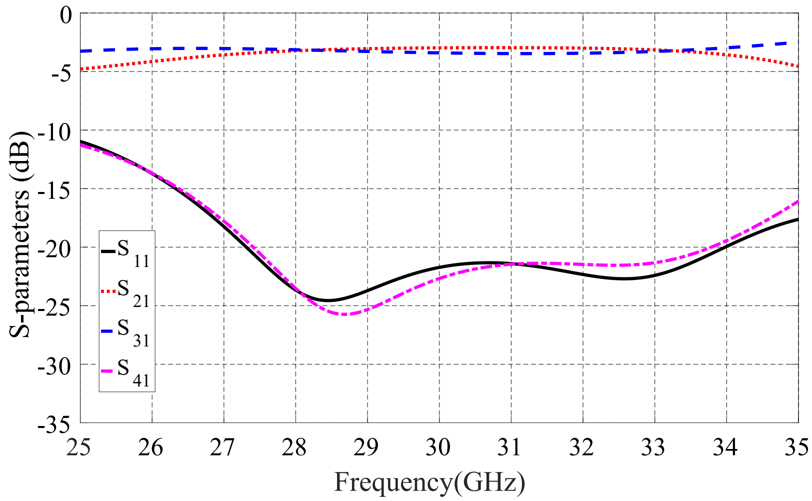

(a)

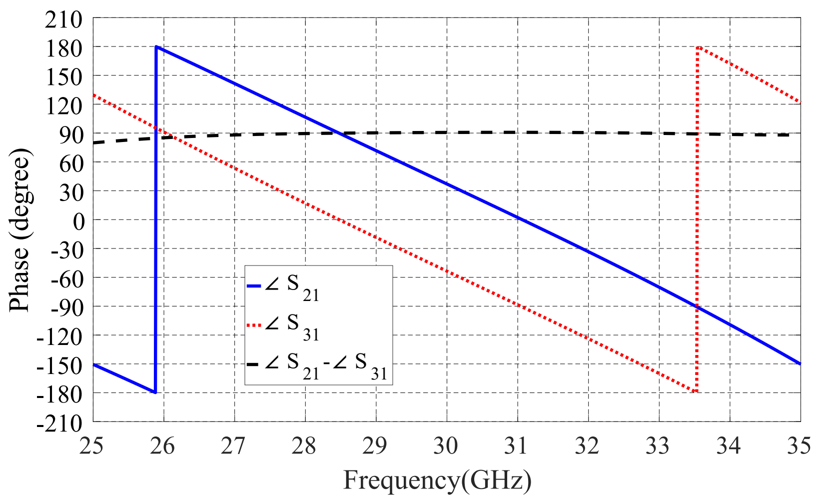

(b)

Figure 5.6: Simulated results of the proposed wideband PRGW 3-dB directional coupler, a) amplitude, (b) phase response.

5.2.3 Printed Ridge Gap Crossover

The crossover has a significant impact on the performance of the proposed feeding network. As shown in Fig. 5.1 , output ports of the crossover (port 2 and port 3 in Fig. 5.7) are connected to input ports of the coupler; therefore, it is crucial to have $\mid S12 \mid$ small enough to ensure equal power division at output ports of the coupler. By cascading the designed 3-dB directional coupler in the previous section, a four-section crossover is built and optimized to achieve maximum isolation and

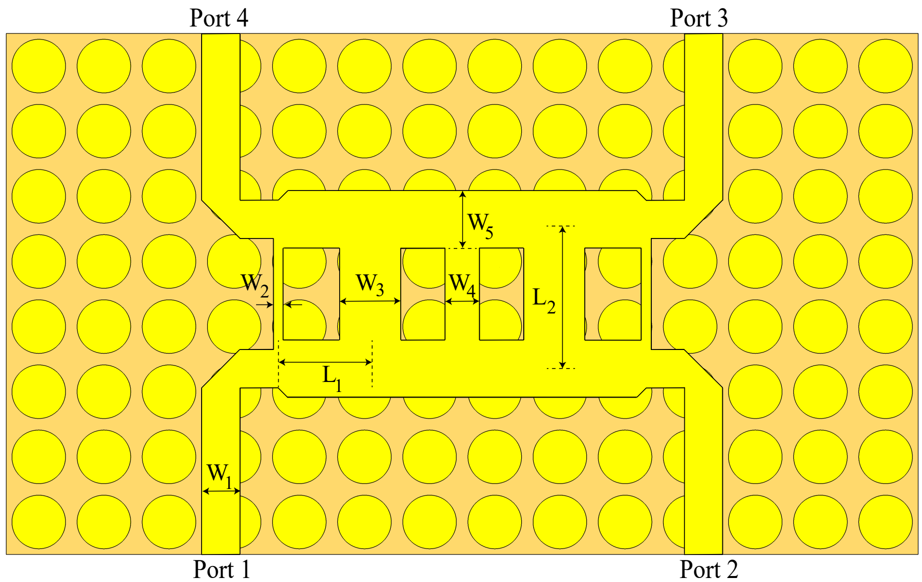

Figure 5.7: (a) Geometry of the proposed wideband PRGW crossover, (b) Simulated S-parameters.

Table 5.3: Dimension of the proposed wideband PRGW directional coupler (mm)

Parameter	W_1	W_2	W_3	W_4	L_1	L_2
Value	1	0.25	1.80	0.81	3.8	2.85

broadband bandwidth. The geometry of the proposed PRGW crossover is illustrated in Fig. 5.7, and its dimensions are listed in Table 5.1. From the simulation result in Fig. 5.8, the bandwidth is 27.5 % (from 25.4 to 33.5 GHz.) for return loss and isolation less than 15 dB. The insertion loss is better than 0.4 dB within the bandwidth. The proposed crossover has the compact size of $0.97\lambda_0 \times 0.54\lambda_0$.

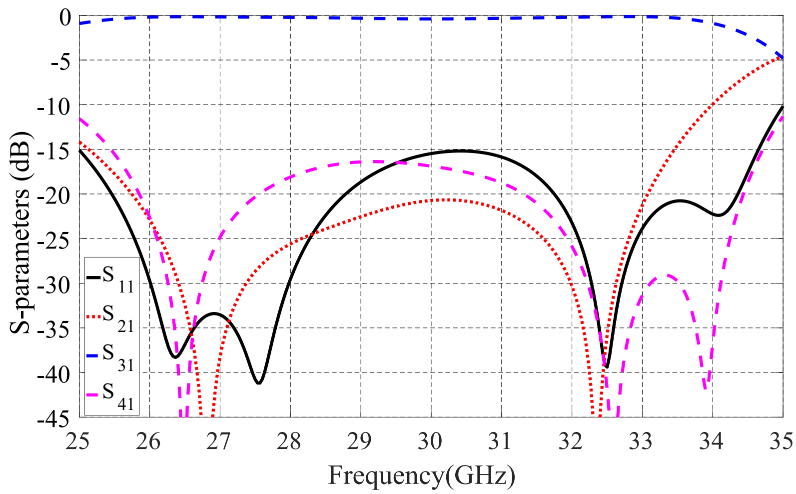

Figure 5.8: (a) Geometry of the proposed wideband PRGW crossover, (b) Simulated S-parameters.

5.2.4 PRGW Feeding Network

By integrating the components designed in previous sections, the wideband two-port feeding network is built as shown in Fig. 5.9. Input ports (port 1 and 2) of the designed feeding network provide output phases of -90 ° between output ports in clockwise or anticlockwise directions without the need to have additional phase shifters contrary to works in [118] and [105]. For instance, when port 1 is excited and port 2 is terminated with matching load, the output signals have equal magnitude and -90 ° phase shift in anti-clockwise direction, resulting in RHCP beam.

The simulated magnitude and phase difference of the S-parameters of the designed feeding network for excitation from input ports are shown in Fig. 5.10, Fig. 5.11 and Fig. 5.12, respectively. It is worth noting that due to the reciprocity of the sequential feeding networks, $S_{ij} = Sji$ for $i \neq j$.

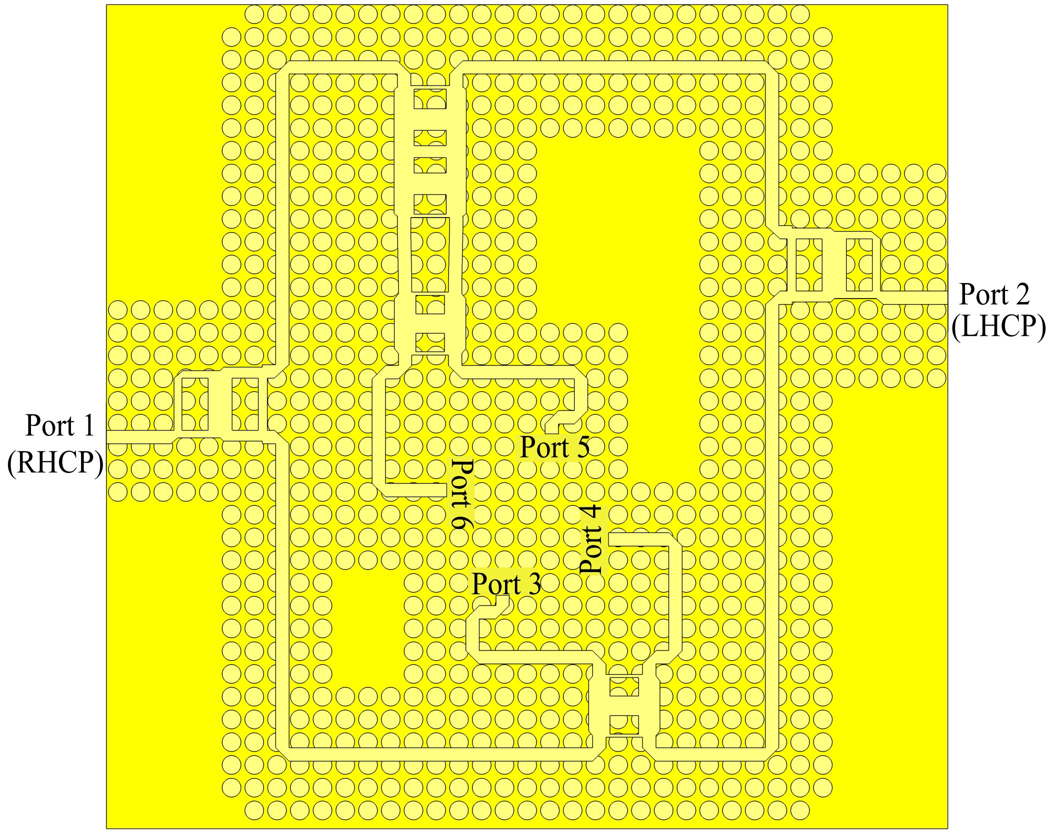

Figure 5.9: Geometry of the proposed feeding network for dual sense of CP antenna.

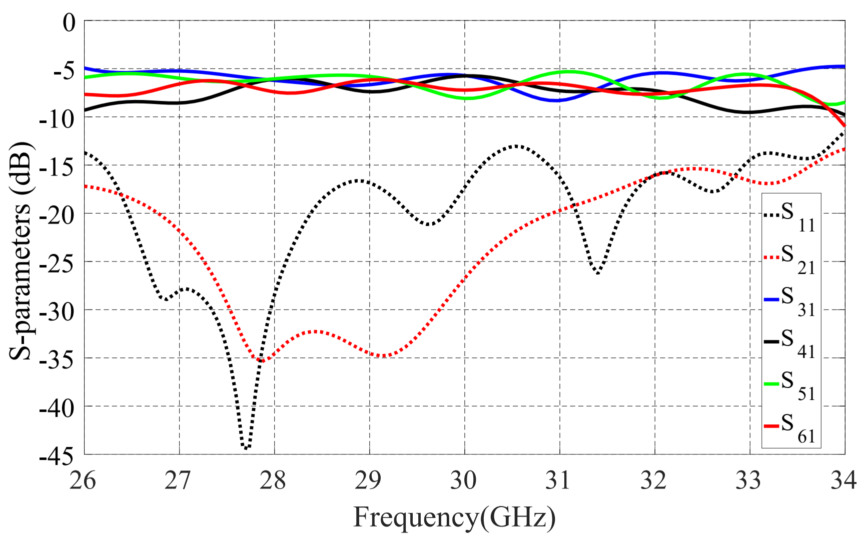

Figure 5.10: Simulated S-parameters of the proposed feeding network for excitation from port 1.

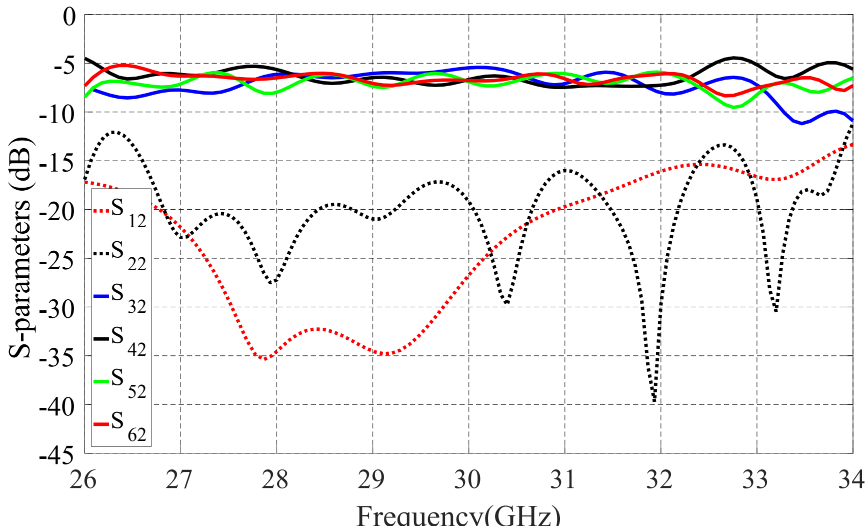

Figure 5.11: Simulated S-parameters of the proposed feeding network for excitation from port 2.

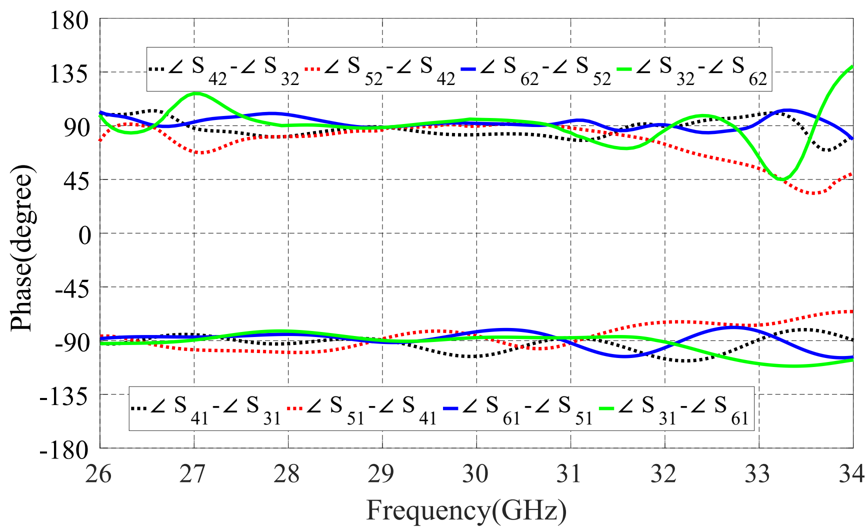

Figure 5.12: Phase difference between the output ports for the excitation of port 1 and port 2.

5.3 45° ME Dipole Antenna Design

ME-dipole antenna has been chosen as radiating element due to its wideband performance, stable radiation and low cross polarization across the operating frequency bandwidth. The ME-dipole antenna was first proposed in 2008 [119] and then has been extensively studied in the literature ([8, 120–122]). The concept of ME dipole antennas is based on the theory of Huygens sources in which two orthogonal electric and equivalent magnetic dipoles are excited simultaneously. The

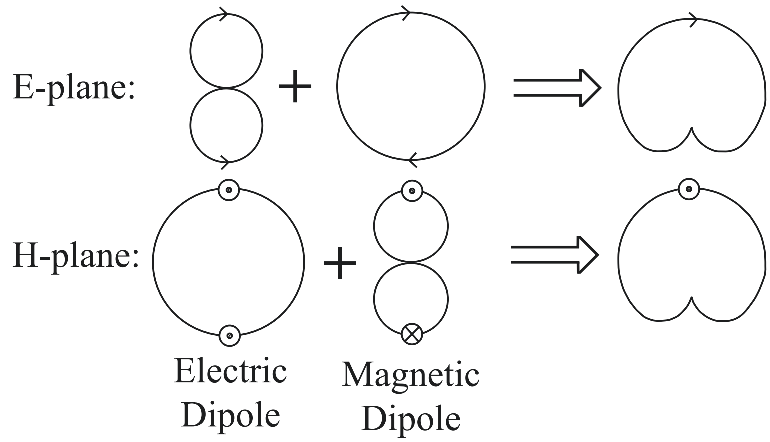

Figure 5.13: Superposition of radiation patterns of the electric and the magnetic dipoles [124].

combination of electric and magnetic dipoles with equal amplitude and phase results in identical broadside radiation patterns in E and H planes over a wide frequency range [123, 124]. Fig. 5.13 shows the superposition of electric and magnetic dipole radiation patterns in two principal planes.

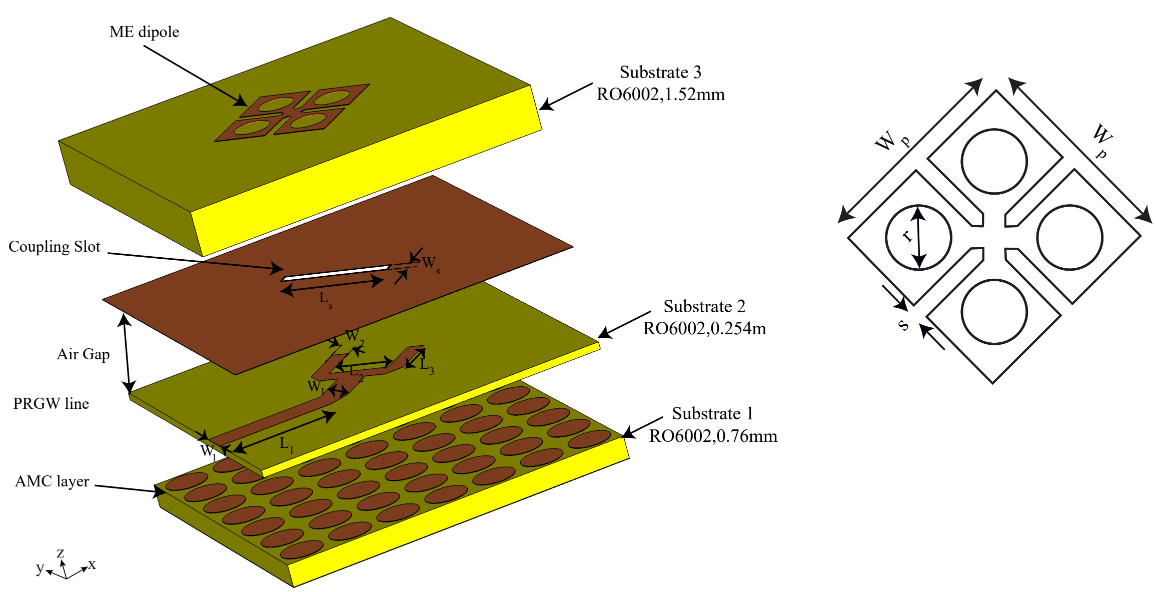

Figure 5.14: Configuration of the proposed 45° ME dipole antenna.

Table 5.4: Dimension of the proposed $45°$ ME dipole antenna (mm)

Parameter	W_1	W_2	W_s	W_p	L_s
Value	1	0.6	0.45	3.9	3.79
Parameter	L_1	L_2	L_3	r	s
Value	3.93	2.1	1.8	1.18	0.31

To mitigate the problem of high cross-polarization level at diagonal planes of 2×2 sequentially rotated array with LP elements, the ME dipole antenna is rotated by 45° degrees with respect to the z-axis. The geometry of the 45° Magneto-electric dipole (ME) antenna with the PRGW section is shown in Fig. 5.14. It consists of four printed 45° tilted parasitic square patches on Rogers 6002 with the thickness of 1.52mm, ϵ_r=2.94, $tan\delta = 0.0012$. All metallic patches are connected to the ground plane using vertical vias. The coupling slot is etched on the bottom copper side of substrate 1. The fork-shaped feeding line is printed on Rogers 6002 with a thickness of 0.254 mm and is placed over an artificial magnetic conductor (AMC) layer. The dimensions of the designed 45° ME dipole antenna are listed in Table 5.4. The simulation results for refection coefficient, gain, and radiation patterns in E- ($\phi = 45°$)and H- plane ($\phi = 135°$) are shown in Fig. 5.15. The designed 45° ME dipole has -15 dB impedance bandwidth of 30% from 25.7 GHz to 34.9 GHz and realized gain in a range of 7.5 dBi to 9.4 dBi over the whole impedance bandwidths.

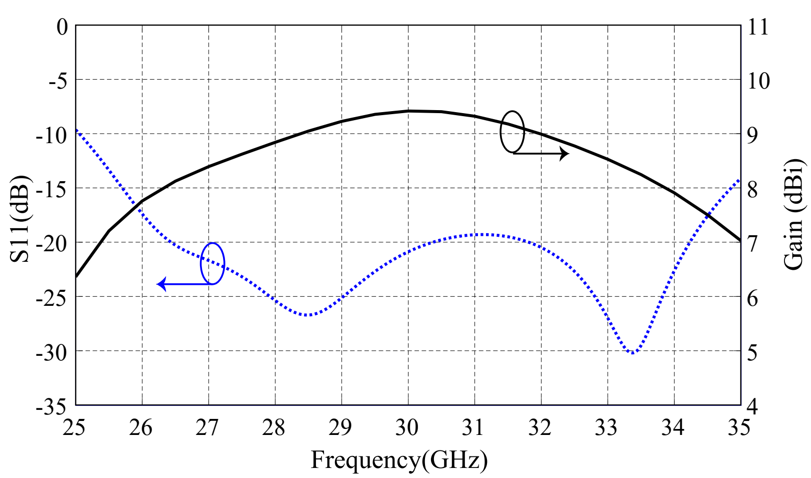

Figure 5.15: Simulated reflection coefficient and realized gain of the proposed antenna .

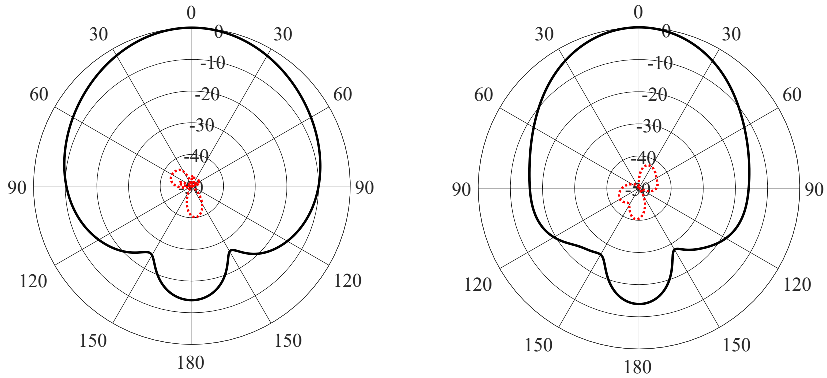

(b)

Simulated Co-pol   Simulated Cross-pol

Figure 5.16: Simulated radiation patterns of the proposed antenna at 30 GHz.

5.3.1 Comparison Between 2×2 Sequentially Rotated 45° ME Dipole and ME Dipole Array

To better understand the impact of shifting polarization to the ϕ=45° plane on the cross-polarization performance, two 2×2 SR arrangements with ME dipole and 45° ME dipole antennas are simulated in the CST studio. As shown in Fig. 5.17a and Fig. 5.17b the distance between the radiating elements in both cases remains constant. It can be observed from Fig. 5.18a and Fig. 5.18b that the XPD is lower for the 2×2 SR 45° ME dipole array at ϕ=0° and ϕ=90° planes for both RHCP and LHCP cases. At the diagonal planes ($\phi = \pm 45°$), the SR 45° ME arrangement has equal XP SLL for +90° (LHCP) and -90° (RHCP) phase shifts between the antenna elements.

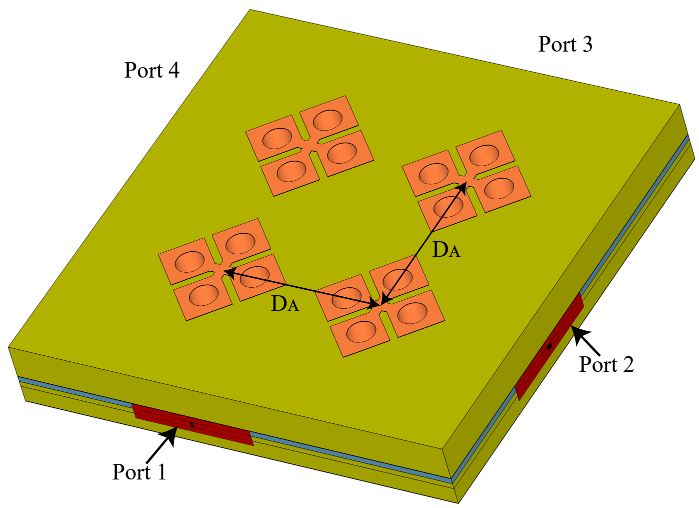

(a)

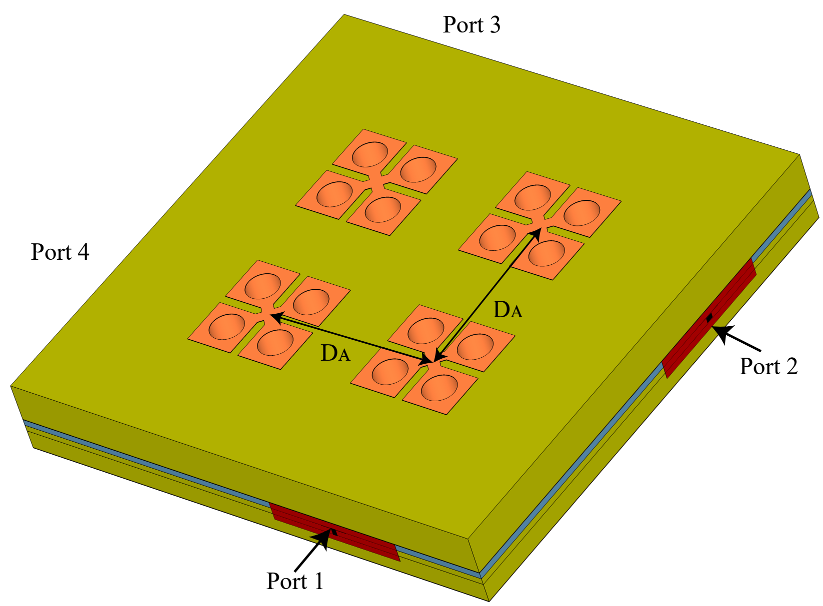

(b)

Figure 5.17: (a) SR 45° ME dipole antenna, (b) SR ME dipole antenna.

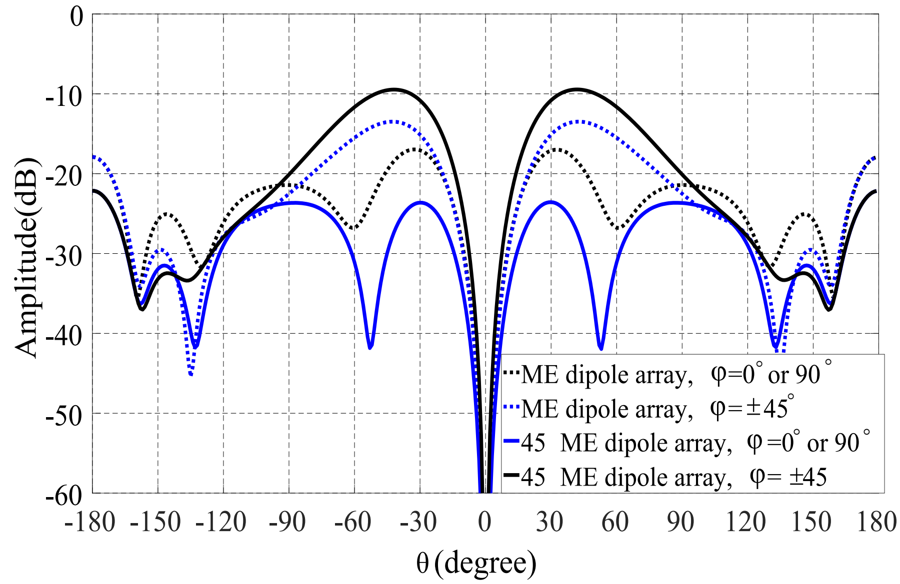

(a)

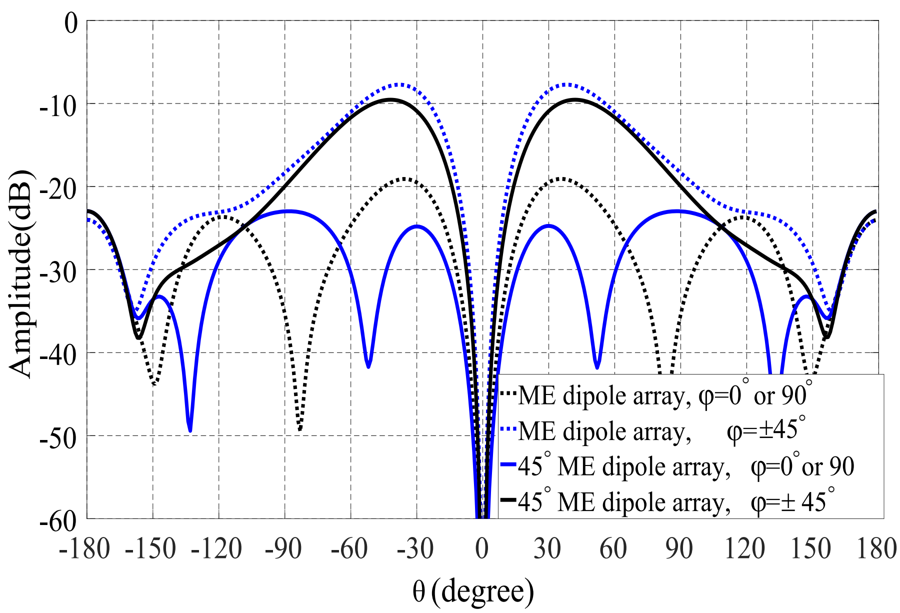

(b)

Figure 5.18: Simulated normalized cross polarization at $\phi = 0°$ or $90°$, and $\phi = \pm 45°$ (a) RHCP. (b) LHCP.

5.4 Circularly Polarized Antenna Array

5.4.1 2×2 Array

The feeding network designed in section II is integrated with a 2×2 sequentially rotated $45°$ME dipole antenna array designed in section III, as shown in Fig. 5.19. It should be noted that the antenna element's spacing should be less than $0.7\lambda_0$(λ_0 is the free space wavelength at the center frequency) to enhance the XPD at off broadside directions and consequently decreasing the gain loss of antenna array consists of LP elements [59]. To facilitate the measurement, a wideband microstrip to PRGW line is designed and printed on the spacer substrate [125].

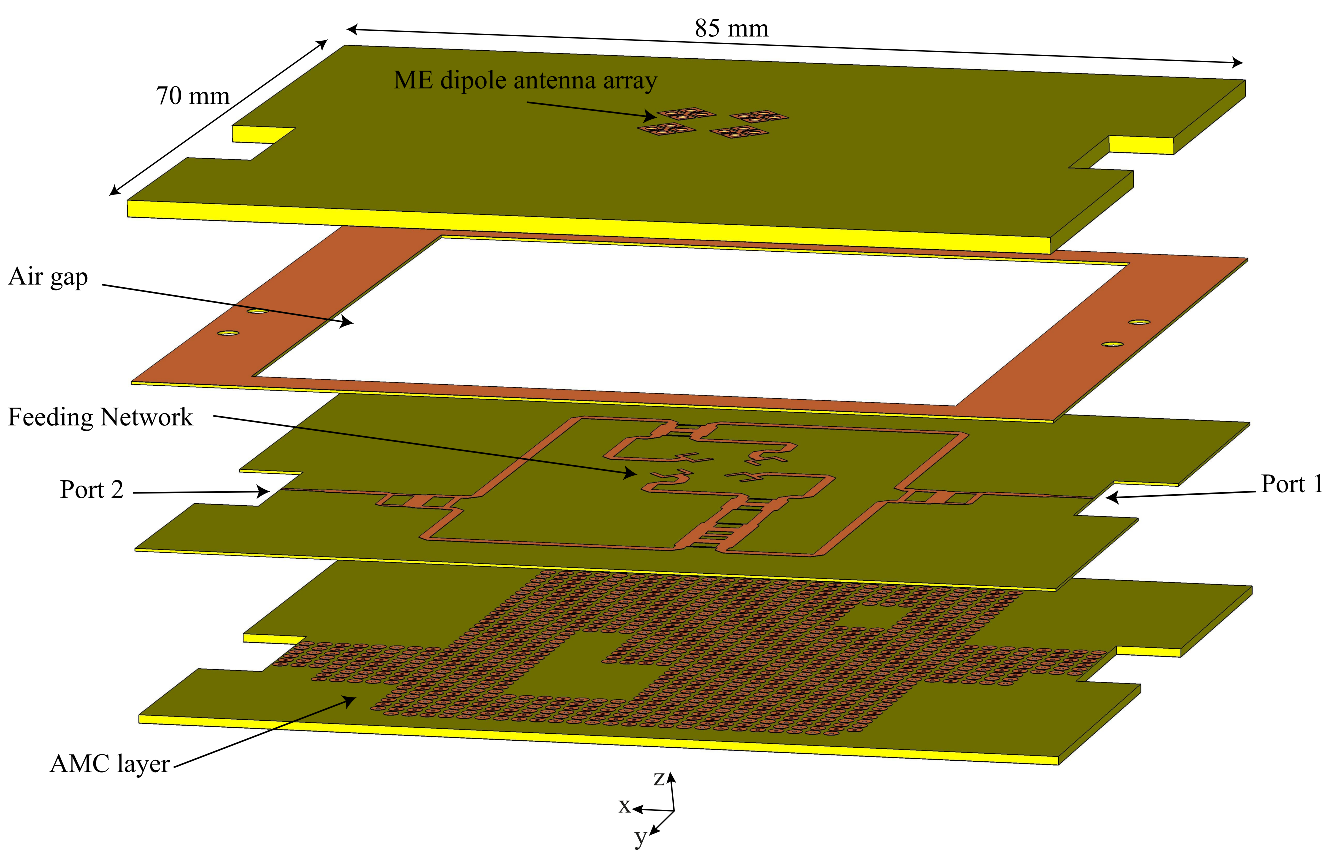

Figure 5.19: Expanded view of dual-polarized ME dipole antenna array.

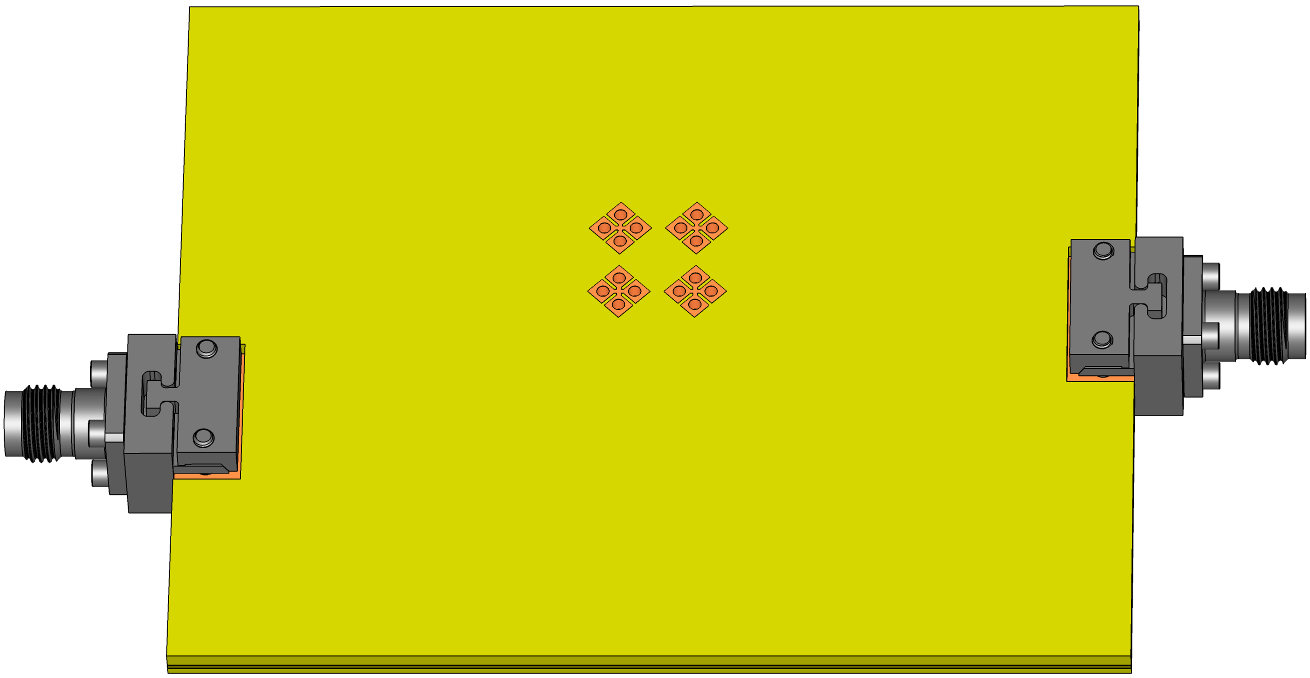

Figure 5.20: 3D view of the 2×2 dual-polarized ME dipole antenna array with the end launch connector.

As shown in Fig. 5.20, the spacer layer is inserted into the air gap in the PRGW region to ensure good electrical contact between the PRGW line and the microstrip line printed on the spacer substrate. The total size of the designed antenna array is $70mm \times 85mm \times 2.8mm$ and aperture area has the size of $12.3mm \times 12.3mm$.

5.4.2 Fabrication and Measurement

A prototype is fabricated using multilayer PCB technology. Two 2.4 mm end-launch connectors from Southwest Microwave Inc. are employed for the measurement. Fig. 5.21 demonstrates the top and bottom view of the fabricated prototype. The S-parameters are measured using N52271A PNA network analyzer. The radiation properties are measured in an anechoic far-field chamber.

The measured and simulated reflection coefficients are given in Fig. 5.22. The simulated impedance bandwidth for port 1 and port 2 are 25.9% (from 26.2 GHz to 34 GHz) and 24.2% (from 26.6 GHz to 34 GHz), respectively; while the measured impedance bandwidth for port 1 and port 2 are 23.5% (from 26.3 to 33.3 GHz) and 22.2%(from 26.4 to 33 GHz), respectively.

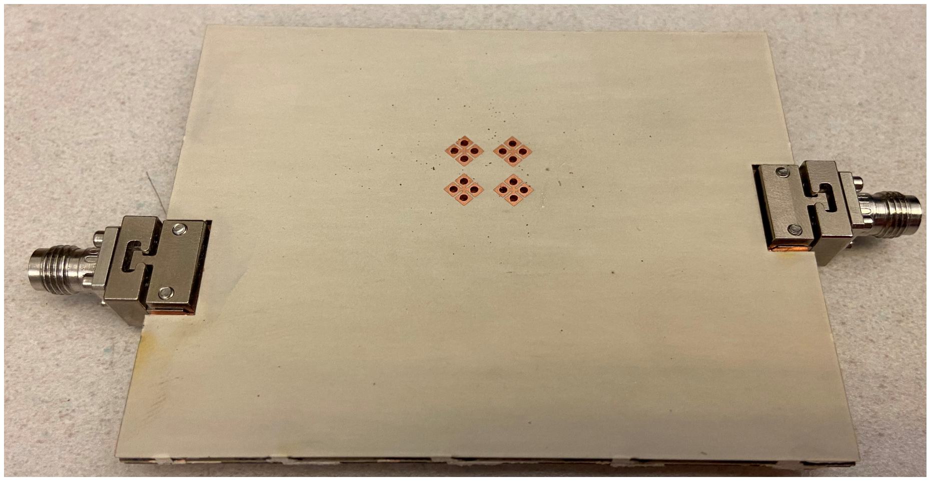

(a)

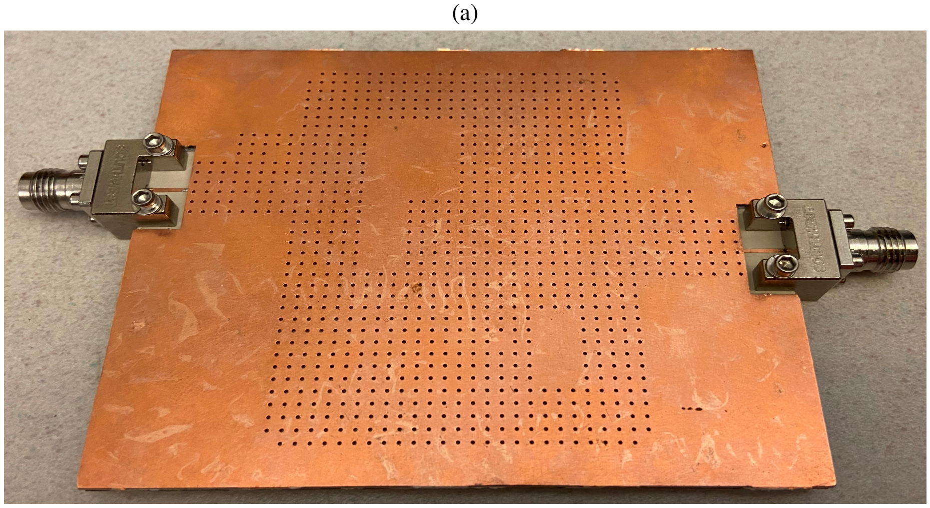

(b)

Figure 5.21: The fabricated dual CP polarized antenna, (a) top (b) bottom view.

The measured isolation between input ports is better than 15 over the whole operating frequency range, as shown in Fig. 5.23. Fig. 5.24 demonstrates the measured and simulated AR from excitation of each input port versus frequency. The measured 3-dB AR bandwidth for RHCP (when port 1 is excited) is 25.2% (25.7-33.1), and the simulated one is 29.3 % (25.3 GHz-34 GHz). The measured 3-dB AR bandwidth for LHCP (when port 2 is excited) is 21.6% (26-32.3), and the simulated one is 28.2% (25.3 GHz-33.6 GHz).

Considering the AR and impedance bandwidth for two ports, the available operating bandwidth is 20.1%, from 26.4 GHz to 32.3 GHz. The antenna CP gains are measured using the gain comparison method described in [98]. Fig. 5.25 presents the measured and simulated realized CP gains for RHCP and LHCP beams. The measured CP gains for two ports are in a range of 9-11.9 dBic within the corresponding operating bandwidth. For most portions of the operating frequency band, the measured gain is about 1 dB lower than the simulated one due to the connectors' insertion loss. A gain drop for LHCP at 27 GHz is caused by the difference between the values of measured AR and the simulated one.

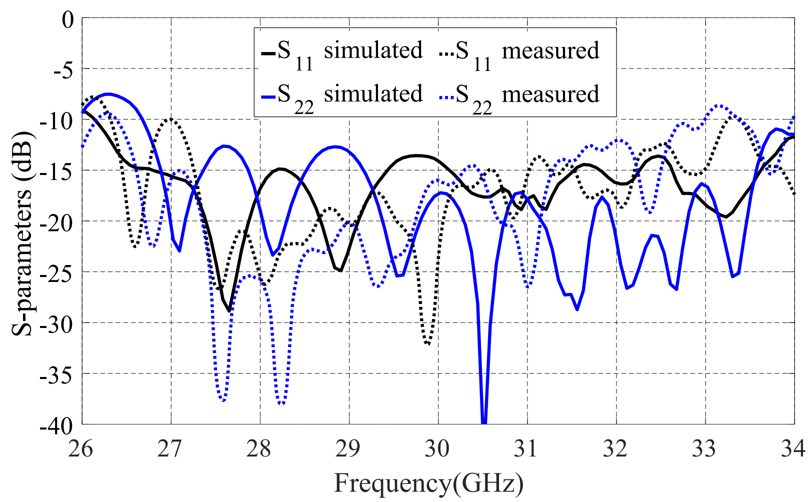

Figure 5.22: S-Parameters of the antenna array for excitation of each input port.

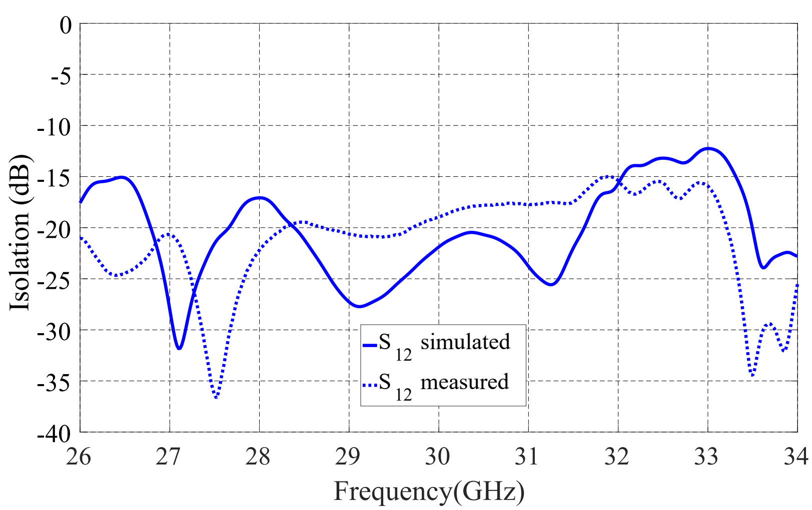

Figure 5.23: Measured and simulated isolation between port 1 and port 2.

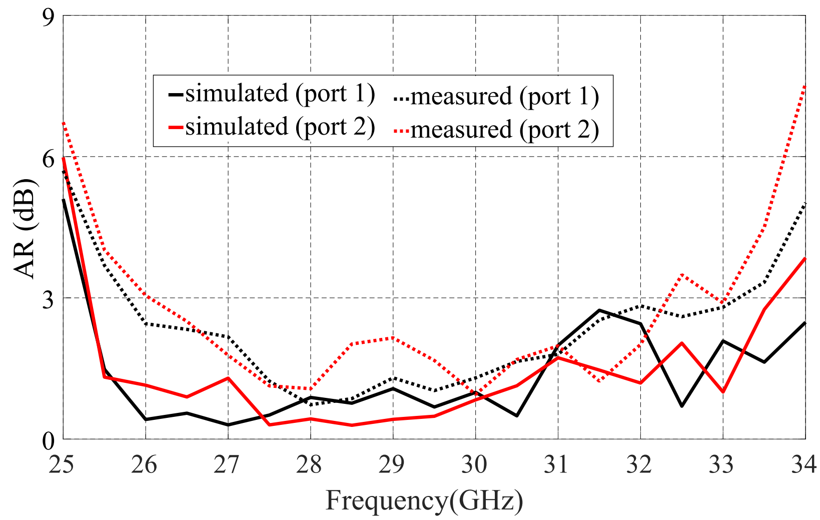

Figure 5.24: AR of the antenna array for excitation of each input port.

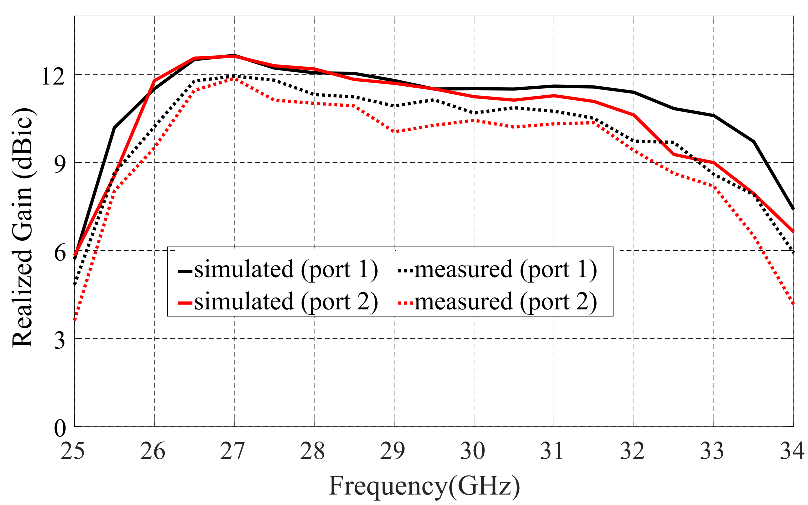

Figure 5.25: Realized gain of the antenna array for excitation of each input port.

Fig. 5.26 and Fig. 5.27 show the measured and simulated normalized radiation patterns in the E-plane and H-plane and at three frequencies of 27 GHz, 29 GHz, and 31 GHz for RHCP and LHCP, respectively. The measured XPDs are higher than 19.5 dB at E-plane and H-plane when excitation is from either port 1 or port 2. The simulated radiation efficiency is higher than 90%, within the operating frequency range.

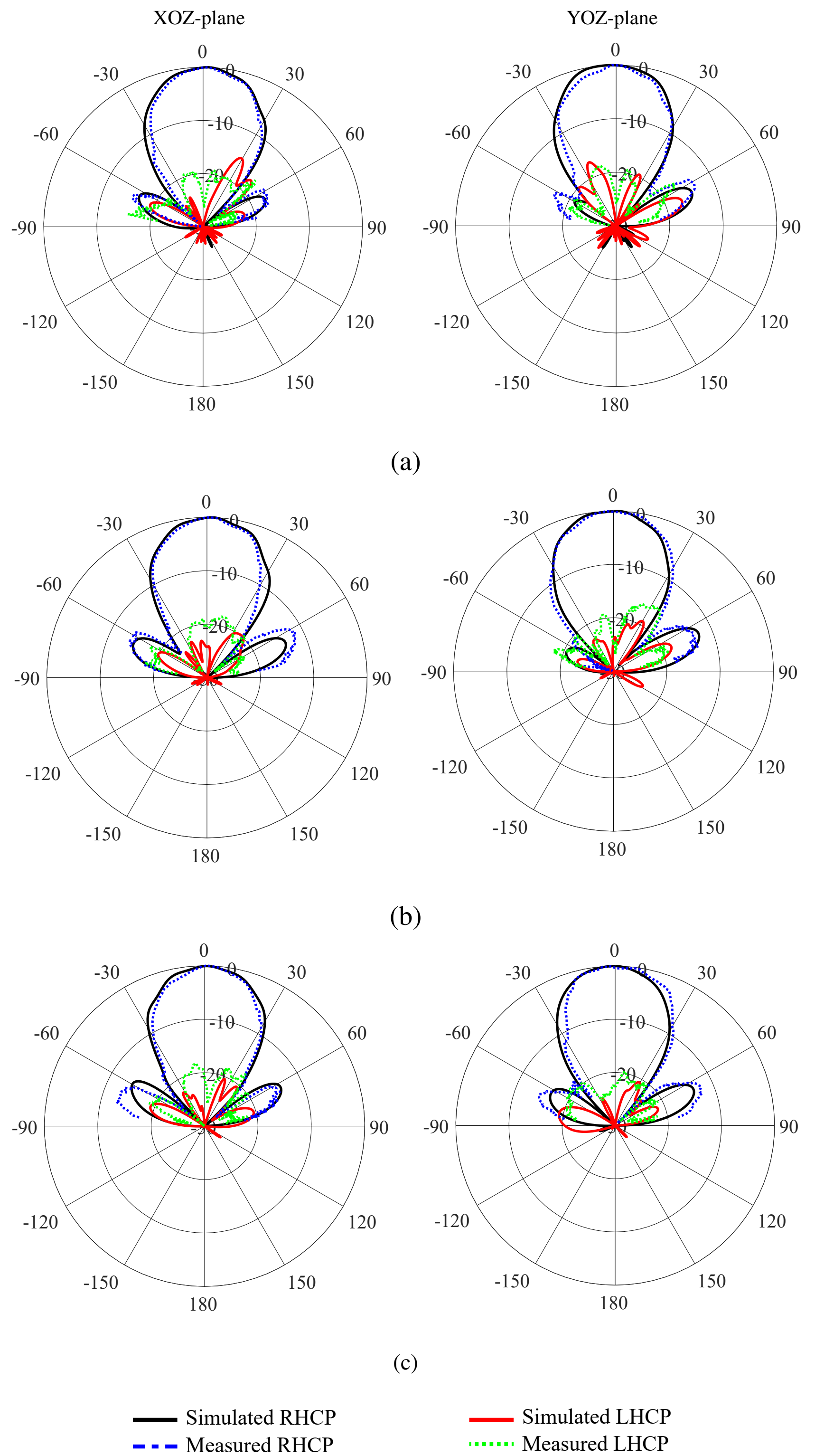

Figure 5.26: Simulated 2-D radiation patterns of the proposed dual polarized antenna array when port 1 is excited, (a) 27 GHz,(b) 29 GHz, and (c) 31 GHz.

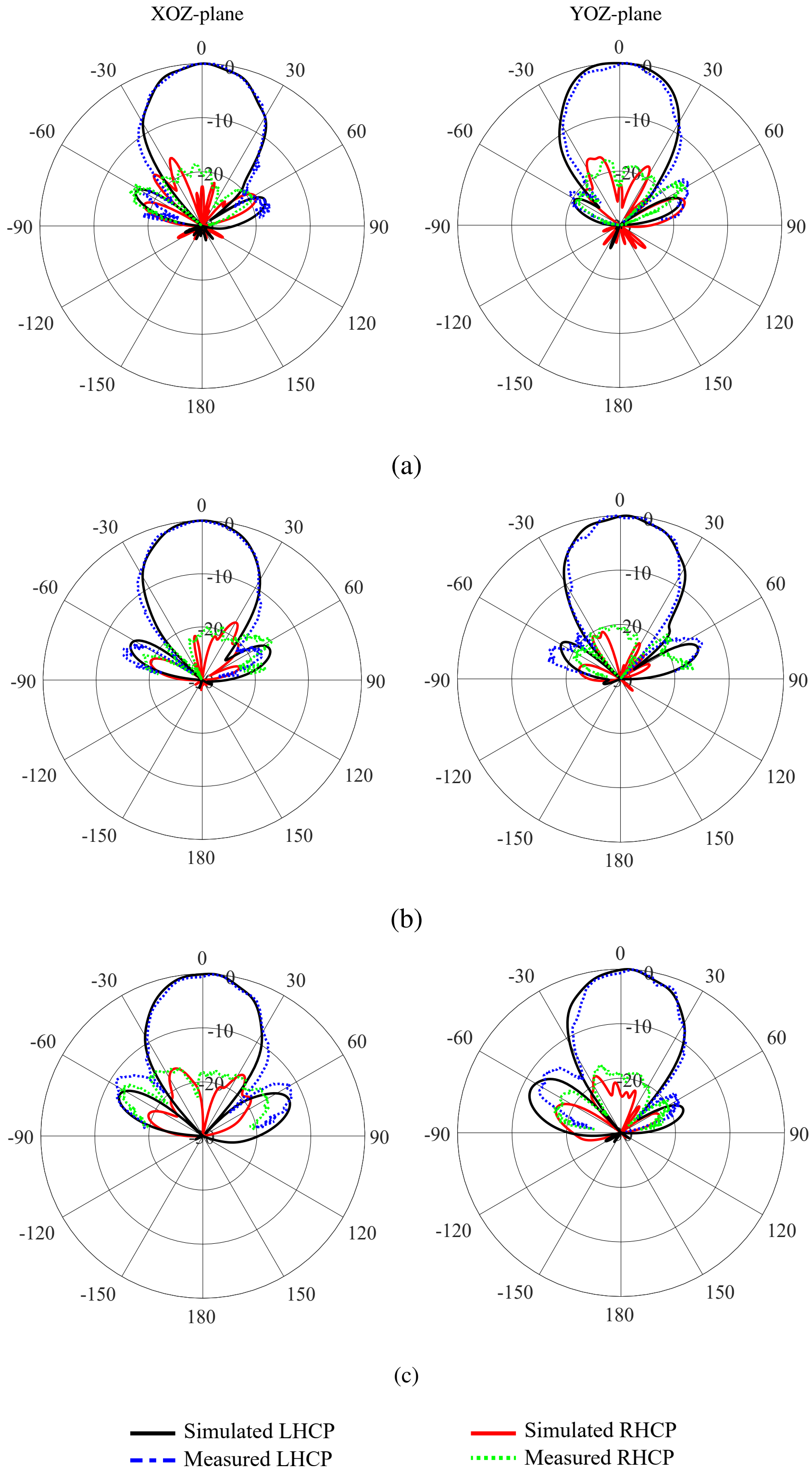

Figure 5.27: Simulated 2-D RP patterns of the proposed dual polarized antenna array when port 2 is excited (a) 27 GHz,(b) 29 GHz and (c) 31 GHz.

Fig. 5.28 depicts the simulated radiation efficiency for two polarizations. The simulated radiation efficiency is higher than 88%, within the operating frequency range.

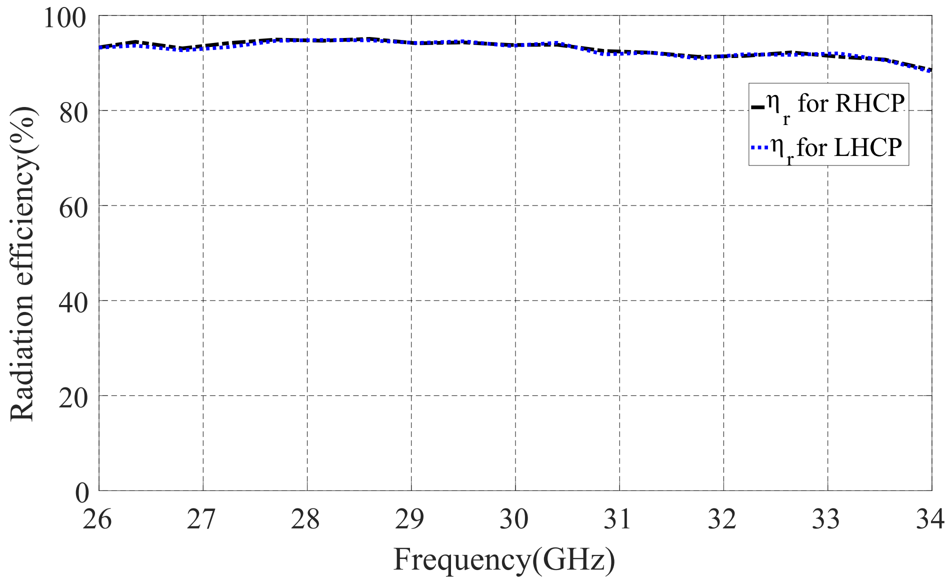

Figure 5.28: Simulated radiation efficiency for both CP Polarization.

5.4.3 Comparison and Discussion

The performances of the reported mm-wave dual CP antennas in [103–105, 107, 109] are compared with our design in Table 5.5. The presented SIW-based designs in [103–105] have the advantages of planner integration and a cost-effective fabrication process, but their radiation efficiencies are lower than 70% due to the high dielectric loss at mm-wave bands. In addition, the low-cost works in [103] and [105] have the problem of limited operating bandwidth. The proposed SIW-fed dual CP antenna in [104] shows wideband performance for two senses of circular polarization. However, it has poor port-to-port isolation. Even though the presented antennas in [107] and [109] have high radiation efficiency due to their waveguide-based feeding structures, they suffer from the difficulty of integration and high-cost manufacturing process of computer numerical control (CNC). The presented dual CP array exhibits a wideband impedance and AR bandwidth while featuring good isolation between the two input ports. In addition, benefiting from a PRGW feeding structure, our design has a low-cost fabrication process and high radiation efficiency.

Table 5.5: Comparison with other dual CP works

	Ref. [103]	Ref. [104]	Ref.[105]	Ref. [107]	Ref. [109]	This work
Radiating	slot	patch	patch	aperture	slot	ME dipole
Freq (GHz)	94	60	42	30	85	30
Fab. Tech	PCB	PCB	PCB	CNC	CNC	PCB
Element Num.	15×15	8×8	8×8	16×16	16×8	2×2
Fab. cost	low	low	low	high	high	low
Imp.& AR BW%	1.1	23	8.89	16	17	20.1
Min Iso.(dB)	15	11.9	19	13	20	15
Peak gain (dBic)	26	25.8	19.2	32.7	24	11.9
Rad. efficiency %	57.5	70	NG*	90	89	> 90

5.5 Summary

A broadband dual CP antenna array based on PRGW technology in the mm-wave band is presented. Two PRGW directional couplers, rat-race couplers, and a crossover are designed first and then integrated to build the dual CP feeding network on a single layer of the substrate. The proposed feeding network provides equal amplitudes and sequential phase differences of $90°$ between the output ports without using the phase shifter. A 2×2 sequentially rotated $45°$ ME dipole antenna is employed as a shared aperture for two senses of orthogonal polarizations. The prototype of the proposed dual-polarized structure is fabricated and tested verify the concept. The proposed antenna covers an overall measured bandwidth of 21.9% from 26.3-32.4 GHz (considering 10-dB impedance, 15-dB isolation, and 3-dB AR bandwidth). The measured realized gain for port 1 varies from 9.6 to 11.95 dBic, and for port 2 varies from 9.4 to 11.8 dBic. The designed antenna has the merit of high radiation efficiency, benefiting from a low-loss PRGW feeding network.

Chapter 6

Conclusions and Future Works

6.1 Summary

Millimeter-wave (mm-wave) spectrum is a promising solution for satisfying the requirements of 5G wireless communication systems since it has more data transmission capacity and can fulfill the growing traffic demand. To benefit from the available frequency band in mm-wave, antennas need to be broadband. Meanwhile, mm-wave CP antennas have received considerable interest due to their well-known features. Therefore, wideband CP antennas are highly required. This dissertation has been focused on the design and development of wideband CP and dual CP antennas at mm-wave frequency bands. To enhance the gain and bandwidth of the CP antenna, sequential rotation (SR) feeding is utilized. The SR feeding networks have been implemented by PRGW technology to achieve low loss and high integration capability.

Spiral and slot spiral antennas are chosen as the main CP radiating elements. These antennas are inherently wideband due to their frequency independent (FI) behavior. However, they have not been commonly employed in mm-wave frequency due to their dependency on balun feedings, mostly high profile and bulky. Therefore, we have proposed simple feeding techniques for both spiral and cavity-backed slot spiral antennas.

The motivation and objectives of the thesis are introduced in chapter 1. Key concepts of CP, sequential feeding (SR) technique, and a literature review of mm-wave CP antennas are presented in chapter 2.

In chapter 3, a new and simple method to excite the slot spiral antenna is introduced. The slot spiral antenna is fed through a backed TE_{120}-mode SIC. The TE_{120}-mode SIC provides differential feeding for the slot spiral antenna. An SR feeding network is developed based on the PRGW technology. A 2×2 cavity-backed slot spiral antenna array using an SR feeding network is employed to achieve wider AR and impedance bandwidth and higher gain. The proposed slot spiral antenna shows advantages such as wide operating bandwidth, good radiation efficiency, low profile, and simple structure.

In order to further improve the AR bandwidth and achieve a higher level of CP purity, an Archimedean spiral antenna with a novel feeding structure is presented in chapter 4. The antenna structure includes a radiating two-arm Archimedean spiral antenna on the top layer and a non-radiating patch dipole beneath the spiral arms. The spiral arms are connected to patches using two vias. Since the patches are located at the lateral side of the slot, the induced currents on vias have equal amplitude and 180° phase difference. Therefore, the vias behave as a balun for the spiral antenna. Furthermore, employing the non-radiating patch dipole causes the size reduction of the spiral antenna. The designed spiral antenna is placed in a 2×2 SR array arrangement, in which the feeding network is implemented using PRGW. The proposed antenna benefits from the wideband performance and high radiation efficiency and compact size, and low fabrication cost.

Chapter 5 investigates the novel design for realizing a dual CP antenna array. Firstly, a dual SR feeding network based on the PRGW is introduced for the first time. The feeding network is composed of a pair of wideband PRGW 3-dB directional couplers and PRGW rat-race couplers, along with the wideband PRGW crossover that are connected together to form the dual SR feeding structure on a single layer. The proposed dual SR feeding provides equal amplitude with sequentially phase offset of +90° and -90° between the output ports from excitation of ports 1 and 2, respectively. The designed feeding network does not require an additional phase shifter, contrary to the reported dual SR feeding networks in the literature. Secondly, the wideband 45° slant-polarized ME dipole antenna is developed. The reason to utilize the antenna with the polarization at the diagonal plane is to improve the XPD mainly at $\phi = 0°$ and $\phi = 180°$. Lastly, a 2×2 ME antenna array is constructed by incorporating the proposed feeding network. The proposed antenna features dual circular polarization, ease of fabrication as the feeding network is realized on one layer, and high radiation efficiency.

6.2 Future Works

In this thesis, wideband CP and Dual CP antennas have been designed based on the PRGW technology. The suggested future works can be listed as follows:

- Improve the gain of the presented CP antennas. High gain CP antennas are mostly realized by integrating multiple antennas into an array. However, the employment of the CP element in the full corporate feeding network deteriorates the AR performance due to the mutual coupling between the radiating elements in full corporate feeding networks [90]. Despite the fact that the sequential feeding network improves the AR of the antenna array, it increases the feeding network's complexity for the array size larger than 2×2. Frequency selective surfaces (FSS) and SRR lens are good candidates to increase the gain of CP antenna without degradation in the CP performance of the antenna array [126].

- Develop a dual CP antenna array using a two-arm Archimedean spiral antenna. As shown in chapter 2, a two-arm spiral antenna with anti-phase input currents produces circular polarization according to the spiral winding direction. A center-fed single spiral antenna is able to generate a dual sense of circular polarization if its arms' lengths differ by $\lambda/4$. In this case, when the currents that are excited in-phase at the input terminals reach the one wavelength circumference (active region of the first mode), they become out of phase, and no radiation occurs. However, since the arms' lengths differ by $\lambda/4$, the reflected currents on the longer arm travel a distance of $\lambda/2$ when they reach one-wavelength circumference. Therefore, the currents become in phase at the first active region, and radiation occurs. Consequently, the sense of polarization for the spiral arms with the in-phase input currents is opposite to the ones with anti-phase input currents [127].

- Design a dual-polarized feeding network using two layers of PRGW to improve the performance of the feeding network by avoiding the usage of crossover and making the structure more compact. In [128] and [129], the performance of the butler matrix is enhanced using these multilayer structures.

- Improve the compactness of the proposed dual CP feeding network in chapter 5 by replacing the rat-race coupler with PRGW 180° phase shifter.

- Design an mm-wave CP beam-switching antenna to achieve wider spatial coverage. Several mm-wave multi-beam LP antennas based on the SRR lens are presented in the literature [110, 130, 131]. The dual-polarized SRR lens can be used on top of CP antennas for beam scanning as well.

Appendix A

Electric Field of N-Element Sequentially Rotated Antenna Array

The electric field can be expressed in terms of co- and cross-polar components [23]:

$$\vec{E} = (E_{co}\hat{e}_{co} + E_{xp}\hat{e}_{xp})e^{-jkR} \tag{A.1}$$

Where $\hat{e_{co}}$ and $\hat{e_{xp}}$ are co-polar and cross-polar unit vectors, respectively. Co- and cross-polar unit vectors for RHCP, are defined as:

$$\hat{e}_{co} = \frac{\hat{x} - j\hat{y}}{\sqrt{2}} \tag{A.2}$$

$$\hat{e}_{xp} = \frac{\hat{x} + j\hat{y}}{\sqrt{2}} \tag{A.3}$$

To find the rotated electric field components at the broadside direction, we can use 2-D Rodrigues' rotation formula [54]:

$$\vec{r'} = cos\beta\vec{r} + sin\beta(\hat{n} \times \vec{r}) \tag{A.4}$$

Where $\vec{r'}$ is the rotated position vector, $\vec{r}$ is the position vector, β is the angle of rotation and $\vec{n}$

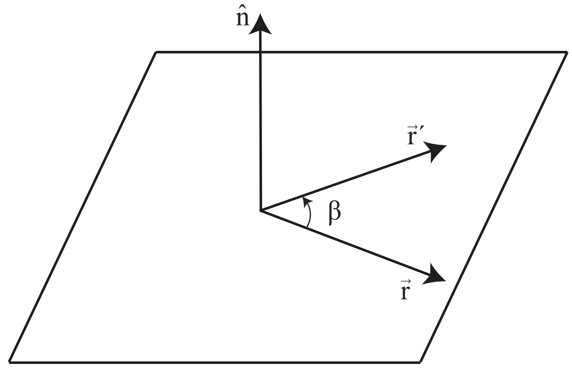

Figure A.1: Vector geometry of Rodrigues' rotation formula

is the axis of rotation. Therefore, the electric field of n_{th} antenna element rotated around the z-axis by angle of $n\beta$ can be obtained as:

$$\begin{aligned}\vec{E}'_n &= cos(n\beta)\vec{E} + sin(n\beta)(\hat{z} \times \vec{E})\\ \vec{E}'_n &= (e^{jn\beta}E_{co}\hat{e}_{co} + e^{-jn\beta}E_{xp}\hat{e}_{xp})e^{-jkz}\end{aligned} \tag{A.5}$$

After applying the phase shift of $n\alpha$ to each antenna element, the electric field can be written as:

$$\vec{E}''_n = e^{jn\alpha}\vec{E}'_n \tag{A.6}$$

$$\vec{E}''_n = (e^{jn(\beta+\alpha)}E_{co}\hat{e}_{co} + e^{-jn(\beta-\alpha)}E_{xp}\hat{e}_{xp})e^{-jkz} \tag{A.7}$$

Finally, the total electric field in the boresight direction produced by N sequentially rotated antenna elements is calculated as:

$$\vec{E}^t = \vec{E}^t_{co} + \vec{E}^t_{xp} = \sum_{n=0}^{N-1} \vec{E}''_n \tag{A.8}$$

$$= (\sum_{n=0}^{N-1} e^{jn(\beta+\alpha)} E_{co}\hat{e}_{co} + \sum_{n=0}^{N-1} e^{-jn(\beta-\alpha)} E_{xp}\hat{e}_{xp}) e^{-jkz}$$

For N ($N \geq 2$) sequentially rotated antenna elements generating RHCP radiation, geometrical phase rotation is in an anticlockwise direction ($\beta > 0$), considering $\alpha = -\beta$, the total co- and cross-polar components of the electric field become as follows:

$$\vec{E}^t_{co} = N E_{co}\hat{e}_{co} \tag{A.9}$$

$$\vec{E}^t_{xp} = 0 \tag{A.10}$$

Bibliography

[1] T. S. Rappaport *et al.*, *Wireless communications: principles and practice*. prentice hall PTR New Jersey, 1996, vol. 2.

[2] A. Osseiran, F. Boccardi, V. Braun, K. Kusume, P. Marsch, M. Maternia, O. Queseth, M. Schellmann, H. Schotten, H. Taoka *et al.*, “Scenarios for 5G mobile and wireless communications: the vision of the metis project,” *IEEE communications magazine*, vol. 52, no. 5, pp. 26–35, 2014.

[3] J. C. Wiltse, “History of millimeter and submillimeter waves,” *IEEE Transactions on microwave theory and techniques*, vol. 32, no. 9, pp. 1118–1127, 1984.

[4] K.-C. Huang and D. J. Edwards, *Millimetre wave antennas for gigabit wireless communications: a practical guide to design and analysis in a system context*. John Wiley & Sons, 2008.

[5] J. Du Preez and S. Sinha, *Millimeter-wave antennas: configurations and applications*. Springer, 2016.

[6] Z. Pi and F. Khan, “An introduction to millimeter-wave mobile broadband systems,” *IEEE communications magazine*, vol. 49, no. 6, pp. 101–107, 2011.

[7] C. E. Shannon, “A mathematical theory of communication,” *ACM SIGMOBILE mobile computing and communications review*, vol. 5, no. 1, pp. 3–55, 2001.

[8] M. Li and K.-M. Luk, "Wideband magneto-electric dipole antenna for 60-GHz millimeter-wave communications," *IEEE Transactions on Antennas and Propagation*, vol. 63, no. 7, pp. 3276–3279, 2015.

[9] J. Zhu, S. Li, S. Liao, and B.-L. Bu, "High-gain series-fed planar aperture antenna array," *IEEE Antennas and Wireless Propagation Letters*, vol. 16, pp. 2750–2754, 2017.

[10] Y. Al-Alem and A. A. Kishk, "High-gain 60 ghz slot antenna with symmetric radiation characteristics," *IEEE Transactions on Antennas and Propagation*, vol. 67, no. 5, pp. 2971–2982, 2019.

[11] Y. Al-Alem and A. A. Kishk, "Wideband millimeter-wave dielectric resonator antenna with gain enhancement," *IEEE Antennas and Wireless Propagation Letters*, vol. 18, no. 12, pp. 2711–2715, 2019.

[12] T. Zhang, L. Chen, A. U. Zaman, and J. Yang, "Ultra-wideband millimeter-wave planar array antenna with an upside-down structure of printed ridge gap waveguide for stable performance and high antenna efficiency," *IEEE Antennas and Wireless Propagation Letters*, vol. 20, no. 9, pp. 1721–1725, 2021.

[13] X. Bai, S.-W. Qu, and K. B. Ng, "Millimeter-wave cavity-backed patch-slot dipole for circularly polarized radiation," *IEEE Antennas and Wireless Propagation Letters*, vol. 12, pp. 1355–1358, 2013.

[14] X. Ruan and C. H. Chan, "A circularly polarized differentially fed transmission-line-excited magnetoelectric dipole antenna array for 5g applications," *IEEE Transactions on Antennas and Propagation*, vol. 67, no. 3, pp. 2002–2007, 2019.

[15] H. Xu, J. Zhou, K. Zhou, Q. Wu, Z. Yu, and W. Hong, "Planar wideband circularly polarized cavity-backed stacked patch antenna array for millimeter-wave applications," *IEEE Transactions on Antennas and Propagation*, vol. 66, no. 10, pp. 5170–5179, 2018.

[16] S. S. Gao, Q. Luo, and F. Zhu, "Introduction to circularly polarized antennas," 2014.

[17] J. Kaiser, “The archimedean two-wire spiral antenna,” *IRE Transactions on Antennas and Propagation*, vol. 8, no. 3, pp. 312–323, 1960.

[18] R. H. DuHamel and J. P. Scherer, “Frequency-independent antennas,” in *Antenna Engineering Handbook*. McGraw-Hill, 1993, pp. 1417–1465.

[19] E. Pucci, E. Rajo-Iglesias, and P.-S. Kildal, “New microstrip gap waveguide on mushroom-type ebg for packaging of microwave components,” *IEEE Microwave and Wireless Components Letters*, vol. 22, no. 3, pp. 129–131, 2012.

[20] E. Baghernia, M. M. M. Ali, and A. R. Sebak, “2$\times$ 2 slot spiral cavity-backed antenna array fed by printed gap waveguide,” *IEEE Access*, vol. 8, pp. 170 609–170 617, 2020.

[21] E. Baghernia, R. Movahedinia, and A.-R. Sebak, “Broadband compact circularly polarized spiral antenna array fed by printed gap waveguide for millimeter-wave applications,” *IEEE Access*, vol. 9, pp. 86–95, 2020.

[22] R. Paknys, *Applied frequency-domain electromagnetics*. John Wiley & Sons, 2016.

[23] P.-S. Kildal, *Foundations of antenna engineering: a unified approach for line-of-sight and multipath*. Artech House, 2015.

[24] C. A. Balanis, *Antenna theory: analysis and design*. John wiley & sons, 2015.

[25] S. V. Parekh, “Simple formulae for circular-polarization axial-ratio calculations,” *IEEE Antennas and Propagation magazine*, vol. 33, no. 1, pp. 30–32, 1991.

[26] M. Li and K.-M. Luk, “Low-cost wideband microstrip antenna array for 60-ghz applications,” *IEEE Transactions on Antennas and Propagation*, vol. 62, no. 6, pp. 3012–3018, 2014.

[27] J. Xu, W. Hong, Z. H. Jiang, and H. Zhang, “Low-profile circular patch array fed by slotted substrate integrated waveguide,” *IEEE Transactions on Antennas and Propagation*, vol. 67, no. 2, pp. 960–970, 2018.

[28] E.-Y. Jung, J. W. Lee, T. K. Lee, and W.-K. Lee, "Siw-based array antennas with sequential feeding for x-band satellite communication," *IEEE transactions on antennas and propagation*, vol. 60, no. 8, pp. 3632–3639, 2012.

[29] Q. Wu, J. Yin, C. Yu, H. Wang, and W. Hong, "Low-profile millimeter-wave siw cavity-backed dual-band circularly polarized antenna," *IEEE Transactions on Antennas and Propagation*, vol. 65, no. 12, pp. 7310–7315, 2017.

[30] B. Bahreini, H. Oraizi, N. Noori, and S. Fakhte, "Design of a circularly polarized parasitic array with slot-coupled dra with improved gain for the 5g mobile system," *IEEE Antennas and Wireless Propagation Letters*, vol. 17, no. 10, pp. 1802–1806, 2018.

[31] A. Perron, T. A. Denidni, and A. R. Sebak, "Circularly polarized microstrip/elliptical dielectric ring resonator antenna for millimeter-wave applications," *IEEE Antennas and Wireless Propagation Letters*, vol. 9, pp. 783–786, 2010.

[32] J. B. Dia'aaldin, S. Liao, and Q. Xue, "High gain and low cost differentially fed circularly polarized planar aperture antenna for broadband millimeter-wave applications," *IEEE Transactions on Antennas and Propagation*, vol. 64, no. 1, pp. 33–42, 2015.

[33] H. Nakano, K. Nogami, S. Arai, H. Mimaki, and J. Yamauchi, "A spiral antenna backed by a conducting plane reflector," *IEEE Transactions on Antennas and Propagation*, vol. 34, no. 6, pp. 791–796, 1986.

[34] H. Nakano, H. Takeda, T. Honma, H. Mimaki, and J. Yamauchi, "Extremely low-profile helix radiating a circularly polarized wave," 1991.

[35] C. Liu, Y.-X. Guo, X. Bao, and S.-Q. Xiao, "60-GHz LTCC integrated circularly polarized helical antenna array," *IEEE Transactions on Antennas and Propagation*, vol. 60, no. 3, pp. 1329–1335, 2011.

[36] V. Rumsey, "Frequency independent antennas," in *1958 IRE International Convention Record*, vol. 5. IEEE, 1966, pp. 114–118.

[37] J. Dyson, "The unidirectional equiangular spiral antenna," *IRE Transactions on Antennas and Propagation*, vol. 7, no. 4, pp. 329–334, 1959.

[38] C. A. Balanis, *Modern antenna handbook*. John Wiley & Sons, 2011.

[39] R. P. Penno and K. M. Pasala, "Angle estimation with a multi-arm spiral antenna," in *1999 IEEE Aerospace Conference. Proceedings (Cat. No. 99TH8403)*, vol. 3. IEEE, 1999, pp. 195–207.

[40] K. Puglia, "Electromagnetic simulation of some common balun structures," *IEEE microwave magazine*, vol. 3, no. 3, pp. 56–61, 2002.

[41] Y.-W. Zhong, G.-M. Yang, J.-Y. Mo, and L.-R. Zheng, "Compact circularly polarized archimedean spiral antenna for ultrawideband communication applications," *IEEE Antennas and Wireless Propagation Letters*, vol. 16, pp. 129–132, 2016.

[42] C. Fumeaux, D. Baumann, and R. Vahldieck, "Finite-volume time-domain analysis of a cavity-backed archimedean spiral antenna," *IEEE Transactions on Antennas and Propagation*, vol. 54, no. 3, pp. 844–851, 2006.

[43] T. Teshirogi, "Wide-band circularly polarized array antennas with sequential rotations and phase shift of elements," *Proc. ISAP'85, Kyoto, Aug.*, 1985.

[44] S.-l. S. Yang, R. Chair, A. A. Kishk, K.-F. Lee, and K.-M. Luk, "Study on sequential feeding networks for subarrays of circularly polarized elliptical dielectric resonator antenna," *IEEE Transactions on Antennas and Propagation*, vol. 55, no. 2, pp. 321–333, 2007.

[45] W. Yang, J. Zhou, Z. Yu, and L. Li, "Bandwidth-and gain-enhanced circularly polarized antenna array using sequential phase feed," *IEEE Antennas and Wireless Propagation Letters*, vol. 13, pp. 1215–1218, 2014.

[46] Y.-J. Hu, W.-P. Ding, and W.-Q. Cao, "Broadband circularly polarized microstrip antenna array using sequentially rotated technique," *IEEE antennas and wireless propagation letters*, vol. 10, pp. 1358–1361, 2011.

[47] P. Hall, J. Dahele, and J. James, "Design principles of sequentially fed, wide bandwidth, circularly polarised microstrip antennas," in *IEE Proceedings H (Microwaves, Antennas and Propagation)*, vol. 136, no. 5. IET, 1989, pp. 381–389.

[48] P. Hall, "Application of sequential feeding to wide bandwidth, circularly polarised microstrip patch arrays," in *IEE Proceedings H (Microwaves, Antennas and Propagation)*, vol. 136, no. 5. IET, 1989, pp. 390–398.

[49] U. R. Kraft, "Main-beam polarization properties of four-element sequential-rotation arrays with arbitrary radiators," *IEEE Transactions on Antennas and Propagation*, vol. 44, no. 4, pp. 515–522, 1996.

[50] A. R. Weily and Y. J. Guo, "Circularly polarized ellipse-loaded circular slot array for millimeter-wave wpan applications," *IEEE Transactions on Antennas and Propagation*, vol. 57, no. 10, pp. 2862–2870, 2009.

[51] Y.-J. Hu, W.-P. Ding, W.-M. Ni, and W.-Q. Cao, "Broadband circularly polarized cavity-backed slot antenna array with four linearly polarized disks located in a single circular slot," *IEEE Antennas and Wireless Propagation Letters*, vol. 11, pp. 496–499, 2012.

[52] Q. Luo, S. Gao, M. Sobhy, J. T. S. Sumantyo, J. Li, G. Wei, J. Xu, and C. Wu, "Dual circularly polarized equilateral triangular patch array," *IEEE Transactions on Antennas and Propagation*, vol. 64, no. 6, pp. 2255–2262, 2016.

[53] R. F. Ma, Z. H. Jiang, Y. Zhang, X. Y. Wu, T. Yue, W. Hong, and D. H. Werner, "Theory, design, and verification of dual-circularly polarized dual-beam arrays with independent control of polarization: A generalization of sequential rotation arrays," *IEEE Transactions on Antennas and Propagation*, vol. 69, no. 3, pp. 1369–1382, 2020.

[54] J. S. Dai, "Euler–rodrigues formula variations, quaternion conjugation and intrinsic connections," *Mechanism and Machine Theory*, vol. 92, pp. 144–152, 2015.

[55] J. Huang, "A technique for an array to generate circular polarization with linearly polarized

elements," *IEEE Transactions on antennas and propagation*, vol. 34, no. 9, pp. 1113–1124, 1986.

[56] H. J. Visser, *Array and phased array antenna basics*. John Wiley & Sons, 2006.

[57] A. K. Bhattacharyya, "Performance comparison between arrays with rotating linear polarization elements and circular polarization elements," in *2007 IEEE Applied Electromagnetics Conference (AEMC)*. IEEE, 2007, pp. 1–3.

[58] H. Iwasaki, T. Nakajima, and Y. Suzuki, "Gain improvement of circularly polarized array antenna using linearly polarized elements," *IEEE transactions on antennas and propagation*, vol. 43, no. 6, pp. 604–608, 1995.

[59] P. Hall, J. Huang, E. Rammos, and A. Roederer, "Gain of circularly polarised arrays composed of linearly polarised elements," *Electronics Letters*, vol. 25, no. 2, pp. 124–125, 1989.

[60] S.-K. Lin and Y.-C. Lin, "A compact sequential-phase feed using uniform transmission lines for circularly polarized sequential-rotation arrays," *IEEE transactions on antennas and propagation*, vol. 59, no. 7, pp. 2721–2724, 2011.

[61] A. Chen, Y. Zhang, Z. Chen, and C. Yang, "Development of a ka-band wideband circularly polarized 64-element microstrip antenna array with double application of the sequential rotation feeding technique," *IEEE antennas and wireless propagation letters*, vol. 10, pp. 1270–1273, 2011.

[62] M. Du, Y. Dong, J. Xu, and X. Ding, "35-GHz wideband circularly polarized patch array on LTCC," *IEEE Transactions on Antennas and Propagation*, vol. 65, no. 6, pp. 3235–3240, 2017.

[63] M. Sun, Y.-Q. Zhang, Y.-X. Guo, M. F. Karim, O. L. Chuen, and M. S. Leong, "Integration of circular polarized array and lna in ltcc as a 60-ghz active receiving antenna," *IEEE transactions on antennas and propagation*, vol. 59, no. 8, pp. 3083–3089, 2011.

[64] Q. Wu, H. Wang, C. Yu, and W. Hong, "Low-profile circularly polarized cavity-backed antennas using siw techniques," *IEEE Transactions on Antennas and Propagation*, vol. 64, no. 7, pp. 2832–2839, 2016.

[65] Y.-X. Zhang, Y.-C. Jiao, and L. Zhang, "Wideband circularly polarized array antennas with sequential-rotation polarization grid and simplified full-siw feeding networks," *IEEE Transactions on Antennas and Propagation*, vol. 68, no. 8, pp. 6088–6097, 2020.

[66] E. J. Denlinger, "Losses of microstrip lines," *IEEE Transactions on Microwave Theory and Techniques*, vol. 28, no. 6, pp. 513–522, 1980.

[67] W. M. Abdel-Wahab, Y. Wang, and S. Safavi-Naeini, "Siw five-port hybrid junction for cp mm-wave antenna applications," in *2013 IEEE Antennas and Propagation Society International Symposium (APSURSI)*. IEEE, 2013, pp. 996–997.

[68] P.-S. Kildal, E. Alfonso, A. Valero-Nogueira, and E. Rajo-Iglesias, "Local metamaterial-based waveguides in gaps between parallel metal plates," *IEEE Antennas and wireless propagation letters*, vol. 8, pp. 84–87, 2008.

[69] M. S. Sorkherizi and A. A. Kishk, "Fully printed gap waveguide with facilitated design properties," *IEEE Microwave and Wireless Components Letters*, vol. 26, no. 9, pp. 657–659, 2016.

[70] M. N. Afsar, "Dielectric measurements of millimeter-wave materials," *IEEE Transactions on Microwave Theory and Techniques*, vol. 32, no. 12, pp. 1598–1609, 1984.

[71] P.-S. Kildal, "Artificially soft and hard surfaces in electromagnetics," *IEEE Transactions on Antennas and Propagation*, vol. 38, no. 10, pp. 1537–1544, 1990.

[72] M. G. Silveirinha, C. A. Fernandes, and J. R. Costa, "Electromagnetic characterization of textured surfaces formed by metallic pins," *IEEE Transactions on Antennas and Propagation*, vol. 56, no. 2, pp. 405–415, 2008.

[73] P.-S. Kildal, "Definition of artificially soft and hard surfaces for electromagnetic waves," *Electronics Letters*, vol. 24, no. 3, pp. 168–170, 1988.

[74] D. Sievenpiper, L. Zhang, R. F. Broas, N. G. Alexopolous, and E. Yablonovitch, "High-impedance electromagnetic surfaces with a forbidden frequency band," *IEEE Transactions on Microwave Theory and techniques*, vol. 47, no. 11, pp. 2059–2074, 1999.

[75] P.-S. Kildal, A. U. Zaman, E. Rajo-Iglesias, E. Alfonso, and A. Valero-Nogueira, "Design and experimental verification of ridge gap waveguide in bed of nails for parallel-plate mode suppression," *IET Microwaves, Antennas & Propagation*, vol. 5, no. 3, pp. 262–270, 2011.

[76] E. Alfonso, M. Baquero, P.-S. Kildal, A. Valero-Nogueira, E. Rajo-Iglesias, and J. I. Herranz, "Design of microwave circuits in ridge-gap waveguide technology," in *2010 IEEE MTT-S International Microwave Symposium*. IEEE, 2010, pp. 1544–1547.

[77] E. Rajo-Iglesias and P.-S. Kildal, "Groove gap waveguide: A rectangular waveguide between contactless metal plates enabled by parallel-plate cut-off," in *Proceedings of the Fourth European Conference on Antennas and Propagation*. IEEE, 2010, pp. 1–4.

[78] E. Baghernia, A.-R. Sebak, and M. R. Chaharmir, "Groove gap wave guide slot array antenna in millimeter wave band," in *2018 18th International Symposium on Antenna Technology and Applied Electromagnetics (ANTEM)*. IEEE, 2018, pp. 1–2.

[79] E. Pucci, *Gap waveguide technology for millimeter wave applications and integration with antennas*. Chalmers Tekniska Hogskola (Sweden), 2013.

[80] S. A. Razavi, P.-S. Kildal, L. Xiang, H. Chen, and E. Alfonso, "Design of 60ghz planar array antennas using pcb-based microstrip-ridge gap waveguide and siw," in *The 8th European Conference on Antennas and Propagation (EuCAP 2014)*. IEEE, 2014, pp. 1825–1828.

[81] E. Pucci, A. U. Zaman, E. Rajo-Iglesias, and P.-S. Kildal, "New low loss inverted microstrip line using gap waveguide technology for slot antenna applications," in *Proceedings of the 5th European Conference on Antennas and Propagation (EUCAP)*. IEEE, 2011, pp. 979–982.

[82] M. S. Sorkherizi, A. Dadgarpour, and A. A. Kishk, "Planar high-efficiency antenna array using new printed ridge gap waveguide technology," *IEEE Transactions on antennas and propagation*, vol. 65, no. 7, pp. 3772–3776, 2017.

[83] E. Gschwendtner, D. Loffler, and W. Wiesbeck, "Spiral antenna with external feeding for planar applications," in *1999 IEEE Africon. 5th Africon Conference in Africa (Cat. No. 99CH36342)*, vol. 2. IEEE, 1999, pp. 1011–1014.

[84] Q. Zhu, K.-B. Ng, and C. H. Chan, "Printed circularly polarized spiral antenna array for millimeter-wave applications," *IEEE Transactions on Antennas and Propagation*, vol. 65, no. 2, pp. 636–643, 2016.

[85] J. Zhu, S. Liao, S. Li, and Q. Xue, "60 GHz wideband high-gain circularly polarized antenna array with substrate integrated cavity excitation," *IEEE Antennas and Wireless Propagation Letters*, vol. 17, no. 5, pp. 751–755, 2018.

[86] H. Nakano, T. Igarashi, H. Oyanagi, Y. Iitsuka, and J. Yamauchi, "Unbalanced-mode spiral antenna backed by an extremely shallow cavity," *IEEE Transactions on Antennas and propagation*, vol. 57, no. 6, pp. 1625–1633, 2009.

[87] Y. Cassivi, L. Perregrini, P. Arcioni, M. Bressan, K. Wu, and G. Conciauro, "Dispersion characteristics of substrate integrated rectangular waveguide," *IEEE Microwave and Wireless components letters*, vol. 12, no. 9, pp. 333–335, 2002.

[88] M. S. Sorkherizi and A. A. Kishk, "Transition from microstrip to printed ridge gap waveguide for millimeter-wave application," in *2015 IEEE International Symposium on Antennas and Propagation & USNC/URSI National Radio Science Meeting*. IEEE, 2015, pp. 1588–1589.

[89] T. Zhang, W. Hong, and K. Wu, "Analysis and optimum design of sequential-rotation array for gain bandwidth enhancement," *IEEE Transactions on Antennas and Propagation*, vol. 63, no. 1, pp. 142–150, 2014.

[90] Y. Li and K.-M. Luk, "A 60-GHz wideband circularly polarized aperture-coupled magneto-electric dipole antenna array," *IEEE Transactions on Antennas and Propagation*, vol. 64, no. 4, pp. 1325–1333, 2016.

[91] A. Chen, Y. Zhang, Z. Chen, and S. Cao, "A ka-band high-gain circularly polarized microstrip antenna array," *IEEE Antennas and wireless propagation letters*, vol. 9, pp. 1115–1118, 2010.

[92] C. Ma, Z.-H. Ma, and X. Zhang, "Millimeter-wave circularly polarized array antenna using substrate-integrated gap waveguide sequentially rotating phase feed," *IEEE Antennas and Wireless Propagation Letters*, vol. 18, no. 6, pp. 1124–1128, 2019.

[93] B. Zhang, Y. P. Zhang, D. Titz, F. Ferrero, and C. Luxey, "A circularly-polarized array antenna using linearly-polarized sub grid arrays for highly-integrated 60-ghz radio," *IEEE transactions on antennas and propagation*, vol. 61, no. 1, pp. 436–439, 2012.

[94] Y. Zhang, W. Hong, and R. Mittra, "45 ghz wideband circularly polarized planar antenna array using inclined slots in modified short-circuited siw," *IEEE Transactions on Antennas and Propagation*, vol. 67, no. 3, pp. 1669–1680, 2018.

[95] L. Schreider, X. Begaud, M. Soiron, and B. Perpere, "Archimedean microstrip spiral antenna loaded by chip resistors inside substrate," in *IEEE Antennas and Propagation Society Symposium, 2004.*, vol. 1. IEEE, 2004, pp. 1066–1069.

[96] H. NAKANO, J. YAMAUCHI, and S. HASHIMOTO, "Sunflower spiral antenna," *IEICE TRANSACTIONS (1976-1990)*, vol. 64, no. 12, pp. 763–769, 1981.

[97] K. L. Chung, "High-performance circularly polarized antenna array using metamaterial-line based feed network," *IEEE Transactions on Antennas and Propagation*, vol. 61, no. 12, pp. 6233–6237, 2013.

[98] B. Y. Toh, R. Cahill, and V. F. Fusco, "Understanding and measuring circular polarization," *IEEE Transactions on Education*, vol. 46, no. 3, pp. 313–318, 2003.

[99] M. M. M. Ali and A. Sebak, "Printed RGW circularly polarized differential feeding antenna array for 5G communications," *IEEE Transactions on Antennas and Propagation*, vol. 67, no. 5, pp. 3151–3160, 2019.

[100] B. Feng, J. Lai, K. L. Chung, T.-Y. Chen, Y. Liu *et al.*, "A compact wideband circularly polarized magneto-electric dipole antenna array for 5g millimeter-wave application," *IEEE Transactions on Antennas and Propagation*, vol. 68, no. 9, pp. 6838–6843, 2020.

[101] R. G. Vaughan, "Polarization diversity in mobile communications," *IEEE Transactions on Vehicular Technology*, vol. 39, no. 3, pp. 177–186, 1990.

[102] S. S. Gao, Q. Luo, and F. Zhu, *Circularly polarized antennas*. John Wiley & Sons, 2013.

[103] Y. J. Cheng, J. Wang, and X. L. Liu, "94 ghz substrate integrated waveguide dual-circular-polarization shared-aperture parallel-plate long-slot array antenna with low sidelobe level," *IEEE Transactions on Antennas and Propagation*, vol. 65, no. 11, pp. 5855–5861, 2017.

[104] Y. Zhao and K.-M. Luk, "Dual circular-polarized siw-fed high-gain scalable antenna array for 60 GHz applications," *IEEE Transactions on Antennas and Propagation*, vol. 66, no. 3, pp. 1288–1298, 2018.

[105] J. Xu, W. Hong, Z. H. Jiang, J. Chen, and H. Zhang, "A q-band low-profile dual circularly polarized array antenna incorporating linearly polarized substrate integrated waveguide-fed patch subarrays," *IEEE Transactions on Antennas and Propagation*, vol. 65, no. 10, pp. 5200–5210, 2017.

[106] Y.-H. Yang, B.-H. Sun, and J.-L. Guo, "A low-cost, single-layer, dual circularly polarized antenna for millimeter-wave applications," *IEEE Antennas and Wireless Propagation Letters*, vol. 18, no. 4, pp. 651–655, 2019.

[107] J. Wu, Y. J. Cheng, H. B. Wang, Y. C. Zhong, D. Ma, and Y. Fan, "A wideband dual circularly polarized full-corporate waveguide array antenna fed by triple-resonant cavities," *IEEE Transactions on Antennas and Propagation*, vol. 65, no. 4, pp. 2135–2139, 2016.

[108] X. Cheng, Y. Yao, T. Yu, J. Yu, and X. Chen, "Wideband dual circularly polarized antipodal septum antenna for millimeter-wave applications," *IEEE Transactions on Antennas and Propagation*, vol. 69, no. 6, pp. 3549–3554, 2020.

[109] F. Ayoub, Y. Tawk, E. Ardelean, J. Costantine, S. Lane, and C. Christodoulou, "Cross-slotted waveguide array with dual circularly polarized radiation at w-band," *IEEE Transactions on Antennas and Propagation*, 2021.

[110] A. Dadgarpour, M. S. Sorkherizi, T. A. Denidni, and A. A. Kishk, "Passive beam switching and dual-beam radiation slot antenna loaded with enz medium and excited through ridge gap waveguide at millimeter-waves," *IEEE transactions on Antennas and Propagation*, vol. 65, no. 1, pp. 92–102, 2016.

[111] N. Ashraf, A. R. Sebak, and A. A. Kishk, "Packaged microstrip line feed network on a single surface for dual-polarized 2 n$\times$ 2 m me-dipole antenna array," *IEEE Antennas and Wireless Propagation Letters*, vol. 19, no. 4, pp. 596–600, 2020.

[112] A. Dadgarpour, N. Bayat-Makou, M. A. Antoniades, A. A. Kishk, and A. Sebak, "A dual-polarized magnetoelectric dipole array based on printed ridge gap waveguide with dual-polarized split-ring resonator lens," *IEEE Transactions on Antennas and Propagation*, vol. 68, no. 5, pp. 3578–3585, 2020.

[113] M. M. M. Ali, I. Afifi, and A.-R. Sebak, "A dual-polarized magneto-electric dipole antenna based on printed ridge gap waveguide technology," *IEEE Transactions on Antennas and Propagation*, vol. 68, no. 11, pp. 7589–7594, 2020.

[114] D.-F. Guan, C. Ding, Z.-P. Qian, Y.-S. Zhang, Y. J. Guo, and K. Gong, "Broadband high-gain siw cavity-backed circular-polarized array antenna," *IEEE Transactions on Antennas and Propagation*, vol. 64, no. 4, pp. 1493–1497, 2016.

[115] M. Caillet, M. Clenet, A. Sharaiha, and Y. M. Antar, "A compact wide-band rat-race hybrid using microstrip lines," *IEEE Microwave and Wireless Components Letters*, vol. 19, no. 4, pp. 191–193, 2009.

[116] M. Akbari, M. Farahani, S. Zarbakhsh, M. D. Ardakani, A.-R. Sebak, T. A. Denidni, and O. M. Ramahi, "Highly efficient 30 ghz 2x2 beamformer based on rectangular air-filled coaxial line," *IEEE Transactions on Antennas and Propagation*, vol. 68, no. 7, pp. 5236–5246, 2020.

[117] E. H. Fooks and R. A. Zakarevicius, *Microwave engineering using microstrip circuits*. Prentice-Hall, Inc., 1990.

[118] J. Zhu, S. Liao, Y. Yang, S. Li, and Q. Xue, "60 ghz dual-circularly polarized planar aperture antenna and array," *IEEE Transactions on Antennas and Propagation*, vol. 66, no. 2, pp. 1014–1019, 2017.

[119] K.-M. Luk and H. Wong, "A new wideband unidirectional antenna element," *Int. J. Microw. Opt. Technol.*, vol. 1, no. 1, pp. 35–44, 2006.

[120] L. Siu, H. Wong, and K.-M. Luk, "A dual-polarized magneto-electric dipole with dielectric loading," *IEEE Transactions on antennas and propagation*, vol. 57, no. 3, pp. 616–623, 2009.

[121] Y. Li, J. Wang, and K.-M. Luk, "Millimeter-wave multibeam aperture-coupled magnetoelectric dipole array with planar substrate integrated beamforming network for 5g applications," *IEEE transactions on antennas and propagation*, vol. 65, no. 12, pp. 6422–6431, 2017.

[122] A. Dadgarpour, M. S. Sorkherizi, and A. A. Kishk, "High-efficient circularly polarized magnetoelectric dipole antenna for 5g applications using dual-polarized split-ring resonator lens," *IEEE Transactions on Antennas and Propagation*, vol. 65, no. 8, pp. 4263–4267, 2017.

[123] A. Chlavin, "A new antenna feed having equal e-and h-plane patterns," *Transactions of the IRE Professional Group on Antennas and Propagation*, vol. 2, no. 3, pp. 113–119, 1954.

[124] Z.-Y. Zhang and K.-L. Wu, "A wideband dual-polarized dielectric magnetoelectric dipole antenna," *IEEE Transactions on Antennas and Propagation*, vol. 66, no. 10, pp. 5590–5595, 2018.

[125] A. Dadgarpour, M. S. Sorkherizi, and A. A. Kishk, "Wideband low-loss magnetoelectric dipole antenna for 5g wireless network with gain enhancement using meta lens and gap waveguide technology feeding," *IEEE Transactions on Antennas and Propagation*, vol. 64, no. 12, pp. 5094–5101, 2016.

[126] E. Baghernia and A.-R. Sebak, "Gain enhancement of wideband millimeter-wave circularly

polarized antenna based on fss superstrate," in *2021 IEEE 19th International Symposium on Antenna Technology and Applied Electromagnetics (ANTEM)*. IEEE, 2021, pp. 1–2.

[127] O. Kim and J. Dyson, "A log-spiral antenna with selectable polarization," *IEEE Transactions on Antennas and Propagation*, vol. 19, no. 5, pp. 675–677, 1971.

[128] M. Ansari, H. Zhu, N. Shariati, and Y. J. Guo, "Compact planar beamforming array with endfire radiating elements for 5g applications," *IEEE Transactions on Antennas and Propagation*, vol. 67, no. 11, pp. 6859–6869, 2019.

[129] A. A. M. Ali, N. J. Fonseca, F. Coccetti, and H. Aubert, "Design and implementation of two-layer compact wideband butler matrices in siw technology for ku-band applications," *IEEE Transactions on Antennas and Propagation*, vol. 59, no. 2, pp. 503–512, 2010.

[130] A. Dadgarpour, B. Zarghooni, B. S. Virdee, and T. A. Denidni, "One-and two-dimensional beam-switching antenna for millimeter-wave mimo applications," *IEEE Transactions on Antennas and Propagation*, vol. 64, no. 2, pp. 564–573, 2015.

[131] T. Li and Z. N. Chen, "Control of beam direction for substrate-integrated waveguide slot array antenna using metasurface," *IEEE Transactions on Antennas and Propagation*, vol. 66, no. 6, pp. 2862–2869, 2018.

List of Publications

Journal Papers

- E. Baghernia, A. Dadgarpour and A. Sebak, “Wideband Dual Circularly Polarized Magneto-Electric Dipole Antenna Array Based on Printed Ridge Gap Waveguide”. Manuscript is submitted to IEEE Transactions on Antennas and Propagation, 2022.
- E. Baghernia, R. Movahedinia and A. -R. Sebak, “Broadband Compact Circularly Polarized Spiral Antenna Array Fed by Printed Gap Waveguide for Millimeter-Wave Applications,” IEEE Access, vol. 9, pp. 86-95, 2021.
- E. Baghernia, M. M. M. Ali and A. R. Sebak, “2 × 2 Slot Spiral Cavity-Backed Antenna Array Fed by Printed Gap Waveguide,” IEEE Access, vol. 8, pp. 170609-170617, 2020.

Conference Papers

- E. Baghernia and A. Sebak, “Gain Enhancement of Wideband Millimeter-Wave Circularly Polarized Antenna Based on FSS Superstrate,” 2021 IEEE 19th International Symposium on Antenna Technology and Applied Electromagnetics (ANTEM), 2021, pp. 1-2.
- E. Baghernia and A. Sebak, “Millimeter-Wave Wideband Printed Circularly Polarized Antenna Fed by PGW,” 2020 IEEE International Symposium on Antennas and Propagation and North American Radio Science Meeting, 2020, pp. 155-156.
- E. Baghernia, A. Sebak and M. R. Chaharmir, “Groove Gap waveguide Slot Array Antenna in Millimeter Wave Band,” 2018 18th International Symposium on Antenna Technology and

Applied Electromagnetics (ANTEM), 2018, pp. 1-2.